

Tunable Optics

Spectral Imaging and Surface Manipulation on Liquid Lenses

Strauch, Matthias

DOI

[10.4233/uuid:b61aa64e-cba4-44c0-8d16-93440e028611](https://doi.org/10.4233/uuid:b61aa64e-cba4-44c0-8d16-93440e028611)

Publication date

2020

Document Version

Final published version

Citation (APA)

Strauch, M. (2020). *Tunable Optics: Spectral Imaging and Surface Manipulation on Liquid Lenses*. [Dissertation (TU Delft), Delft University of Technology]. <https://doi.org/10.4233/uuid:b61aa64e-cba4-44c0-8d16-93440e028611>

Important note

To cite this publication, please use the final published version (if applicable). Please check the document version above.

Copyright

Other than for strictly personal use, it is not permitted to download, forward or distribute the text or part of it, without the consent of the author(s) and/or copyright holder(s), unless the work is under an open content license such as Creative Commons.

Takedown policy

Please contact us and provide details if you believe this document breaches copyrights. We will remove access to the work immediately and investigate your claim.

Tunable Optics

Spectral Imaging and Surface Manipulation on Liquid Lenses

Proefschrift

**ter verkrijging van de graad van doctor
aan de Technische Universiteit Delft,
op gezag van de Rector Magnificus
prof. dr. ir. T.H.J.J. van der Hagen;
voorzitter van het College voor Promoties,
in het openbaar te verdedigen op
30-3-2020 om 12:30 uur
door**

Matthias STRAUCH

Master of Science, Ludwig-Maximilians-Universität
München, Duitsland
geboren te München, Duitsland

Dit proefschrift is goedgekeurd door de promotoren.

Samenstelling promotiecommissie bestaat uit:

Rector Magnificus,	voorzitter
Prof. dr. H.P. Urbach,	TU Delft, promotor
Dr. F. Bociort,	TU Delft, copromotor

Onafhankelijke leden:

Prof. dr. ir. C.R. Kleijn,	TU Delft
Prof. dr. M.C.G. Aalders,	Universiteit van Amsterdam
Prof. I.L. Livshits,	ITMO University, Rusland
Prof. dr. G. Vdovin,	TU Delft
Dr. B.J. Feenstra,	SMART Photonics

© 2020 Matthias Strauch

ISBN 978-94-028-1994-6

Dit onderzoek werd gefinancierd via het Spectr@phone project (IPD 12017) van het IOP Photonic Devices programma van de RVO.

Tunable Optics

Spectral Imaging and Surface Manipulation on Liquid Lenses

Dissertation

**for the purpose of obtaining the degree of doctor
at Delft University of Technology
by the authority of the Rector Magnificus
prof. dr. ir. T.H.J.J. van der Hagen;
Chair of the Board for Doctorates
to be defended publicly on
30-3-2020 at 12:30 o'clock
by**

Matthias STRAUCH

Master of Science, Ludwig-Maximilians-Universität
München, Germany
born in München, Germany

This dissertation has been approved by the promotors.

Composition of the doctoral committee:

Rector Magnificus,	chairperson
Prof. dr. H.P. Urbach,	Delft University of Technology, promotor
Dr. F. Bociort,	Delft University of Technology, copromotor

Independent members:

Prof. dr. ir. C.R. Kleijn,	Delft University of Technology
Prof. dr. M.C.G. Aalders,	University of Amsterdam
Prof. I.L. Livshits,	ITMO University, Russia
Prof. dr. G. Vdovin,	Delft University of Technology
Dr. B.J. Feenstra,	SMART Photonics

© 2020 Matthias Strauch

ISBN 978-94-028-1994-6

This research was funded through the Spectr@phone project (IPD 12017) of the IOP Photonic Devices program of RVO.

Contents

Summary	vii
Samenvatting	ix
I. Spectral imaging	1
1. Spectral imaging of bruises	3
1.1. Bruises as an indicator for child abuse	4
1.1.1. Bruise formation	4
1.1.2. Hyperspectral investigation of bruises	6
1.2. Age determination	6
1.3. Development of a new spectral camera	10
1.3.1. Requirements	10
1.3.2. Spectral imaging basics	10
1.3.3. Spectral imaging techniques	12
1.3.4. Comparison of different spectral imaging techniques	18
1.3.5. Development of a demonstrator camera	19
1.4. Design of the Fabry-Pérot interferometer	22
1.4.1. Basic concept	22
1.4.2. Mirror coatings	26
1.4.3. Comparison of a single and a multilayer example	27
1.4.4. Surface roughness	29
1.5. Optical design	34
1.5.1. Collimated design	35
1.5.2. Telecentric design	35
2. Wide-angle spectral imaging using a Fabry-Pérot interferometer	39
2.1. Importance of spectral imaging in surveillance cameras	39
2.2. Design criterion	40
2.3. The collimated and the telecentric design	42
2.4. Comparison of the spectral performance	44
2.5. Concluding remarks	51
II. Electrowetting liquid lenses	53
3. Focusing light using liquid optics	55
3.1. Liquid lens techniques	56
3.1.1. Tunable acoustic gradient index of refraction lenses	56

3.1.2.	Liquid crystal lenses	57
3.1.3.	Membrane liquid lenses	57
3.1.4.	Electrowetting liquid lenses	58
3.2.	Electrowetting	59
3.2.1.	Wetting	59
3.2.2.	Electrowetting	61
3.3.	Electrowetting liquid lens	62
3.3.1.	Arctic 39N0	65
4.	Study of surface modes on a vibrating electrowetting liquid lens	67
4.1.	Known performance impacts of surface vibrations	67
4.2.	Liquid surface model	68
4.3.	Approximations and limitations	71
4.4.	Measurement setup	72
4.5.	Simulation of a liquid lens using Fresnel propagation	74
4.6.	Confirmation of the membrane model	76
4.7.	Applicability	79
5.	Creation of a tunable asphere with an electrowetting liquid lens	81
5.1.	Aberration correction with liquid lenses	82
5.2.	Construction of a desired surface shape using Bessel functions	82
5.2.1.	Orthogonality of the Bessel function	83
5.2.2.	Hankel transform	85
5.3.	Implementation	87
5.4.	Interferometric surface measurements	88
5.5.	Construction of arbitrary aspheres	93
5.6.	Summary	99
6.	Conclusion	101
	Bibliography	102
	Appendix	119
A.	Optical design specifications	121
A.1.	Lens designs	121
A.2.	Transmittance spectrum analysis in CODE V	125
B.	Voltage signal generation	131
B.1.	Amplification	131
B.2.	LabView software	131
B.2.1.	Creation of cosine waveforms	132
B.2.2.	Liquid lens signal generation	132
B.2.3.	Camera driver	133
B.2.4.	Arbitrary liquid lens surface generation	133

C. Interferogram analysis	139
D. Implementation of the Hankel transform	143
D.1. Calculation of the actuation voltage signal	143
D.2. Export to LabVIEW	144
Curriculum vitæ	147
List of Publications	149

Summary

This thesis focusses on two aspects of tunable optics: Fabry-Pérot interferometers with a variable distance between their mirrors and electrowetting liquid lenses.

The need for a device to detect child abuse has motivated us to design and build a camera that can detect the chemical composition of the upper skin layers of a bruise using a self-made Fabry-Pérot interferometer. The research described in the first part of this thesis has shown that wide-angle spectral imaging can be achieved with compact and cost-effective cameras using Fabry-Pérot interferometers. Designs with a full field of 90° in which the Fabry-Pérot interferometer is mounted either in front of an imaging system or behind a telecentric lens system are presented and analysed. The dependency of the spectral resolution on the numerical aperture of the lens system is derived and its value as a design criterion is shown. It is shown that the telecentric camera design is preferable over the collimated design for bruise imaging with a Fabry-Pérot interferometer.

The idea to use a liquid lens for spectral imaging has directed the research towards a new concept of controlling surface waves on the surface of a liquid lens. We investigate and model surface waves because they decrease the imaging quality during fast focal switching. We propose a model that describes the surface modes appearing on a liquid lens and that predicts the resonance frequencies. The effects of those surface modes on a laser beam are simulated using geometrical optics and Fresnel propagation, and the model is verified experimentally. The model of the surface oscillations is used to develop a technique to create aspheric surface shapes on commercially available electrowetting liquid lenses. The surface waves on the liquid lens are described by Bessel functions of which a linear combination can be used to create any circularly symmetrical aspheric lens shape at an instant of time. With these surface profiles, one can realise a large set of circularly symmetrical wavefronts and hence intensity distributions of beams transmitted by the lens. The necessary liquid lens actuation to achieve a desired shape is calculated via a Hankel transform and confirmed experimentally. The voltage signal can be repeated at video rate. Measurements taken with a Mach-Zehnder interferometer confirm the model of the surface waves. The capabilities and limitations of the proposed method are demonstrated using the examples of a Bessel surface, spherical aberration, an axicon, and a top hat structure.

Samenvatting

Dit proefschrift is gericht op twee aspecten van afstembare optica: Fabry-Pérot interferometers met een variabele afstand tussen de spiegels en op vloeistofflenszen, gebaseerd op elektrobevochtiging.

De behoefte aan een apparaat om kindermishandeling te detecteren motiveert ons om een camera te ontwerpen en te bouwen, die met behulp van een zelfgemaakte Fabry-Pérot interferometer de chemische samenstelling van de bovenste huidlagen van een blauwe plek kan detecteren. Het in het eerste deel van dit proefschrift beschreven onderzoek heeft aangetoond dat spectrale groothoekbeeldvorming kan worden gerealiseerd met compacte en goedkope camera's, samen met Fabry-Pérot interferometers. Ontwerpen met een beeldhoek van 90° , waarin de Fabry-Pérot interferometer vóór een beeldvormend systeem of áchter een telecentrisch lensstelsel is gemonteerd, worden gepresenteerd en geanalyseerd. De relatie tussen de spectrale resolutie en de numerieke apertuur van het lensstelsel wordt afgeleid en de waarde ervan als ontwerpcriterium wordt getoond. Er is aangetoond dat het ontwerp van de telecentrische camera de voorkeur verdient boven het gecollimeerde ontwerp voor beeldvorming door middel van een Fabry-Pérot interferometer.

Het idee om een vloeistofflens te gebruiken voor spectrale beeldvorming heeft het onderzoek gericht op een nieuw concept om oppervlaktegolven op het oppervlak van een vloeistofflens te besturen. We onderzoeken en modelleren oppervlaktegolven omdat deze de kwaliteit van het beeld verminderen tijdens snelle brandpuntveranderingen. We stellen een model voor, dat de oppervlaktewoorden beschrijft, die op een vloeistofflens verschijnen en dat de resonantiefrequenties voorspelt. De effecten van deze oppervlaktewoorden op een laserstraal worden gesimuleerd met behulp van geometrische optica en Fresnel propagatie, en het model wordt experimenteel geverifieerd. Het model van de oppervlaktetrillingen wordt gebruikt voor de ontwikkeling van een techniek om asferische oppervlaktevormen op in de handel verkrijgbare elektrobevochtigingvloeistofflenszen te creëren. De oppervlaktegolven op de vloeistofflens worden beschreven door Bessel functies, waarvan een lineaire combinatie kan worden gevormd, om iedere cirkelsymmetrische asferische lensvorm op enig moment in de tijd te creëren. Met deze oppervlakteprofielen kan men een grote set cirkelsymmetrische golffronten en dus intensiteitsverdelingen van door de lens vallend licht realiseren. De noodzakelijke vloeistoffensaandrijving om een gewenste vorm te bereiken wordt met een Hankel transformatie berekend en experimenteel bevestigd. Het spanningssignaal kan met videosnelheid worden herhaald. Metingen met een Mach-Zehnder interferometer bevestigen het model van de oppervlaktegolven. De mogelijkheden en beperkingen van de voorgestelde methode worden gedemonstreerd aan de hand van enkele voorbeelden: een Bessel oppervlak, sferische aberratie, een axicon en een hoge hoedstructuur.

Part I.

Spectral imaging

1. Spectral imaging of bruises

Spectral imaging has a very popular topic in research and engineering in recent years in optics. Almost 2000 scientific publications are published every year [1]. The number has doubled since 2010 and spectral imaging has entered many fields of science and industry today. The applications range from astronomy to agriculture and from arts to medicine and forensics.

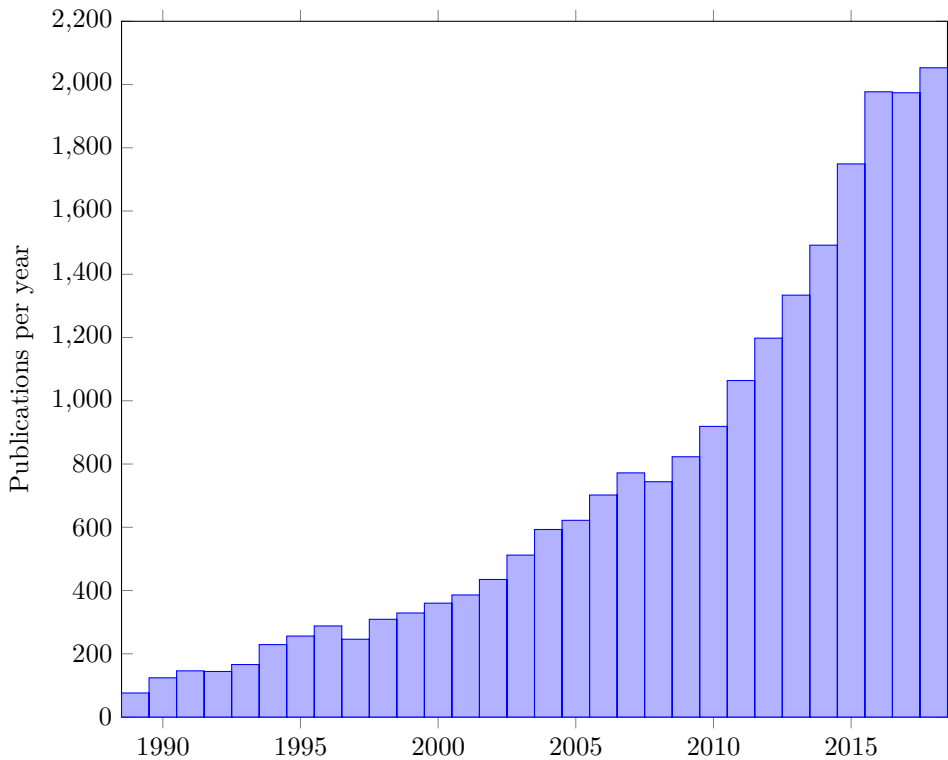


Figure 1.1.: Annual number of publications on spectral imaging during the life of the author [1].

In this context, it is not surprising that the Academisch Medisch Centrum (AMC)¹, the largest hospital of Amsterdam with a connection to the Universiteit van Amsterdam, decided to start a research project on spectral imaging in 2012. Together with the Technische Universiteit Delft (TU Delft), the Saxion Hogeschool

¹Since 2018: Amsterdam Universitair Medisch Centrum (Amsterdam UMC)

and the support of Dutch industry partners Avantes BV, Anteryon BV, Forensic Technical Solutions (FTS)², and later DEMCON Focal, they created “The Spectr@phone” project. The aim was to develop a hand-held spectrometry and multispectral imaging tool for forensic and medical applications, more specific the development focussed on the age determination of bruises.

1.1. Bruises as an indicator for child abuse

Since the beginning of the 90s child abuse has been put into the focus of scientific research after denying the problem for decades [2]. There are numerous forms of child abuse all having long-term effects on the physical and mental health of the affected children [3, 4]. One example is physical abuse, indicated by the presence of multiple bruises, which can be detected during regular check-ups by a doctor. Legal actions however have a serious impact on the life of a family and should therefore be taken with great caution. Unusual locations as well as a uniform shape of bruises indicate child abuse. One factor that can help detecting child abuse is the age of a bruise which had been impossible to detect for a long amount of time.

1.1.1. Bruise formation

A bruise is created when an external force breaks a skin layer and blood accumulates in the subcutaneous tissue. The blood diffuses into the upper skin layers of the dermis and forms a visible discolouration. The colouring is mainly caused by the chromophores: haemoglobin (red/blue) and bilirubin (yellow). Their visibility depends on their location in terms of depth and diffusion, their amount, the skin pigmentation, and the oxygenation of the haemoglobin [4].

The colour of a bruise changes over time and depends on a series of biological processes, which in turn depend on the age and gender of the child. The red haemoglobin diffuses in the dermis and is enzymatically converted to bilirubin during the healing process of the wound [6]. Bilirubin however diffuses faster than haemoglobin creating yellowish rings around the red/blue haemoglobin areas (Fig. 1.2) of a bruise. The knowledge about these colour changes has been summarised in look-up tables, but the variations in the colours and their descriptions makes their legal use impossible [7].

To objectively determine the colour of a bruise, scientists have tried to use reflectance spectroscopy to determine the concentration of each chromophore inside the skin (Fig. 1.3). But the complex nature of bruises makes estimating the age difficult when analysing the spectrum of the skin in only one position. The chromophores move in the skin and make determining the optimal reference point challenging. Many important factors influence the colour composition of a bruise including the size and depth of the bruise and different tissue types and thus effect the spectroscopic measurement. Separating their influences to determine the age cannot easily be done with point spectroscopy.

²Now: fortechs

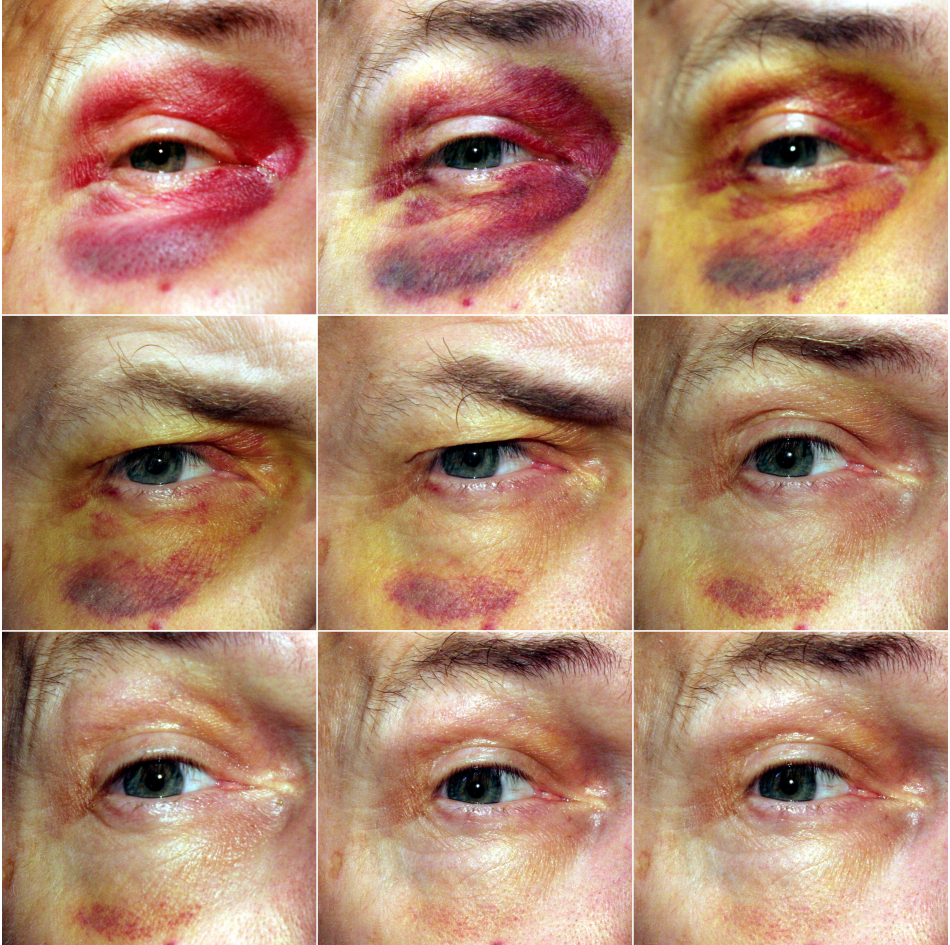


Figure 1.2.: Healing of a black eye over a 9-day period caused by a wisdom tooth extraction [5].

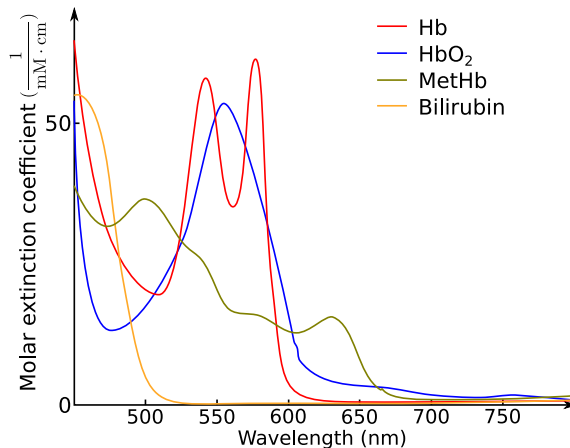


Figure 1.3.: Molar extinction coefficient of oxygenated (HbO_2) and desoxygenated haemoglobin (Hb), methaemoglobin (metHb), and bilirubin [8].

1.1.2. Hyperspectral investigation of bruises

The appearance of spectral cameras on the market enabled new analysis techniques that wouldn't be possible with reflectance spectroscopy in only one point of the bruise. In spectral imaging the colour spectrum is measured in each image point and in consequence gives information about the bruise in each point at the same time. Most spectral imaging methods are based on a scan over time, since 2D camera sensors cannot obtain 3D information in a single shot. Therefore, the 3D datacube is either scanned spatially, or spectrally. The additional information obtained by spectral imaging can then be used to localise the haemoglobin and bilirubin in the bruise.

1.2. Age determination

Determining the age of a bruise however is non-trivial. The mechanism of blood diffusion and the healing process differs depending on the position and depth of the bruise. The following model is based on the work of Randeberg and Stam [4, 6, 9] and has been further developed by Richelle Hoveling during the course of the Spectr@phone project. A simulation of the time- and space-dependent behaviour of bruises enables accurate age determination of bruises. The simulation is based on a finite element method (FEM) model of the bruise that uses the different dynamics of haemoglobin and bilirubin to describe the healing behaviour.

This skin model consists of three layers resembling the dermis (top and middle layer) and the subcutaneous layer (bottom layer). The starting point of the simulation is a haemoglobin pool of arbitrary shape and size in the subcutaneous layer that resembles the initial injury causing the bruise. In consequence the model does not describe bruises containing open wounds. The chromophore concentration in

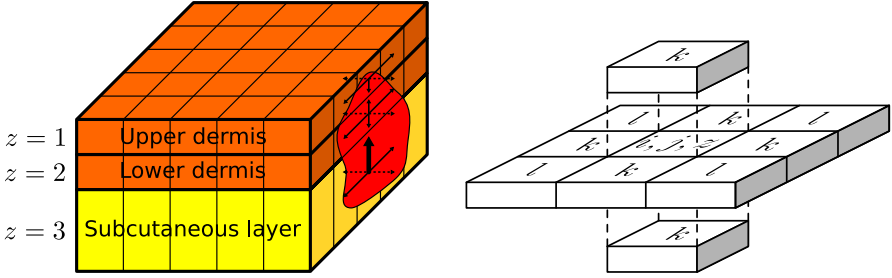


Figure 1.4.: FEM skin model. (a) The skin is divided three layers z . A schematic blood pool spreading from the subcutaneous layer into the dermis is indicated in red. (b) Element indexing of adjacent compartments k and l as used in the formulas.

each finite element is influenced by three processes: First the convection from the subcutaneous layer into the dermis. Second the vertical diffusion between the layers and horizontal diffusion within the layers. Third the enzymatic conversion of bilirubin to haemoglobin. The fluid transport of haemoglobin in vertical direction is given by Darcy's law [10]. The diffusion is described by Fick's first law [11, 12]. The conversion of haemoglobin to bilirubin is described by Michaelis-Menten kinetics [13]. In the second layer ($z = 2$), the mass rate of haemoglobin is

$$\begin{aligned} \frac{\Delta[\text{Hb}]_{i,j,z}}{\Delta t} = & \left(\frac{[\text{Hb}]_{i,j,z+1}}{V_{z+1}} \frac{K \Delta p_{z+1;z} A_{z+1;z}}{\Delta x_{z+1;z}} \right) + \\ & + D_{\text{Hb}} \left(\frac{1}{6} \sum_k \left(\frac{\Delta N_{\text{Hb}} A}{\Delta x} \right)_{i,j,z;k} + \frac{1}{4} \sum_l \left(\frac{\Delta N_{\text{Hb}} A}{\sqrt{2} \Delta x} \right)_{i,j,z;l} \right) - \\ & - \frac{V_{\max} [\text{Hb}]_{i,j,z}^*}{K_m + [\text{Hb}]_{i,j,z}^*} [\text{HO}] M(\text{Hb}). \end{aligned} \quad (1.1)$$

The first term on the right-hand side describes the flow out of the subcutaneous layer into the lower dermis. Therefore, this term is zero in the upper dermis ($z=1$) and its sign is inverted in the subcutaneous layer ($z=3$). The second term describes the diffusion between neighbouring elements and the third term the conversion of haemoglobin to bilirubin. All variables are listed in Table 1.1. The meaning of the indices is depicted in Figure 1.4. i and j are the coordinate indices of an element within a layer $z \in \{1; 2; 3\}$. k resembles all nearest neighbour elements and l the four nearest diagonal elements within the same layer z . Haemoglobin, bilirubin, and heme oxygenase are abbreviated with Hb, B, and HO, respectively. The molar masses of haemoglobin and bilirubin are $M(\text{Hb}) = 65 \frac{\text{kg}}{\text{mol}}$ and $M(\text{B}) = 0.584 \frac{\text{kg}}{\text{mol}}$, respectively.

Quantity	Abbreviation	Unit
Time step	Δt	s
Mass of Hb, HO, B	[Hb], [HO], [B]	kg
Volume of the element	V	m^3
Hydraulic conductivity	K	$\frac{\text{m}^4}{\text{Ns}}$
Pressure difference between layer $z + 1$ & z	$\Delta p_{z+1,z}$	$\frac{\text{N}}{\text{m}^2}$
Contact surface of two elements	A	m^2
Distance between the centres of two nearest neighbour elements	Δx	m
Diffusivity of Hb, B	$D_{\text{Hb}}, D_{\text{B}}$	$\frac{\text{m}^2}{\text{s}}$
Hb density difference between the elements	ΔN_{Hb}	$\frac{\text{kg}}{\text{m}^3}$
Maximum conversion rate per mg of HO	V_{max}	$\frac{\text{mol}}{\text{kg}\cdot\text{s}}$
Molar concentration of Hb	$[\text{Hb}]^* = \frac{[\text{Hb}]}{M(\text{Hb})V}$	$\frac{\text{mol}}{\text{m}^3}$
Michaelis-Menten constant (affinity of an enzyme for a reaction)	K_m	$\frac{\text{mol}}{\text{m}^3}$
Molar mass of Hb, B	$M(\text{Hb}), M(\text{B})$	$\frac{\text{kg}}{\text{mol}}$
Clearance time of B from the lymphatic system	τ_{B}	s

Table 1.1.: Quantities used in Equations (1.1) and (1.2).

The bilirubin mass rate is given in all layers z by

$$\begin{aligned} \frac{\Delta[B]_{i,j,z}}{\Delta t} = & D_B \left(\frac{1}{6} \sum_k \left(\frac{\Delta N_{BA}}{\Delta x} \right)_{i,j,z;k} + \frac{1}{4} \sum_l \left(\frac{\Delta N_{BA}}{\sqrt{2}\Delta x} \right)_{i,j,z;l} \right) + \\ & + 4 \frac{V_{\max}[\text{Hb}]_{i,j,z}^*}{K_m + [\text{Hb}]_{i,j,z}^*} [\text{HO}] M(\text{B}) - \\ & - \frac{[B]_{i,j,z}}{\tau_B}. \end{aligned} \quad (1.2)$$

The first term on the right-hand side describes the diffusion between neighbouring elements. The second term describes the creation of bilirubin from haemoglobin. The additional factor 4 represents the enzymatic reaction creating 4 mol of bilirubin from 1 mol of haemoglobin. The third term describes the clearance of bilirubin into the lymphatic system.

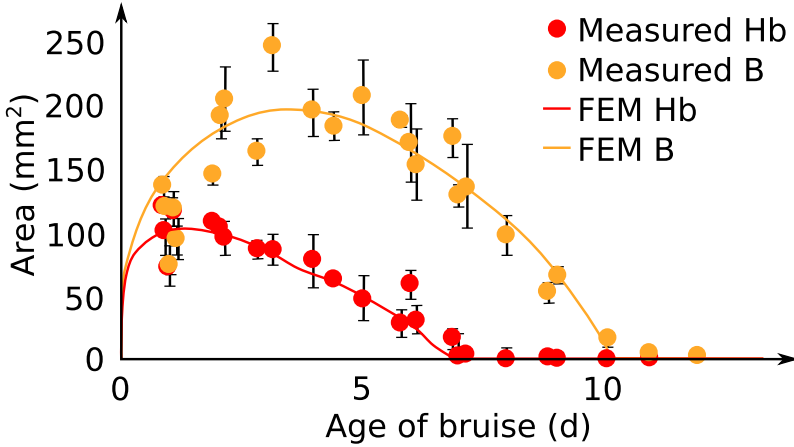


Figure 1.5.: Development of measured haemoglobin (Hb) and bilirubin (B) areas of a bruise compared to the FEM simulation [14].

The FEM model gives insights into the characteristic spreading behaviour of both haemoglobin and bilirubin. This spatial inhomogeneity during the healing process of the bruise can be used to determine the age of a bruise [15]. The different development of the red/blue haemoglobin and the yellow bilirubin area allows retrieving information about the exact age by simply looking at the ratio of both areas. For a known suspect, the age of a bruise has been determined with an accuracy of ± 0.5 h after 26 h and an accuracy of ± 2.5 h after 100 h (Fig. 1.5).

The chromophore areas have to be determined using spectral imaging. Unlike other spectral imaging techniques, it is not necessary to perform hyperspectral imaging on the full visible spectrum. It is possible to measure as little as 9 wavelengths to accurately determine the chromophore concentrations in each pixel. Figure 1.6 depicts, how only two wavelengths can already give an indication, where the two chromophores are located in the bruise.

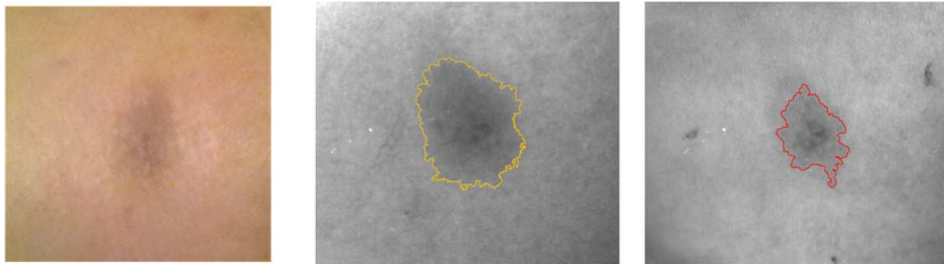


Figure 1.6.: Reflectance images of a bruise for white light (left), at 450 nm (middle), and at 580 nm (right), showing the areas of increased bilirubin (yellow) and haemoglobin (red).

1.3. Development of a new spectral camera

At the AMC this technique had been applied using a liquid crystal tunable filter (LCTF) hyperspectral camera, being the best option available at the time. LCTF filter uses wavelength-dependent birefringence to filter light spectrally. Its working principle is explained in Section 1.3.3. The disadvantage of such a LCTF camera is its low light efficiency and therefore long integration times and gigabyte image files. In consequence, measuring bruises on living people turned out to be impractical. Creating an application-specific spectral imaging device measuring only the necessary wavelengths in a sufficient quality for a decent price has been the main motivation for the Sprectr@phone project.

1.3.1. Requirements

To decide on the best camera design, account has to be taken of the requirements imposed by the medical analysis. A list of essential parameters is shown in Table 1.2. They are based on the requirements of the presented FEM model in Section 1.2, taking account of typical bruise sizes, and ensuring comfortable measurement conditions in the hospital. The short acquisition time is especially important to prevent that the patient can move during the measurement. The main challenge is therefore finding a light efficient spectral imaging device with a sufficient spectral resolution and a large free spectral range to make short integration times possible without having to use an impractical light source. The requirements imposed on the image quality, e.g. working distance, depth of field, and resolution are much less strict than the spectral requirements. Therefore, the choice and development of a spectral filter quickly became the focus of the project.

1.3.2. Spectral imaging basics

Spectral imaging aims to collect all spectral information in each pixel of the image [16]. Hence, the irradiance is measured in a three-dimensional (3D) dataset with the standard space coordinates (x, y) and an additional wavelength coordinate λ . This dataset is called a datacube (Fig. 1.7). The data points of the

Wavelength range	450-650 nm
Spectral resolution	6-15 nm
# of wavelengths	9-12
Spatial resolution	<1 mm
Working distance	20 cm
Object size	10 × 10 cm
Acquisition time	<1 s

Table 1.2.: Specification goals for the Spectr@phone camera

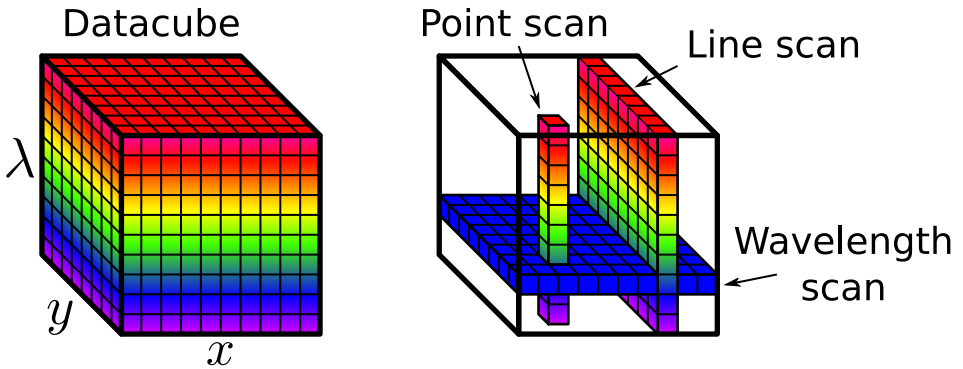


Figure 1.7.: Spectral datacube (left) and spectral scanning strategies (right)

spectral datacube are called voxels (volume pixel = volume picture element). A spectral camera measures the 3D datacube with a two-dimensional (2D) sensor, in consequence most techniques scan the datacube in 2D slices over time. There is a variety of different terms referring to spectral imaging, that became popular during different decades, wavelength regimes, and fields of application, that can be used interchangeably: Spectral imaging, imaging spectroscopy, imaging spectrometry, hyperspectral imaging, and multispectral imaging [17]. Some authors differentiate between those terms, but there is no consistent standard. Multispectral imaging is in general seen as a technique for which more than three but less than 10–25 spectral bands are measured, which separates it from standard RGB cameras and hyperspectral approaches³. However, the boundaries are fluent and often depend on the market they are aiming for. The known spectral imaging techniques can be subdivided into four categories:

- Point-scanning (whisk broom scanners): All classic spectrometers can be used for spectral imaging by simply scanning the whole field of view point by point with one or two mirror galvanometers. This approach mainly finds its application in techniques where point scans are common by default like in optical coherence tomography, confocal microscopy, space telescopes, or satellites.
- Line-scanning (push broom scanners): Line scanning techniques can be applied for most spectrometry techniques and are standard in many airborne/spaceborne systems, that move with a constant speed above their objects, or in industry applications where the product passes the camera on a conveyor belt.
- Wavelength-scanning: Wavelength filters are applied, whenever there is no need to measure all wavelength bands at a time, or the spatial scanning causes unwanted artefacts.
- Snapshot techniques: Non-scanning or snapshot systems obtain the spectral data cube with a single exposure of the detector⁴. Most snapshot techniques are based on either a wavelength or spatial scanning technique but project the information obtained usually obtained during the scan on a different or larger detector unit. Snapshot techniques are the most trending development in the field, but in general come with huge post-processing efforts or drastic trade-offs between spectral and spatial resolution. Therefore they are still barely represented outside of lab environments.

1.3.3. Spectral imaging techniques

The following section gives an overview over some popular techniques and provides background information about the historic availability of spectral imaging techniques.

³A fast tool for determining the age of bruises is therefore a multispectral camera.

⁴This does not necessarily mean that they are faster than scanning techniques.

Spatial-scanning techniques

Spatial scanning techniques rely on dispersion created by either a grating or a prism. Grating and prisms spread the wavelength information along a spatial axis on the detector. Therefore, only one line of the image can be measured simultaneously and the image has to be line scanned. This is advantageous, if the object and the camera are moving with constant speed with respect to each other.

The prism spectrometer is the oldest spectral imaging technique, first developed by P. Jules C. Janssen in the middle of the 19th century. A spinning double-slit monochromator creates a narrowband spectrum. The spectral image is measured by looking through the exit slit and changing the viewing angle with respect to a prism to observe the scene in different wavelengths [17]. Prisms (especially Amici prisms) have ever since been used for spectral imaging and can nowadays be found in many line-scanning spectral cameras.

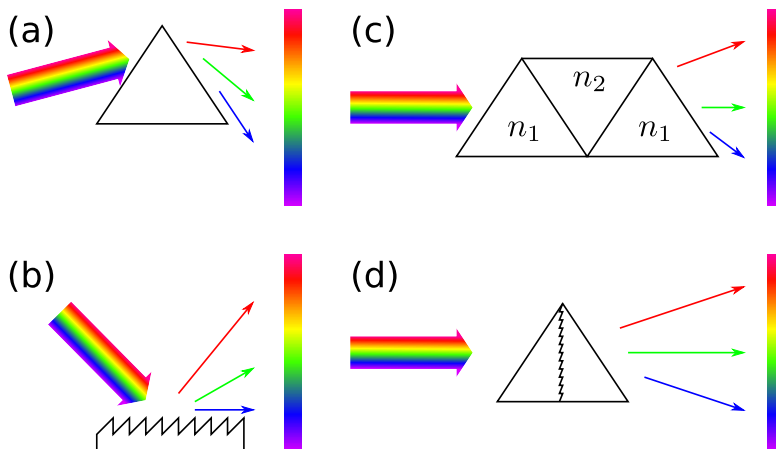


Figure 1.8.: Typical techniques used for line scanning: (a) Prism, (b) grating, (c) Amici prism, (d) Prism grating prism [18].

Grating spectrometers however can be easier customised and are therefore the more popular technique today. Both prism and grating can be combined into a prism grating prism (Fig. 1.8) to amplify each other's effect and to create large separation of wavelengths [18, 19].

Spatial-scanning spectrometers are applied in all kind of applications ranging from satellites [20], fluorescence microscopy [21], measuring retinal oxygen saturation [22] to X-ray applications [23].

Wavelength-scanning techniques

One of the easiest techniques to measure an image wavelength by wavelength is the use of colour filters [16, 24]. Each colour filter transmits only a narrow wavelength band and has to be exchanged between each wavelength measurement with for example a filter wheel (Fig. 1.9). Dichroic colour filters are very light efficient and

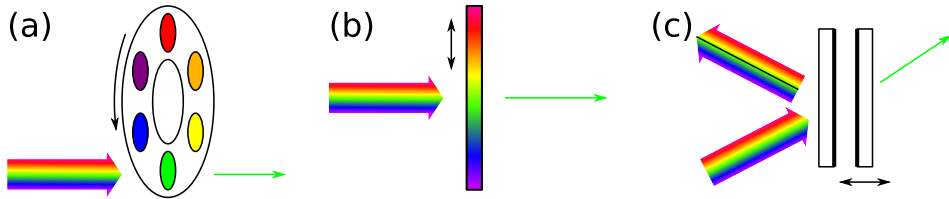


Figure 1.9.: Typical techniques used for wavelength scanning: (a) Filter wheel, (b) Linear variable filter, (c) Fabry-Pérot filter.

useful when only very few wavelengths are required. For more wavelengths the use of linear variable filters is more convenient.

At the end of the 19th century Charles Fabry and Alfred Pérot developed their famous interferometer, the first spectral filter that allowed watching a full scene, while being able to tune the wavelength [25]. A Fabry-Pérot interferometer (FPI) consists of a pair of parallel highly reflecting mirrors. Interference of multiply reflected beams creates very precise fringes and can be used to filter wavelengths. The strength of Fabry-Pérot filters is their ability to scan through wavelengths by changing the distance between the mirrors while maintaining a high spectral resolution. The scan takes a complete image for each mirror configuration.

Due to high manufacturing costs and their difficult alignment FPIs had only been used for high-end spectral imaging in telescope and space applications for many decades [26–30]. With the miniaturisation of electronics and the development of new manufacturing techniques microelectromechanical systems (MEMS)-based FPIs have been manufactured. [31–33]. Alternatively, piezoelectric crystals [34], electro-optics [35], dual tunable Fabry-Pérot devices [35], or liquid crystals [36,37] can be used to scan through the wavelengths. FPIs achieve the highest spectral resolutions and can achieve the highest light efficiency for a given spectral resolution [38].

Liquid crystal tunable filters (LCTF) are based on a sequence of Lyot filters [39]. A Lyot filter firstly linearly polarises the incoming light, secondly sends it through a birefringent crystal and a liquid crystal to turn the polarisation plane over an angle which depends on the wavelength and third through a second linear polariser to filter the wavelengths. The wavelength-dependent birefringent phase retardation can be controlled electrically via the liquid crystal. Figure 1.10 displays how more Lyot filters in series are used to create narrower spectral transmission lines and a larger free spectral range, but this causes additional transmission losses with each additional polariser. LCTFs are very stable, especially in environments with difficult temperature conditions [15, 36, 40–44].

Acousto-optic tunable filters (AOTF) use piezos to create standing waves within a crystal (Fig. 1.11). The acoustic wave induces a density grating that works as an optical grating. The wavelength can be tuned by changing the acoustic frequency by which the grating constant is changed. AOTFs are light-weight spectral filters that can have very large spectral operating ranges (200 nm – 5 μ m) [16, 36, 43–49].

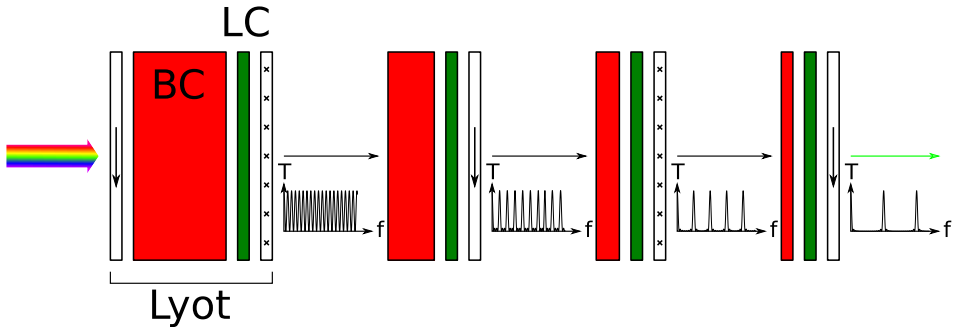


Figure 1.10.: Working principle of a LCTF. The birefringent crystals (BC) are shown in red. Their crystal axes are oriented along the optical axis. The liquid crystals (LC) are shown in green. The polarisers are marked with an arrow or x to indicate their polarising axis. Each unit of polariser(s), birefringent crystal, and liquid crystal is called a Lyot filter. Changing the orientation of the liquid crystal changes the frequency f of maximum transmission T .

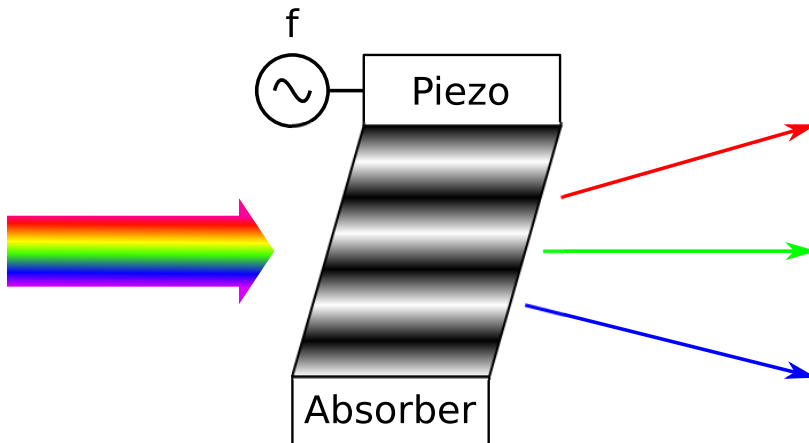


Figure 1.11.: Working principle of an AOTF. A piezo induces an acoustic wave into a crystal. Tuning the frequency f changes the grating constant and the transmission wavelength.

Snapshot techniques

Unlike other scanning techniques spectral images can also be obtained with a single exposure of the detector. This is often achieved by projecting several wavelengths to different parts of a large detector simultaneously.

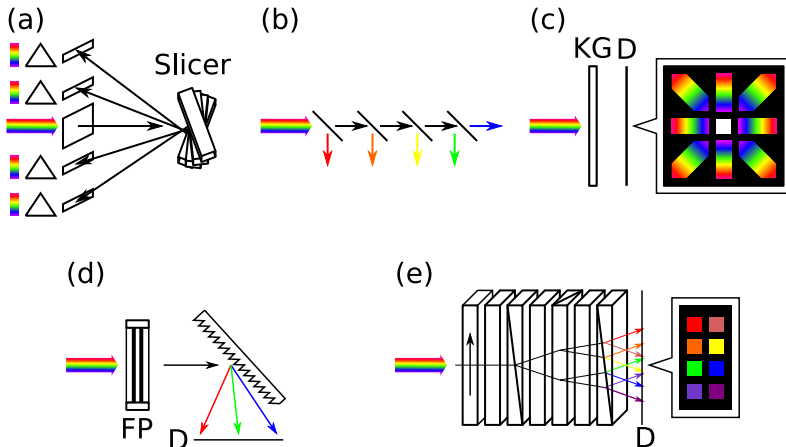


Figure 1.12.: Selected snapshot techniques: (a) Image slicer mirror, (b) Multispectral beamsplitting with dichroic mirrors, (c) Computed tomography imaging spectrometry with a kinoform grating (KG), (d) Tunable echelle imager combining a static Fabry-Pérot (FP) with a grating, (e) Image-replicating imaging spectrometer: A set of a polariser waveplates and Wollaston prisms is used to separate all wavelengths similar to a LCTF filter. Detectors are abbreviated with D.

The first snapshot approach was proposed by Bowen in 1938 [50]. His proposed image slicer is a mirror that reflects each line of the image into a different direction (Fig. 1.12(a)). Each line of the image can then simultaneously be evaluated by an individual spectrometer.

In a similar way an image can be measured with a fibre array, where each fibre can be analysed individually, or an array of lenslets [26, 51–53]. Multispectral beamsplitting is depicted in Figure 1.12(b). It separates the wavelengths with dichroic mirrors/prisms that each send a different wavelength to an individual detector [54]. A multiaperture filtered camera is a camera array each with an individual colour filter, which are often implemented using microlens arrays [55, 56].

The same colour filtering can also be applied at the pixel level in a single camera by increasing the number of filters of the standard RGB Bayer filter [57, 58]. Even though those spectrally resolving detector arrays are very compact and stable, multispectral Bayer filters have been under development for more than 40 years and the technique has not been commonly implemented due to resolution limits and manufacturability problems.

Figure 1.12(d) shows how a Fabry-Pérot interferometer can be combined with a grating to separate multiple transmission wavelengths spatially (tunable echelle

imager) [59]. The principle of a liquid crystal tunable filter (LCTF) can be turned into a snapshot technique by dropping the liquid crystals and splitting up the polarisation after each waveplate (image-replicating imaging spectrometer) with Wollaston polariser prisms (Fig. 1.12(e)). In consequence each band gets spatially spread and subdivided after each Lyot filter [52].

Similar to computed tomography, spectral images can be calculated by making several projections of the spectral datacube (Computed Tomography Imaging Spectrometry) [60–63]. This can be done by designing for example a kinoform grating that, similar to a slit spectrometer, creates multiple projections of the datacube on a single detector chip (Fig. 1.12(c)). Sufficient datacube resolutions therefore require large high resolution detectors. Kinoform dispersers are difficult to fabricate.

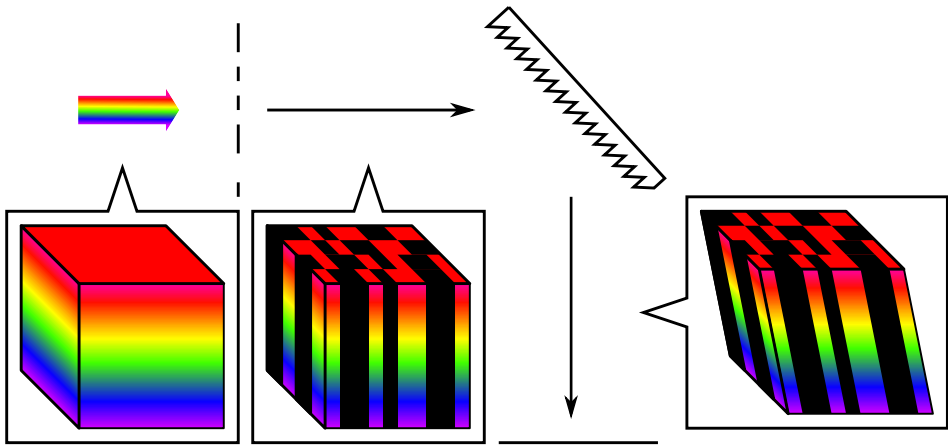


Figure 1.13.: Basic compressive spectral imaging setup with a coded aperture mask and a grating

A nowadays very popular approach is compressive spectral imaging (CSI/CAS-SI). The CSI approach uses compressive sensing to reduce the necessary amount of data that has to be collected to represent the datacube. A spectral image of sufficient quality is calculated afterwards on the computer. Compressive sensing is a signal processing technique that can be used to reconstruct a sparse signal. The signal has to be measured in a sparse basis which can in general be done using far fewer samples. The basis is then transformed back into the usual (cartesian) basis numerically to obtain the full information. Solving the undetermined system of linear equations relies on finding a sparse basis by minimizing the l_1 norm [64–66]. In spectral imaging this technique is usually applied by placing a coded aperture mask in the imaging system (Fig. 1.13). The mask can be both encoded spatially as well as spectrally to get high quality spectral images. The encoded light is then sent through a disperser and measured by a detector [67–78].

Other approaches

Spectral filtering does not have to be done after the light interacts with the object. In some applications it can also be achieved by tuning the light source. This is useful whenever the background noise in the frequency band of interest is negligible. Outside the visible spectrum many techniques tune the wavelength of the light source for spectral imaging. The standard examples are gemstone spectral imaging with X-ray [79,80] and Raman spectroscopy [81]. The general approach has also been tested in the visible regime by using a set of different LEDs [82].

Next to the discussed main approaches there are numerous niche techniques for spectral imaging used in very specific situations. Chromatic aberrations can be used to separate different wavelengths with movable pinhole arrays or Alvarez-Lohmann lenses [83–85]. Photons can also be sorted spectrally using plasmonic nanostructures [86]. Tilting one or more colour filters scans small wavelength regions accurately [87,88] and imaging Fourier transform spectroscopy uses classic interferometers like the Michelson, or Sagnac interferometer to generate a spectral datacube [89–96]. Extended lists of more spectral imaging techniques can be found in the review articles of Garini et al. [16] and Hagen and Kudenov [17].

1.3.4. Comparison of different spectral imaging techniques

All spectral imaging techniques aim for a different trade-off between spectral and spatial resolution, size, applicability in the specific work environment, speed, reliability, post-processing, and margin of error. For the age determination of bruises it is most important that certain wavelengths in the visible range are measured very reliably⁵. When measuring bruises on living bodies it is crucial to optimise the speed of the spectral measurement to avoid errors due to breathing or movements of the patient. These two most important goals are accompanied by the wish for quick post-processing and a cheap and hand-held measurement device.

Developing the best spectral imaging camera within the manufacturing capabilities of the involved companies, all available spectral imaging approaches were evaluated in terms of measurement speed and their spectral and spatial resolutions.

Light efficiency

Spectroscopy techniques can be compared in terms of luminosity, i.e. the total amount of energy transmitted/detected per unit time of a source with unit intensity and their resolving power. The resolving power \mathfrak{R} is the ratio of the wavelength λ and the smallest distinguishable wavelength difference (spectral resolution) $\delta\lambda$: $\mathfrak{R} = \lambda/\delta\lambda$. For the three main spectroscopy techniques the prism, the grating, and the FPI, the luminosity for a given resolving power can be expressed analytically. For lossless transmission, the flux passing through a prism or grating spectrometer is [38]:

$$\Phi = \frac{BS\beta\lambda D}{\mathfrak{R}}, \quad (1.3)$$

⁵The necessary accuracy is indicated in Table 1.2.

where B is the luminance of the source, S is the area of the output beam, β is the (identical) angular height of the entrance and exit slits and $D = \partial\alpha/\partial\lambda$ is the angular dispersion. The product SD is different for prisms and gratings. The advantage of a grating over a prism is typically a factor of more than 8, with a minimum of 3, because of the small angular dispersion of common glass or crystalline prisms. Hence, a prism is always inferior to a grating spectrometer in terms of luminosity. The flux passing through an ideal Fabry-Pérot spectrometer is:

$$\Phi = \frac{\pi^2}{2} \frac{BA}{\mathfrak{R}}, \quad (1.4)$$

where A is the area of the Fabry-Pérot spectrometer. The ratio of the flux passing through a Fabry-Pérot and the grating spectrometer can be reduced to $\pi^3/(4\beta)$ [38]. Since the angular height β of the entrance slit has to be chosen $<1/10$, measuring with a Fabry-Pérot spectrometer typically allows a luminosity gain of 30 to 400 compared to a grating spectrometer. The higher light throughput of the Fabry-Pérot spectrometer allows shorter acquisition times per wavelength and therefore speeds up the entire measurement. Other interference-based techniques like the Michelson interferometer can be described in the same way as the Fabry-Pérot spectrometer and have no advantage in terms of luminescence for a given resolving power \mathfrak{R} . The difference is that Fabry-Pérot cavities reach higher spectral resolutions than single-pass interferometers.

Most spectral imaging techniques can be associated by their working principle with one of the three described techniques. AOTFs for example use an acoustic grating while LCTFs use a set of Lyot filters, which work like a series of Michelson interferometers but each with significant losses due to the polarisers.

1.3.5. Development of a demonstrator camera

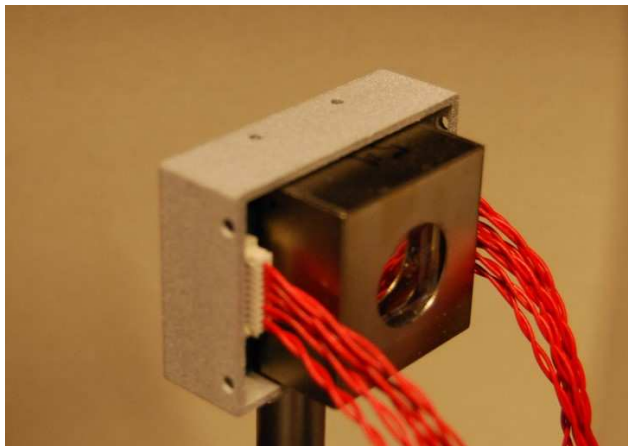


Figure 1.14.: Fabry-Pérot interferometer by Rikola

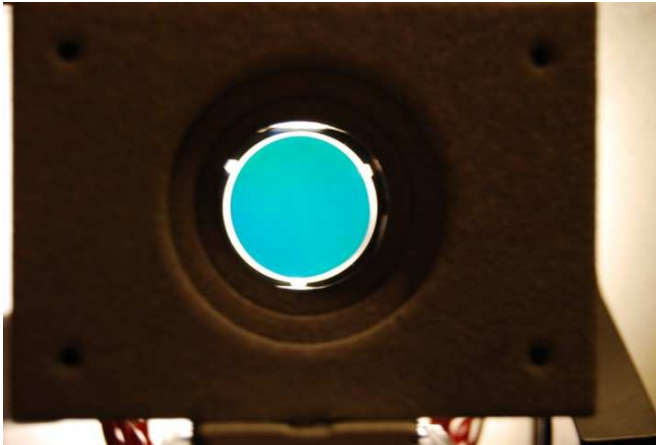


Figure 1.15.: Transmission through the Rikola Fabry-Pérot interferometer.

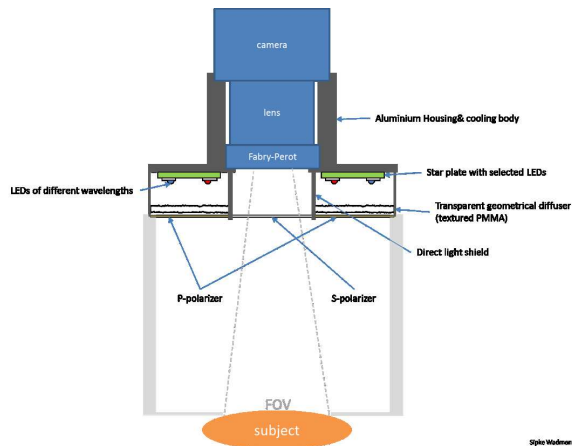


Figure 1.16.: Schematic demonstrator using a set of LEDs to distinguish between multiple orders of the Fabry-Pérot transmission.

Applying the best performing spectroscopy technique, the Fabry-Pérot spectrometer, has been difficult in the past due to manufacturability problems. While it has been applied for spectral imaging in space applications for many decades, low-cost mass-producible FPIs have only been available recently. To test the feasibility of the technique, a MEMS-based Fabry-Pérot interferometer has been bought from the only supplier on the market, the Finnish startup Rikola⁶. The FPI has been developed by the VTT Technical Research Center of Finland. The module is shown in Figure 1.14 and Figure 1.15. A scheme of the demonstrator built at Avantes is displayed in Figure 1.16.

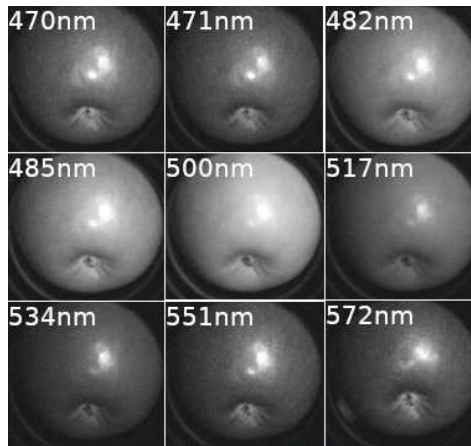


Figure 1.17.: First spectral image of a green apple captured with the spectral camera demonstrator by Albert Borreman at Avantes

The first trials were successful and motivated to put further effort into developing an own Fabry-Pérot interferometer at Anteryon. The first spectral images taken with the demonstrator camera are displayed in Figure 1.17. The original idea of developing a spectral camera for determining the age of bruises using a Rikola FPI failed at a very early stage of the project and purchasing the component was decided to be too expensive for our final application purpose. The VTT had decided to use the Rikola FPI in a different project for a similar market and therefore decided to withdraw their support and participation from the Spectr@phone project. A different solution had to be found, both profiting from the manufacturing strengths of Anteryon and circumventing the patents of VTT. Therefore our own Fabry-Pérot interferometer was developed and designed in detail for the project, shifting the focus from the design of a spectral camera entirely towards the design of the spectral filter.

⁶Rikola was acquired by Senop in 2016.

1.4. Design of the Fabry-Pérot interferometer

The design challenges and resulting decisions on how to manufacture a FPI and the necessary theoretical background is explained in this section. The theoretical results are followed by brief examples to explain the major design decisions.

1.4.1. Basic concept

The principle of a Fabry-Pérot interferometer has been understood since the 19th century and not changed much since then. A Fabry-Pérot interferometer consists of two highly reflecting mirrors facing each other. The spacing in between the two glass plates is typically in the range of micrometres to centimetres. The spacing defines the transmission wavelengths of the spectrometer. The rear surfaces of the glass plates are often tilted and/or coated with an anti-reflective dielectric layer to avoid unwanted reflections. A Fabry-Pérot etalon instead is a single glass plate with two reflecting surfaces.

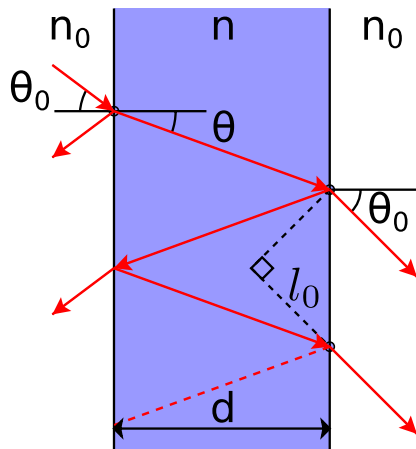


Figure 1.18.: A basic Fabry-Pérot interferometer: An incident beam with angle θ is reflected between two mirrors separated by a material of thickness d and with refractive index n . The mirror gap is shown in blue and the glass mirrors n_0 in white. The medium surrounding the mirrors is not visible at this scale.

Figure 1.18 shows a basic FPI with the two glass mirrors displayed in white and the air gap in blue. The electric field of an incident plane wave that enters the FPI gap from the left under a certain angle θ_0 with the normal on the mirrors of the FPI can be described as:

$$i = E_0 \exp(i(k(x \cos \theta_0 + z \sin \theta_0) - \omega t + \varphi)), \quad (1.5)$$

where x and z are the coordinates perpendicular and parallel to the mirrors of the FPI, respectively, E_0 is the amplitude of the incident electric field, k is the wave

number in the glass mirrors, t is the time, ω is the angular frequency, and ϕ is the phase of the incident field at $x = 0$, $z = 0$ and $t = 0$. The field transmitted by the FPI without any internal reflections is t_0 :

$$t_0 = T \exp\left(i \frac{2\pi n}{\lambda_0} \frac{d}{\cos \theta}\right) i, \quad (1.6)$$

where T is the transmittance of the mirrors (which are assumed to be identical), n is the refractive index of the material in between the mirrors, λ_0 is the vacuum wavelength of the incident light, d is the distance between the mirrors, and θ is the angle between the wave vector and the normal on the mirrors of the FPI. The angles θ and θ_0 are linked by Snell's law $n \sin \theta = n_0 \sin \theta_0$ with n_0 being the index of refraction of the glass plates. For each transmission a factor of \sqrt{T} and for each reflection a factor \sqrt{R} , where R is the reflectance of the mirrors, is multiplied to the amplitude. For each reflection at the glass mirrors the phase changes by π . The second factor of the exponent describes the travelled distance of the light and the first factor converts it into a phase. The field exiting the FPI after two reflections passes the gap three times and hence has amplitude:

$$t_1 = TR \exp\left(i \frac{2\pi n}{\lambda_0} \frac{3d}{\cos \theta}\right) i. \quad (1.7)$$

To calculate the interference between two succeeding fields one must not forget, that the field t_0 has to travel an additional distance l_0 outside of the gap to interfere with t_1

$$l_0 = 2d \tan \theta \sin \theta_0. \quad (1.8)$$

The phase difference between two succeeding beams is therefore:

$$\phi = 2n \frac{2\pi}{\lambda_0} \frac{d}{\cos \theta} - \frac{2\pi}{\lambda_0} 2n_0 d \tan \theta \sin \theta_0 \quad (1.9)$$

$$= \frac{2\pi}{\lambda_0} 2nd \left(\frac{1}{\cos \theta} - \tan \theta \sin \theta \right) \quad (1.10)$$

$$= \frac{2\pi}{\lambda_0} 2nd \cos \theta. \quad (1.11)$$

In consequence all succeeding transmitted fields can be described as

$$t_m = TR^m e^{im\phi} i, \quad (1.12)$$

for all integers $m \in \mathbb{N}_0$. The amplitude of the the total transmitted field is:

$$t = \sum_{m=0}^{\infty} t_m = T \sum_{m=0}^{\infty} R^m e^{im\phi} i = \frac{T}{1 - Re^{i\phi}} i. \quad (1.13)$$

The transmitted intensity is the modulus squared of the field:

$$\mathcal{T} = tt^* = \frac{T^2}{1 + R^2 - 2R \cos \phi} E_0^2. \quad (1.14)$$

This result is known as the Airy function⁷

$$\mathcal{A}(\phi, R) = \frac{1}{1 + F(R) \sin^2 \frac{\phi}{2}} E_0^2. \quad (1.15)$$

with the coefficient of finesse:

$$F = \frac{4R}{(1 - R)^2}. \quad (1.16)$$

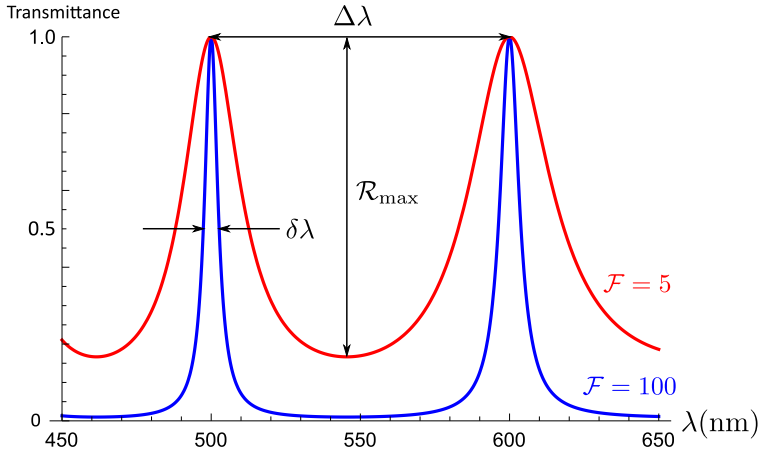


Figure 1.19.: The spectral transmittance of a absorption free FPI under normal incidence $\theta = 0$ (mirror distance $d = 1500 \text{ nm}$, $n_{\text{Air}} = 1$, $E_0^2 = 1$)

The Airy function is shown in Figure 1.19. The absorptance A of the mirrors can be included with a simple additional factor:

$$\mathcal{T}' = \left(1 - \frac{A}{1 - R}\right)^2 \mathcal{A}(\phi, R). \quad (1.17)$$

Most other important characteristic parameters of a FPI can be derived easily using this equation. The transmittance is maximal, whenever $\sin^2(\phi/2) = 0$. Transmission peaks can therefore be observed for $\phi = 2\pi m$ for $m \in \mathbb{N}$. The minimum of the transmittance function \mathcal{T} defines the maximum reflectance of the FPI \mathcal{R}_{max} , i.e. the maximum suppression of all wavelengths outside the transmission

⁷Using the trigonometric identity: $\cos(x) = 1 - 2 \sin^2\left(\frac{x}{2}\right)$.

peaks

$$\mathcal{R}_{\max} = \frac{4R}{(1+R)^2} E_0^2. \quad (1.18)$$

The free spectral range (FSR) $\Delta\lambda$ of a FPI is the wavelength difference between two neighbouring transmission peaks at $\lambda_1 - \Delta\lambda$ and λ_1 .

$$\Delta\lambda = \frac{\lambda_1^2}{2n_g d \cos\theta + \lambda_1}, \quad (1.19)$$

where $n_g = n - \lambda_0 \times dn/d\lambda_0$ is the group refractive index. Detecting the age of bruises requires a FSR of $\Delta\lambda = 200 - 250$ nm (Tab. 1.2). To achieve the required spectral resolution of $\delta\lambda = 6 - 15$ nm for normal incidence for wavelengths in the range of $\lambda = 650 - 700$ nm without extra filtering, the mirror gap d has to be smaller than the FSR $\Delta\lambda = 731$ nm to transmit at $\lambda_1 = 650$ nm and $\Delta\lambda = 630$ nm at $\lambda = 700$ nm. In consequence the mirror gap can only be operated in two configurations while avoiding multiple transmission peaks within the region of interest: The zeroth transmission requires gaps of $d = 225 - 350$ nm to scan the full wavelength range $\lambda = 450 - 700$ nm. Such small mirror distances are very hard to achieve and control and therefore the second option has been chosen: Tuning the mirror gap in the range of $d = 450 - 650$ nm covering a slightly smaller wavelength range $\lambda = 450 - 650$ nm. The mirror distance is identical to the transmission wavelength. A mirror reflectivity of $>94\%$ is required to achieve the necessary spectral resolution of $\delta\lambda = 6 - 15$ nm if the thickness of the FPI gap is one wavelength. The finesse of the resonator is given by

$$\mathcal{F} = \frac{\Delta\lambda}{\delta\lambda} = \frac{\pi}{2 \arcsin\left(\frac{1}{\sqrt{R}}\right)}, \quad (1.20)$$

with $\delta\lambda$ being the full width at half maximum (FWHM) of a transmission peak. The resolving power is

$$\mathfrak{R} = n\mathcal{F}. \quad (1.21)$$

The finesse/resolving power of an FPI for spectral imaging of bruises has to be larger than 48 (Tab. 1.2).

The spectral behaviour of high finesse FPIs can also be described as a superposition of Lorentzian⁸ functions $L(x; x_0, \gamma)$:

$$\mathcal{T} = 2\pi \frac{1-R}{1+R} \text{III}\left(\frac{\phi}{2\pi}\right) L(\phi; 0, -\ln(R)) E_0^2, \quad (1.22)$$

with the Dirac comb $\text{III}(\phi/2\pi) = \sum_{n=-\infty}^{\infty} \delta(\phi/(2\pi) - n)$ [97-100].

⁸Very useful for convolutions.

1.4.2. Mirror coatings

The derived model describes a FPI using metal mirrors (typically Ag) with a single coating layer accurately. The disadvantage of a metal coating is its high absorption. A FPI using two Ag-coated mirrors (45 nm) with a reflectivity of 90% absorbs already 88% of the intensity⁹. The only way to avoid high absorptions is the use of dielectric coatings. Dielectric mirror coatings reflect the light at an interface by using a stack of multiple layers. Each layer can consist of a different material with its own refractive index and thickness.

Multilayer mirrors

The basic model is based on the assumption that the problem can be treated purely geometrically. It is sufficient to describe highly reflecting thin metal mirrors with a high reflectance. However, such mirrors also slightly absorb light with each reflection in the FPI. In contrast, multilayer mirrors show hardly any absorption losses. If the transmission is calculated with a multilayer model, the physical effects at a sub wavelength range have to be taken into account.

The basis of calculating the transmittance and reflectance is identical to the standard model for a FPI. A plane wave is incident on a planar interface between two media. Maxwell's equations determine the behaviour of the fields at the boundary and yield the well-known Fresnel equations. In a multilayer stack however, the boundary conditions are applied at each interface and the fields are propagated in between over short distances. This leads to a set of equations that can be written using a matrix model. Every layer of the stack corresponds to the multiplication by a transmission matrix to describe the behaviour of the whole stack. A thorough derivation can be found in H. Angus Macleod's book "Thin-Film Optical Filters" in chapter 2 [102]. A quick summary of the results will be provided here, because we use this model later to calculate the transmission spectra.

Each layer r in a multilayer stack can be described by a matrix M :

$$M_r = \begin{pmatrix} \cos \phi_r & i \frac{\sin \phi_r}{\eta_r} \\ i \eta_r \sin \phi_r & \cos \phi_r \end{pmatrix}. \quad (1.23)$$

The phase difference within a layer r

$$\phi_r = \frac{2\pi n_r d_r}{\lambda} \cos \theta_r, \quad (1.24)$$

is given by the layer thickness d_r , the complex index of refraction of the layer n_r and the angle of incidence within the layer θ_r . The optical admittance describes the ratio of H and E fields in the layer and is different for both s- (\perp) and p-

⁹ $\lambda = 500 \text{ nm}, \theta = 0^\circ, n = 0.060, \text{ extinction coefficient } \kappa = 3.6$ [101]

polarisation (\parallel):

$$\eta_{\parallel} = n_r \cos \theta_r \quad (1.25)$$

$$\eta_{\perp} = \frac{n_r}{\cos \theta_r}. \quad (1.26)$$

The angle of incidence in a layer is given by Snell's law:

$$\theta_r = \sin^{-1} \left(\frac{n_0}{n_r} \sin(\theta_0) \right), \quad (1.27)$$

where n_0 is the index of refraction of the medium in front of the stack. A stack of layers can again be expressed as a single matrix by multiplying the matrices of each layer¹⁰:

$$M = M_1 M_2 \dots M_N. \quad (1.28)$$

The final E and H -fields then follow directly from the initial fields:

$$\begin{pmatrix} E_{N+1} \\ H_{N+1} \end{pmatrix} = M \begin{pmatrix} E_0 \\ H_0 \end{pmatrix} \quad (1.29)$$

$$\begin{pmatrix} B \\ C \end{pmatrix} = \begin{pmatrix} E_{N+1}/E_0 \\ H_{N+1}/E_0 \end{pmatrix} = M \begin{pmatrix} 1 \\ \eta_{N+1} \end{pmatrix}. \quad (1.30)$$

Dividing the resulting fields by the initial electric field E_0 simplifies the calculation and introduces the ratios B and C . The transmittance \mathcal{T} and reflectance \mathcal{R} of the multilayer stack are:

$$\mathcal{T} = \frac{4\eta_0 \operatorname{Re}(\eta_{N+1})}{(\eta_0 B + C)(\eta_0 B + C)^*} \quad (1.31)$$

$$\mathcal{R} = \left(\frac{\eta_0 B - C}{\eta_0 B + C} \right) \left(\frac{\eta_0 B - C}{\eta_0 B + C} \right)^*. \quad (1.32)$$

The matrix formalism reduces the problem of calculating the multilayer transmittance layer by layer to a simple straight forward matrix multiplication, in which nothing more than the complex index of refraction n_r and the thickness of each layer d_r have to be known. The formalism can be used to calculate the transmittance, absorptance, and reflectance for both polarisation states and all angles of incidence θ .

1.4.3. Comparison of a single and a multilayer example

The advantage of a dielectric multilayer mirror coating is the absence of absorption, which is typically higher than 85% for silver mirrors as mentioned before. But mirrors made of multilayer coatings are more difficult to fabricate and their design is non-trivial. Creating a Fabry-Pérot cavity with multilayer-coated mirrors for

¹⁰The index 0 indicates the medium in front of the stack, while $N + 1$ indicates the medium behind it.

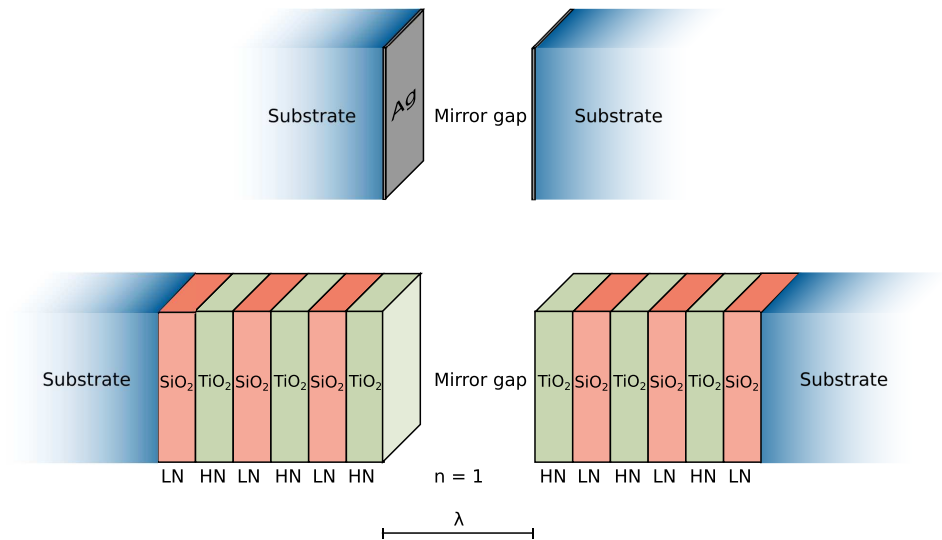


Figure 1.20.: The first sketch shows a Fabry-Pérot interferometer using a single layer silver coating. The thickness of the Ag layer is $\ll \lambda$. The second sketch shows a multilayer coating. The layers have an optical thickness of a quarter wavelength. The refractive indices at $\lambda = 550 \text{ nm}$ are $\text{HN} = 2.543$ and $\text{LN} = 1.460$ [101].

single wavelength however is well understood. A quarter wavelength stack of alternating layers of high (HN) and low refractive index (LN) materials creates a good mirror that is optimised for a single wavelength and can be used to further analyse the FPI properties. To create a mirror coating that is optimal for the full spectral range of the FPI, further optimisation of the layer thicknesses is needed. An example of a multilayer coating consisting of a Substrate|(SiO₂|TiO₂)₃ quarter wavelength stack¹¹ (Fig. 1.20) shows a mirror reflectivity of $\approx 91\%$ for 550 nm with hardly any light absorbed.

As found in Section 1.4.1, the mirror gap necessary for the Spectr@phone is equal to the wavelength under normal incidence measured in the material in between the FPI mirrors and therefore thinner than a typical mirror coating. Hence, one cannot just calculate the reflectance of a dielectric mirror and put it into the geometric FPI model (1.15). The geometric model assumes infinitesimal mirror coating thicknesses and only takes account of the interference within the cavity. All phase information from within the coatings is omitted. It can however be extended to describe multilayer coatings [103]. The standard approach is treating the mirror gap as an additional layer in the multilayer stack to correctly determine the transmittance of a dielectric FPI. Both mirrors and the air gap are calculated as a single multilayer stack.

The different transmittances for a dielectric mirror and a silver mirror FPI with

¹¹Notation of multilayer stacks: |: Surface between two adjacent materials.

()_x: The layer or combination of layers within the brackets is repeated x times.

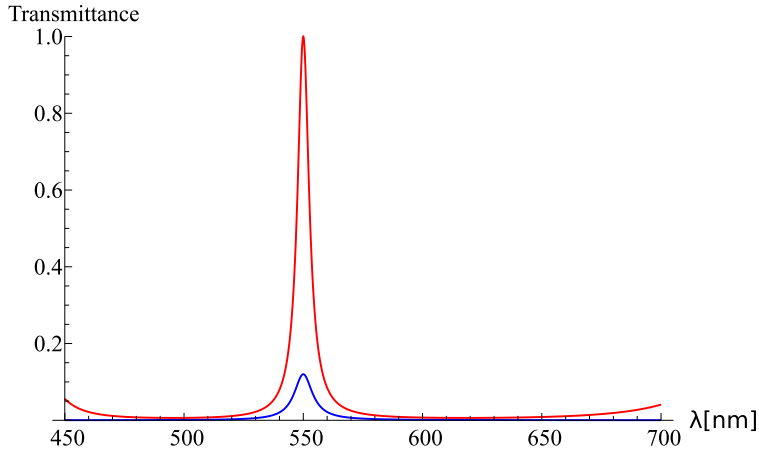


Figure 1.21.: The transmission through a Ag Fabry-Pérot etalon is plotted in blue and the transmission through a multilayer Fabry-Pérot is shown in red. The used parameters are: $d = 550 \text{ nm}$, $\theta = 0^\circ$. The thickness of the Ag layer is 45 nm. The multilayer is quarter wavelength stack of Substrate|(TiO₂|SiO₂)₃.

similar mirror reflectance ($R_{\text{Ag}} = 0.90$, $R_{\text{Substrate}|(\text{TiO}_2|\text{SiO}_2)_3} = 0.91$) are displayed in Figure 1.21. Both FPIs achieve the same spectral resolution, but the maximum transmittance of the Ag mirrors is much lower than for the multilayer mirrors. The dielectric coatings are optimised for 550 nm and therefore the reflectivity drops for far away wavelengths. In consequence, the FPI performance decreases around 450 nm. This can be avoided by optimising the layer thickness and materials of the dielectric mirrors. Also the shifting behaviour of the transmission peak changes when tuning the mirror gap with dielectric mirrors and becomes less intuitive. Dielectric coatings are strongly wavelength dependent, while silver coatings barely are, so to create a dielectric FPI with the same shifting behaviour as a silver FPI one would require the thickness of the coating layers to scale with the mirror gap, which is impossible with known manufacturing techniques.

1.4.4. Surface roughness

The principle of a FPI is known for more than a century. Ways to overcome its flaws are known. So why is there only one manufacturer of usable FPIs for spectral imaging on the market? The answer is: tight tolerances. The performance of an FPI is highly sensitive to mirror imperfections, that destroy the perfect parallelism of the mirrors. To achieve a decent performance the sum of the root mean square (RMS) surface roughness of both mirrors has to be below the desired 6 nm linewidth otherwise the transmission peak is broadened and shrinks. In comparison the thickness of a quarter wavelength layer of TiO₂ and SiO₂ are 55 nm and 94 nm, respectively. The total coating thickness is therefore 149 times larger than the tolerable surface roughness. In other words the layer deposition has to

be done perfectly on very flat mirrors. Next to the 'natural' mirror roughness the mirrors have to be moved with great care. Since the mirrors have to be larger than 1 cm^2 to be used for spectral imaging, the aspect ratio between mirror gap and mirror width is 1:20000. Smallest mistakes during the movement of the mirrors can bend the mirrors, glue them together eternally, or break the required parallelism. Therefore it was crucial to investigate the exact implications of different kinds of surface inhomogeneities.

The gap separation of a FPI depends on different parameters like the mirror alignment, curvature, waviness, steps and Gaussian surface roughness. They introduce a shrinkage and broadening of the transmittance peak, which can be expressed by a convolution of a surface distribution function $D(d)$ with the ideal FPI transmittance $\mathcal{A}(\phi(d))$ (See Eq. (1.15)): $\mathcal{A}(d) * D(d)$. Each surface deviation changes the thickness d of the FPI locally. The surface distribution function $D(d)$ measures how often each thickness deviation occurs on a circular mirror. Depending on the surface inhomogeneity the surface deviations are distributed differently. Figure 1.22 illustrates six common inhomogeneities [99].

Type	$D(d)$	σ_D
Tilted	$\sqrt{d_{\max}^2 - d^2}$	$\frac{d_{\max}}{2}$
Spherical	$\text{rect}\left(\frac{d}{2d_{\max}}\right)$	$\frac{d_{\max}}{\sqrt{3}}$
Sine	$-\sqrt{d_{\max}^2 - d^2} + d_{\max}$	$\frac{d_{\max}}{\sqrt{2}}$
Gaussian	$\frac{1}{\sqrt{2\pi\sigma^2}}e^{-\frac{d^2}{2\sigma^2}}$	σ
Step	$\delta(d + d_{\max}) + \delta(d - d_{\max})$	d_{\max}

Table 1.3.: Surface distribution functions $D(d)$ and the standard deviation σ_D of the surface function for given maximum phase errors d_{\max} . The different surface profiles are shown in Figure 1.22.

Table 1.3 lists the effective surface roughness given by the standard deviation σ_D relative to the maximal thickness deviation d_{\max} . Comparing the standard deviations of the distribution functions σ_D for a given maximum thickness deviation d_{\max} allows ranking the surface inhomogeneities by their severity. The worst effect on the spectral resolution has a step in the mirror. This is however a very uncommon defect. Sine shapes as a result of machine polishing rank second and a spherical shape as possibly created by polishing or bending ranks third. The least dramatic effect is caused by a lack of parallelism of the mirrors. Gaussian surface roughness is difficult to put into the ranking because there is no maximum surface deviation d_{\max} but only a standard deviation σ .

The first mirror measurements¹² by Anteryon showed heavily distorted mirror surfaces as displayed in Figure 1.23. The surface deformation is mainly parabolic¹³,

¹²The material of the mirrors was N-BK7.

¹³Not to be confused with paraboloid.

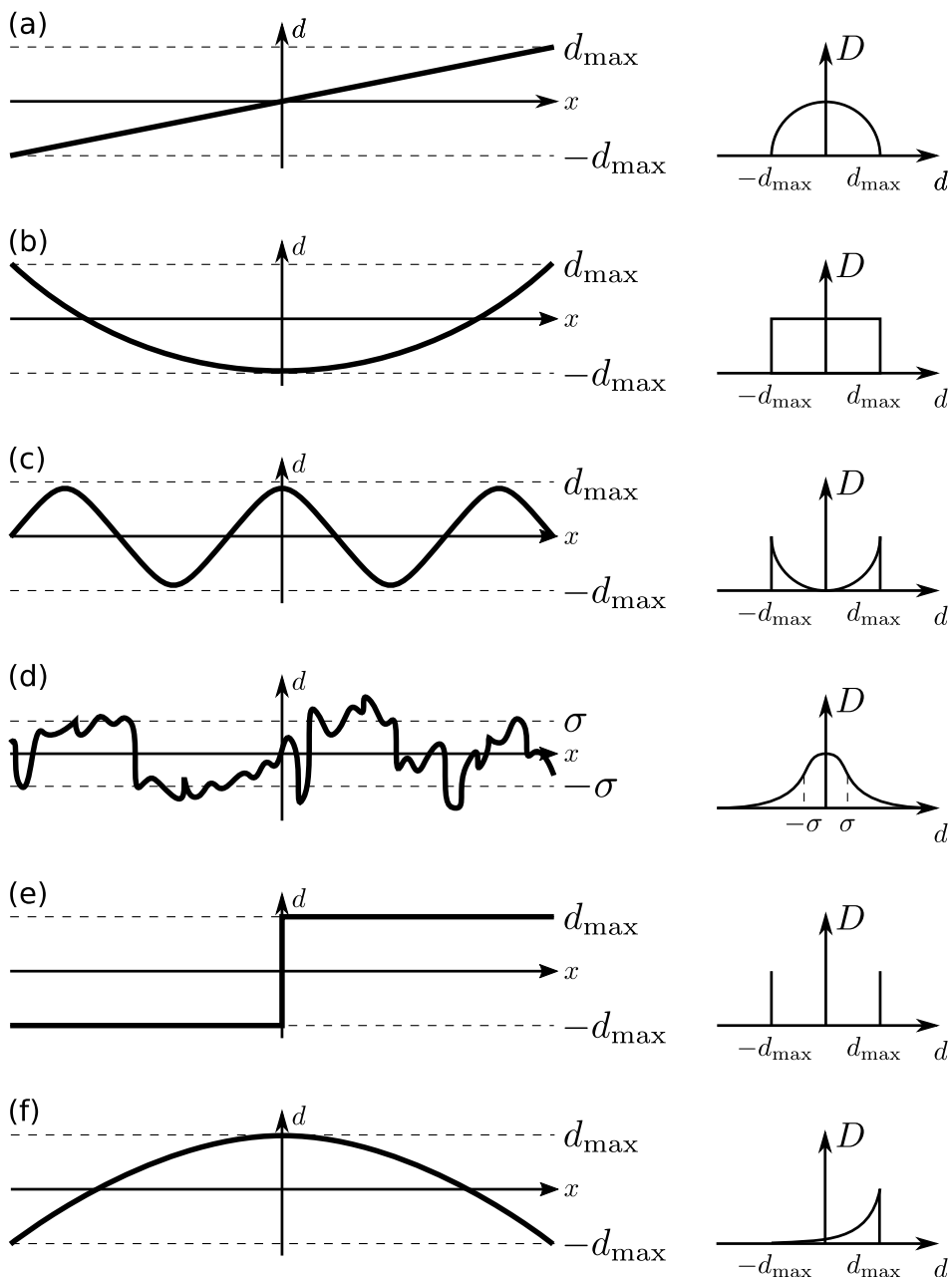


Figure 1.22.: Fabry-Pérot thickness changes d due to surface inhomogeneities plotted along the diagonal x of a circular mirror and the corresponding surface distribution functions for: (a) Tilted mirrors, (b) spherical curved surface, (c) sine surface, (d) Gaussian surface error with standard deviation σ , (e) step, and (f) parabolic surface

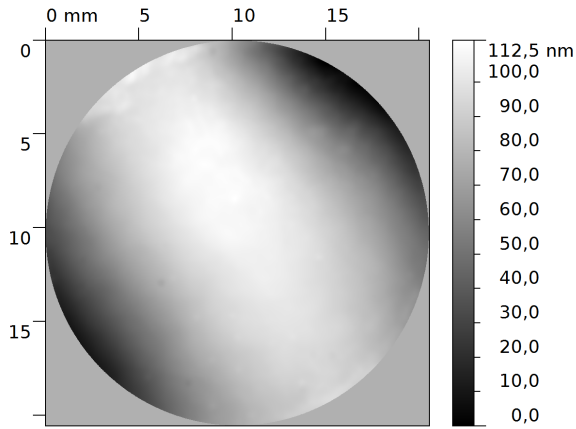


Figure 1.23.: Surface measurement of an early stage mirror measured at Anteryon. The mirror shows a strong parabolic surface deformation, which was observed with two different measurement techniques.

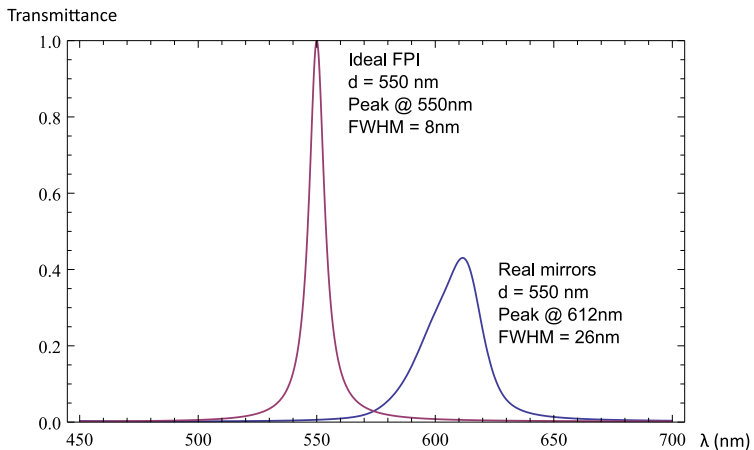


Figure 1.24.: Comparison of an ideal FPI with perfect mirrors to one with the real rough mirror as measured by Anteryon (see Fig. 1.23).

the least problematic surface inhomogeneity investigated. After a subtracting a polynomial fit to the surface profile the remaining RMS surface roughness reduces to 1.3 nm. The effect of the rough mirror on the spectral performance of a FPI is displayed in Figure 1.24. Due to the asymmetry of the surface distribution function, the peak is not only broadened but is also red-shifted. In conclusion, the investigated mirror cannot be used for the spectral camera.

Other factors have less influence on the peak width of the transmittance peaks than the surface roughness. The refractive index of air depends on the pressure and the temperature. The peak wavelength therefore shifts with the refractive index of the medium in between the mirrors (see Eq. (1.11)). The temperature drift is smaller than a nanometre per 10°C and therefore negligible [104]. The cavity can be sealed to avoid other environment influences such as changes in the chemical composition of the air, dust contamination, and pressure changes. The transmission peaks are more broadened for large angles of incidence than for small angles. Such angles however are not necessary to measure bruises as intended (Tab. 1.2).

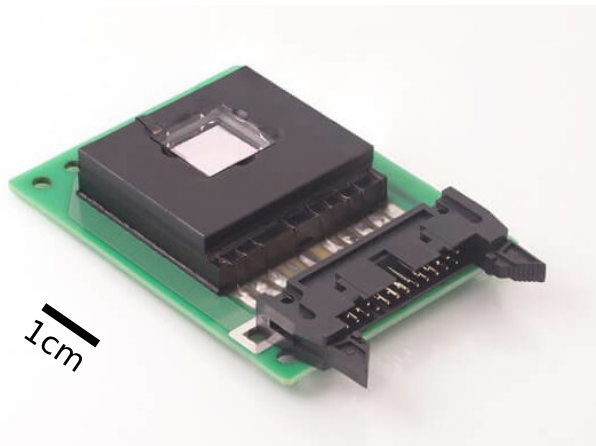


Figure 1.25.: Early FPI prototype made by Anteryon [105].

During further analysis, Anteryon discovered that another one of their machines was able to create much flatter surfaces in-house, than the surface of the D263T glass they intended to buy initially. Based on these mirrors the first prototype was built. Figure 1.25 displays one of the prototypes as shown on the website of Anteryon. The mirror area is 11 mm × 11 mm. The black packaging prevents dust from entering and blocking the FPI. The interface is realised via USB and an internal micro chip controls the mirror position. Later versions have been made even smaller and the final one displayed in Figure 1.26 fits into 30 mm optical cage systems.

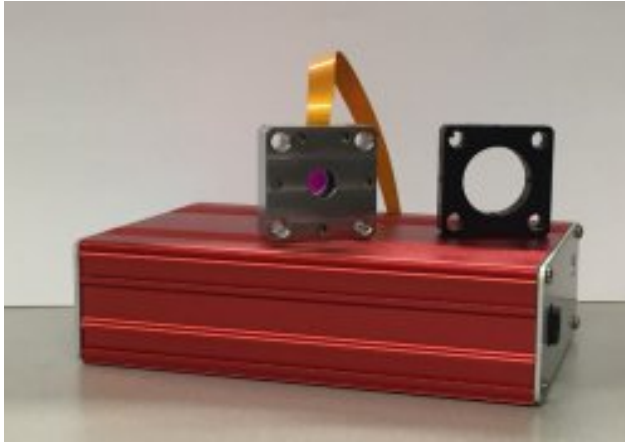


Figure 1.26.: Final FPI prototype made by Anteryon [105]. The prototype has an aperture diameter of 10 mm and fits into a 30 mm optical cage system.

1.5. Optical design

Designing an optical imaging system for the Spectr@phone project was initially thought to be the main focus of the TU Delft contribution. However the requirements on speed and spectral resolution were much tighter than the actual imaging task. The development of a custom optical design for the spectral camera was therefore abandoned. Still, to develop a spectral camera using off-the-shelf objectives, the exact implications of the FPI position in an optical imaging system had to be investigated.

The desired field of view (FOV) of the camera is given by the typical size of bruises and therefore did not need to be optimised for image regions larger than 10×10 cm. In combination with a working distance suited for handheld devices of ≈ 20 cm this requires a full FOV of less than 39° in the corners of the image. In consequence most field angles can still be represented by the paraxial approximation. Also the spatial resolution is not very demanding: 0.5 mm spatial resolution were believed to be sufficient which equals an image size of at least 200×200 px. The size of the optical system was intended to be small enough to fulfil the handheld requirement of the spectral camera. Though desirable, it was not crucial since the main goal was building a camera which is not larger than the already existing LCTF spectral camera with a length of 40 cm.

The optical design can be built by using off-the-shelf components and possibly even by using an entire off-the-shelf camera in combination with the developed Fabry-Pérot filter. However, it is crucial to understand how and where to place the FPI in the optical system. There are two extreme choices to position the FPI in optical systems that both have different advantages regarding spectral resolution and mirror tolerances. The advantages and disadvantages of both extreme choices are studied in the following sections.

1.5.1. Collimated design

The most obvious way to place a Fabry-Pérot filter in an optical system is in a position where all rays coming from an object point are parallel when they enter the FPI. The Airy function (1.15) defines the transmitted spectrum of the ideal FPI as a function of the angle of incidence¹⁴. Such a configuration can be best achieved by putting a collimating lens system in front of the FPI and an additional one behind it to focus the light on a camera sensor¹⁵.

The collimated configuration has two disadvantages. First each object point corresponds to a different angle of incidence at the FPI. The transmission wavelength therefore changes for each field angle. In the context of imaging bruises it is important to get the same wavelength information for each point of the bruised area. If the wavelength drift is too large the FPI mirror gap has to be scanned in the vicinity of the desired wavelength to reconstruct the spectral response from a set of images. Even though the post-processing is easy for paraxial imaging, measuring more wavelengths results in a longer acquisition time and therefore not desirable. The transmittance wavelength shift is 40 nm between marginal and chief ray, which is far more than the tolerable 6 nm spectral resolution (see Eq. (1.11)). Reconstructing the spectral image during post-processing therefore requires a hyperspectral image instead of just nine wavelengths and the measurement takes $\times 3.7$ longer.

It is greatly preferred to use cross-polarisation of the light source and the camera in spectral skin imaging to suppress light that is reflected directly from the surface of the skin without penetrating the bruise. Since the transmission properties of a multilayer coating are different for s- and p-polarisation as described in Section 1.4.2 the difference in field angles changes the transmission properties even more for each object point and the circular symmetry is broken¹⁶. Second the collimated rays originating from an object point pass through a large area of the Fabry-Pérot mirrors and therefore suffer from all mirror imperfections. Large-range mirror inhomogeneities like a lack of parallelism or bent mirrors have maximum impact on the spectral resolution.

1.5.2. Telecentric design

The other extreme alternative to the collimated configuration is placing the FPI in the image space of an imaging system that is telecentric on the image side. Telecentric lenses have a constant non-angular field of view. Their magnification does not change in terms of object/image distance. Telecentricity can be achieved on both object and image side of an optical design. For telecentricity on the

¹⁴The FPI is ideal in the sense that the mirrors are assumed to be perfectly smooth and parallel to each other.

¹⁵If the object is sufficiently far away from the camera, the lens system in the front can even be omitted as for the design shown in Section 2.4.

¹⁶Note that it is not possible to choose the polarisation passing through the FPI. While light on the horizontal axis of the FPI might be s-polarised, it will be p-polarised on the vertical axis. On the diagonals and everywhere else in between, it is a superposition of both polarisation states. The transmittance of a single polarisation state results in a single transmittance peak, the superposition of two polarisation states results in a double-peak.

object side however the first lens of the system needs to have at least the size of the object, which makes it very unattractive for handheld applications. On the image-side, it is easy to implement and allows placing the FPI anywhere in between the last lens and the detector. Rays coming from different object positions pass the FPI in different confined areas and therefore the influence of large scale surface is less than in the collimated system. Additionally the rays coming from all object points pass the FPI under close to normal angle of incidence, preventing transmission wavelength shifts over the FOV. The influence of polarisation on the transmittance properties is also minimal for close to normal incidence.

The disadvantage of the telecentric configuration is that the rays from a given object point are not parallel when passing through the FPI. The angular difference between normal incidence and the angle of incidence of the marginal rays broadens the transmission wavelength in all image points equally. The impacts on the design of a spectral camera and the derivation of a design criterion will be discussed in Chapter 2 using a surveillance camera example.

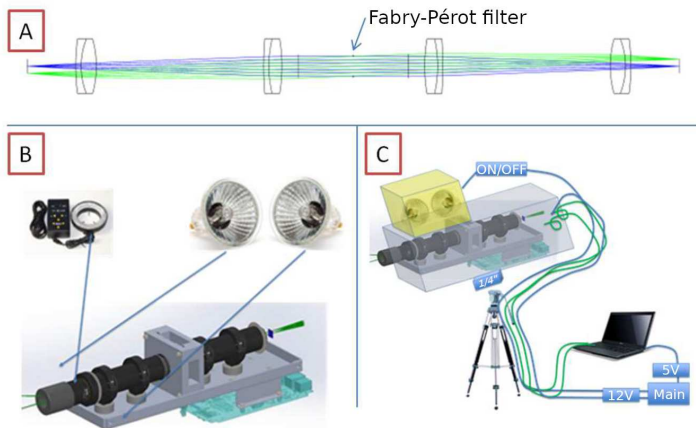


Figure 1.27.: Final Spectr@phone camera. A Optical system of the final demonstrator. B Camera components. C Full camera including housing, main controller board, and laptop

The best solution for the Spectr@phone camera was therefore decided to be the telecentric design. However due to time and money considerations the final spectral camera was built using the collimated design. Off-the-shelf components are used to create a working but not necessarily very compact camera system. The resulting design is displayed in Figure 1.27. The spectral camera meets all spectral and optical requirements as defined during setup of the project (Tab. 1.2). The only disadvantage of the system is that the camera can be barely called handheld but it is at least not larger than the initially used LCTF camera at the AMC.

The spectral transmittance characteristics of the spectral camera imaging a uniformly illuminated white target are displayed in Figure 1.28. The losses in the peak intensities can be explained by the effects of large scale surface imperfec-

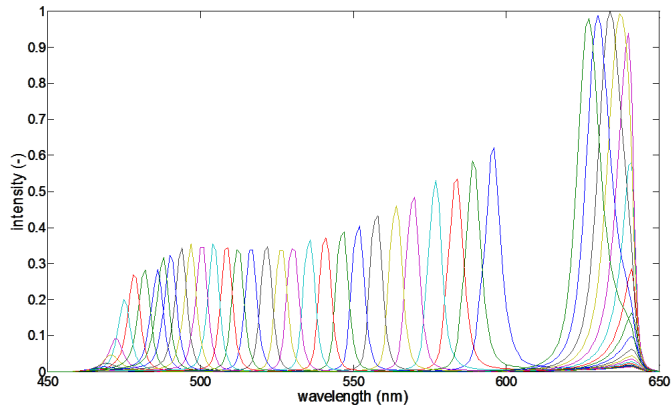


Figure 1.28.: Transmittance measurement of the final camera system axis for various mirror configurations. The colours are reused for multiple mirror gap sizes/transmission wavelengths

tions, misalignment, and polarisation broadening in the collimated configuration. A telecentric system would suffer significantly less from mirror bending and lack of parallelism of the mirrors and therefore produce more confined and higher transmittance peaks for lower-wavelength transmissions.

The newly developed camera has been tested successfully on bruises at the AMC in Amsterdam and will be further developed and adjusted to their needs in the future. The Fabry-Pérot module is made available commercially and can be bought from Anteryon [105].

2. Wide-angle spectral imaging using a Fabry-Pérot interferometer

Spectral imaging of bruises requires a fast spectral imaging system with a low spectral and spatial resolution compared to e.g. agricultural or microscopy applications. Nonetheless the described Fabry-Pérot interferometer (FPI) can be applied in much more demanding camera systems. To investigate how to design an optical system using an FPI we started a project with Prof. Irina Livshits from the Research Laboratory Computer-Aided Design Optical-Information and Energy Saving Systems at ITMO University in Saint Petersburg, Russia. The idea of the cooperation was to investigate the performance of the FPI in one of her high performance surveillance camera systems. The results of this collaboration as summarised in this chapter are published in the Journal of the European Optical Society - Rapid Publications [106].

This chapter shows that wide-angle spectral imaging can be achieved with compact and cost-effective devices using Fabry-Pérot interferometers. Designs with a full field of view of 90° , in which the Fabry-Pérot interferometer is mounted either in front of an imaging lens system or behind a telecentric lens system are presented and analysed. We show the dependency of the spectral resolution on the numerical aperture of the lens system and demonstrate its value as a design criterion.

2.1. Importance of spectral imaging in surveillance cameras

As already described using the example of bruise imaging in Section 1.1, with spectral imaging, spectral information is obtained in every image point, thereby gaining more information that is useful in diverse applications. It is nowadays widely used and many new spectral imaging techniques were developed over the last few years [17, 107]. While most research focussed on the development of spectral imaging components or on the applications of spectral imaging, there is still potential to improve the lens design of complete spectral imaging systems, especially for applications that require a large field of view (FOV). An increased FOV spectral imaging system is presented by Xu et al. [108], who designed an acousto-optical tunable filter system for a full FOV of more than 30° . At the same time more and more applications are found, which can benefit from spectral imaging with a large FOV, for example in security and surveillance applications such as face recognition techniques, which require information in the visible and near-infrared range [109, 110]. Tracing a moving object or person based on spectral imaging [111] was studied and the effects of shadow [112] and darkness [113] and

their correction were studied. The ExoMars 2020 rover for example uses several wide-angle spectral cameras to create 3D spectral images [114].

The usage of a tunable Fabry-Pérot interferometer is becoming increasingly popular [33] due to its high light efficiency for a given spectral resolution [38]. But so far it has mainly been used in remote sensing applications that require high optical resolution, like the Aalto-1 satellite [115] or in drone systems for agricultural observation [116,117] and in telescopes like the vacuum tower telescope on Tenerife [29]. Many new applications do not require such high resolutions, but it is in general desirable to develop small and cost-effective systems. Following the trend of mass-producing small cameras, tunable FPIs can be produced with the same machines and techniques and be offered low-priced and in large quantities.

2.2. Design criterion

Taking account of the requirements for the FPI in the design of the optical system of which the FPI will be part, can improve the performance of the overall spectral imaging system. A design criterion can be derived based on the geometric model of a FPI as obtained in Section 1.4.1.

The transmittance of an ideal Fabry-Pérot interferometer (i.e. an FPI illuminated by plane waves with perfectly flat and parallel mirrors and without absorption losses) is given by the Airy function (1.15)

$$\mathcal{A}(\phi, R) = \frac{1}{1 + F(R) \sin^2 \frac{\phi}{2}}, \quad (2.1)$$

where the phase ϕ depends on the wavelength λ , the angle of incidence θ of the incoming rays, the mirror separation d and the refractive index n of the medium in between the mirrors as (see Eq. (1.11)) [118]:

$$\phi = \frac{2\pi}{\lambda} 2nd \cos \theta, \quad (2.2)$$

and $F = 4R/(1 - R)^2$ is the coefficient of finesse (1.16), which depends on the reflectance R of the used mirrors. Maxima are obtained for $\phi = 2\pi m$ for all orders $m \in \mathbb{Z}$. The transmittance function \mathcal{T} , which takes account of the absorptions of a part of the light by the mirrors can be written as (see Eq. (1.17)) [99]

$$\mathcal{T}(\phi, R, A) = \left(1 - \frac{A}{1 - R}\right)^2 \mathcal{A}(\phi, R), \quad (2.3)$$

where A is the absorptance of the mirrors. In the ideal limit of 100% reflecting mirrors, i.e. $R = 1$, the transmittance becomes a Dirac comb denoted by the Cyrillic letter Sha: $\mathbb{III}(\phi/2\pi) = \sum_{n=-\infty}^{\infty} \delta(\phi/(2\pi) - n)$.

For high finesse FPIs in practical instruments, the transmittance is not a Dirac comb, but shows finite order intensities, which are broadened by convolution with

a Lorentzian profile (Cauchy distribution)

$$L(x; x_0, \gamma) = \frac{1}{\pi\gamma \left[1 + \left(\frac{x-x_0}{\gamma} \right)^2 \right]}, \quad (2.4)$$

with the location parameter x_0 and the half width at half maximum γ . In this case Equation (2.3) can be approximated by (see Eq. (1.22)) [98]

$$\mathcal{T}(\phi) = \left(\text{III} \left(\frac{\phi}{2\pi} \right) * 2\pi L(\phi; 0, -\ln(R)) \right) \left(1 - \frac{A}{1-R} \right)^2. \quad (2.5)$$

With multilayer mirrors using the Bragg effect nearly absorption-free FPIs can be made. To calculate the reflectance and transmittance of these mirrors and the air space between them, the standard matrix formalism based on the electromagnetic boundary conditions [102] as summarised in Section 1.4.2 can be employed. Alternatively a model by Gawhary et al. [103] that adds up all internal reflections of the coating can be used, too.

We will investigate two special cases of a spectral imaging device with objects at infinity that contain a Fabry-Pérot interferometer. The first case is a *collimated configuration*, where the FPI is mounted in front of the lens system at a position of collimated incidence and the second case is a *telecentric configuration*, where the FPI is mounted behind the lens system that is telecentric on the image side. Equation (2.2) is used in both cases to evaluate the situation for plane waves arriving from the object, i.e. the object is at infinity.

For collimated incidence the transmittance peak wavelengths depend on the incidence angle and the gap size. The wavefronts coming from an object point are planes at the FPI. For plane waves we call the full width at half maximum of a transmittance peak produced by the FPI the intrinsic full width at half maximum $FWHM_i$. In the following we distinguish between the *intrinsic plane-wave $FWHM_i$* , which is fully described by the Equations (2.1)-(2.5) and the *simulated spherical-wave $FWHM_s$* , which will be evaluated numerically in the telecentric case.

For the telecentric configuration, the rays coming from a single object point are not parallel at the FPI, i.e. for every object point we observe (for a well corrected lens system) a spherical wavefront at the FPI. An estimation of the angular behaviour can be made by considering the plane waves travelling along the directions of the marginal and the chief rays. The difference in the angle of incidence at the FPI of the chief ray $\theta_{\text{chief}} \approx 0$ and the marginal rays θ_{marg} broadens the intrinsic transmittance peak of a given order and leads to a decrease in transmittance. To study the design limitation resulting from this effect, we compare the transmittance peak wavelength λ_0 for incidence parallel to the optical axis and the transmittance peak wavelength $\lambda_1 = \lambda_0 - \delta\lambda$ for marginal incidence. Like for spectral imaging of bruises, we focus on only one FPI order. A rough estimate of the wavelength interval $\delta\lambda$, within which light can be maximally transmitted, can be derived from Equation (2.2) by requiring that the phases for λ_0 and λ_1 are

equal

$$\frac{2\pi}{\lambda_0} 2nd = \frac{2\pi}{\lambda_0 - \delta\lambda} 2nd \cos \theta_{\text{marg}}, \quad (2.6)$$

which leads to

$$\delta\lambda = (1 - \cos \theta_{\text{marg}}) \lambda_0. \quad (2.7)$$

The wavelength interval can be rewritten in terms of the numerical aperture on the image side $\text{NA}_i = n \sin(\theta_{\text{marg}})$ of the corresponding optics:

$$\delta\lambda = \left(1 - \sqrt{1 - \left(\frac{\text{NA}_i}{n} \right)^2} \right) \lambda_0. \quad (2.8)$$

In air ($n = 1$) this reduces to a simple design criterion

$$\delta\lambda = \left(1 - \sqrt{1 - \text{NA}_i^2} \right) \lambda_0. \quad (2.9)$$

Because according to Equation (2.7), different peak wavelengths are associated with the angles between 0° and θ_{marg} , the FPI transmission peaks must be broad enough in order to transmit all these angles and to avoid a significant decrease in transmittance. This design criterion based on Equation (2.7) will be used in the analysis of the model system shown below. As will be shown in Section 2.4, except when the NA is very small, the FWHM_s for spherical waves is proportional to $\delta\lambda$.

2.3. The collimated and the telecentric design

The used lens model is a modified version of a wide-angle pinhole lens with a full FOV of 90° designed by Prof. Irina Livshits [119]. The parameters of this and the following lens designs can be found in Appendix A. The starting system by her is displayed in Figure 2.1. The system is smaller than 15 mm in length and the pinhole has a diameter of 1 mm. This makes the surveillance camera basically invisible to the human eye. The model is analysed with CODE V¹⁷. With a FPI mounted at two different positions, the two designs were reoptimised to correct the aberrations introduced by the FPI using the default CODE V merit function, which is optimising for transverse ray aberrations, i.e. the RMS spot size. The design is optimised for three wavelengths 450 nm, 548 nm, and 700 nm and three object half field angles 0° , 31.8° , and 45° . While the collimated configuration is just optimised for the RMS spot size, the telecentric configuration is also optimised for the angle of incidence of the chief rays for each field angle at the FPI $\theta_{\text{chief}} \rightarrow 0$.

The Fabry-Pérot interferometer is modelled as two plane-parallel glass plates having each 0.5 mm in thickness. Unlike in the actual FPI the two glass plates are

¹⁷More details about the analysis with CODE V can be found in Appendix A.

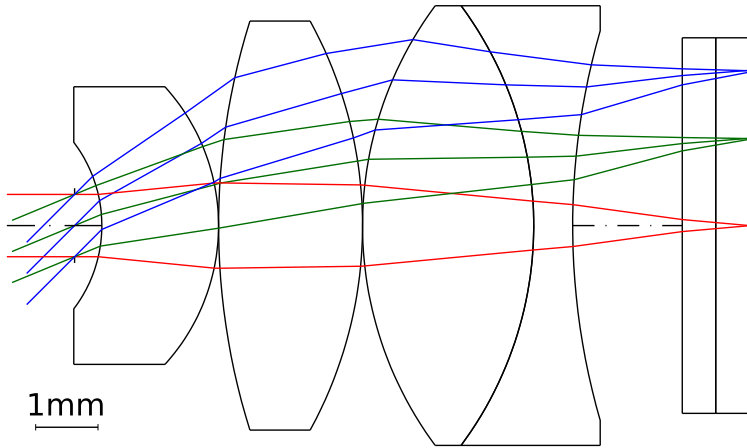


Figure 2.1.: Starting configuration of a spectral imaging system with FOV of 90° with a Fabry-Pérot interferometer behind the lens system designed by Prof. Irina Livshits.

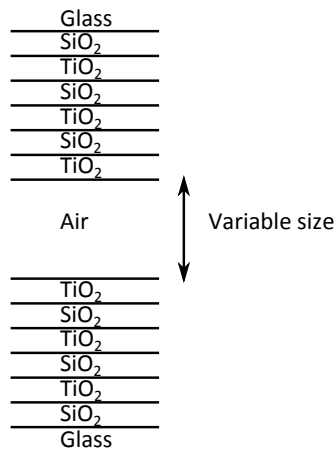


Figure 2.2.: The coating of the FPI is a quarter wavelength optical thickness stack of $(\text{SiO}_2\text{TiO}_2)_3$ with a variable air layer. The used glass is Schott N-BK 7 [120]. The reference wavelength is 548 nm. The refractive indices are: $n_{\text{SiO}_2} = 1.4599$, $n_{\text{TiO}_2} = 2.53598$, $n_{\text{Air}} = 1.00027784$, $n_{\text{NBK7}} = 1.51680$.

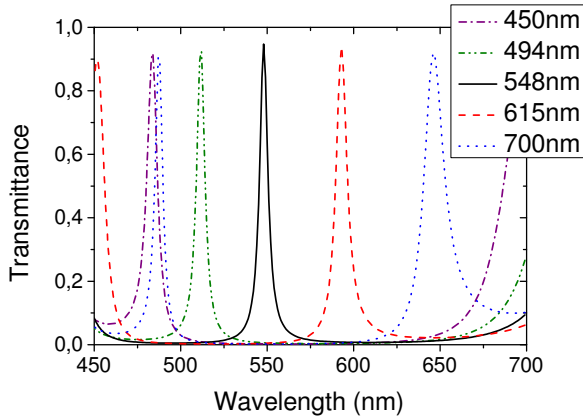


Figure 2.3.: The modelled FPI transmittance is shown as a function of the wavelength for different air gaps and for the case of normal incidence.

modelled in direct contact with each other. Since the thickness of the mirror gap is negligible compared to the thickness of the glass plates, the imaging quality is not impacted by this simplification. The mirror coatings and the air gap are modelled as a single coating in between the glass plates (Fig. 2.2). The transmittance of the FPI can be tuned by varying the thickness of the air layer in the coating model (Fig. 2.3). In CODE V all calculations for the transmission analysis are made relative to unit energy across the entrance pupil [121].

The dimensions of the Fabry-Pérot interferometer (thickness of the FPI mirrors and FPI aperture) are taken from the first FPI demonstrator by Anteryon and similar to those of commercially available FPIs [33, 122, 123]. The thickness of the Fabry-Pérot mirrors was increased during the development of the final FPI to minimize the effects of bending during the mirror movement. For the available FPIs, aperture diameters are available up to 20 mm and the air gap can be tuned with sub-nanometre accuracy in just a few milliseconds. To simulate such an FPI, we choose the coating of the mirrors to be a quarter wavelength optical thickness stack, at reference wavelength 548 nm, of a high and a low refractive index material, made of well-understood FPI coating layers $(\text{SiO}_2\text{TiO}_2)_3$ [124]. The system is reoptimised and evaluated both using the FPI at a position of collimated (Fig. 2.4) and telecentric (Fig. 2.5) incidence.

2.4. Comparison of the spectral performance

Figure 2.6 shows the image quality of the two designs simulated with CODE V. Note that, despite of the large field, the small size and the simplicity of the design, the imaging quality of the system is sufficient for applications such as e.g. surveillance¹⁸. For the CODE V image simulation the input file must be a RGB bitmap,

¹⁸The primary aberrations characterising the designs are listed in Appendix A

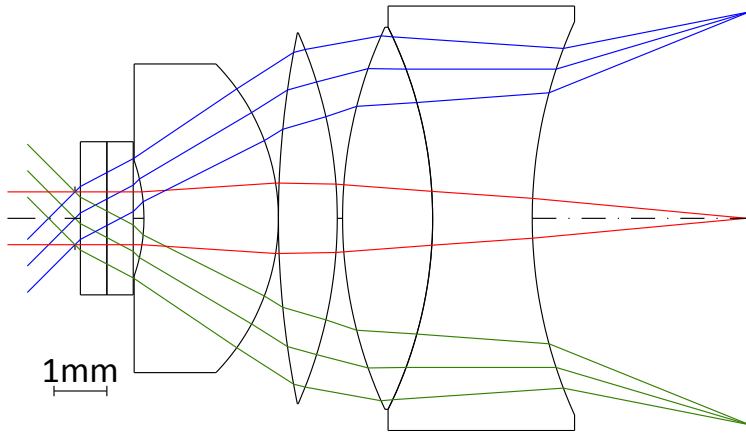


Figure 2.4.: Wide-angle security lens design with a FOV of 90° with and a FPI in collimated configuration. The effective focal length is 5.43 mm and the numerical aperture on the image side is $NA_i = 0.0927$. In comparison to the initial design in Fig. 2.1, the FPI was moved directly behind the aperture and the system reoptimised for a minimal RMS spot size.

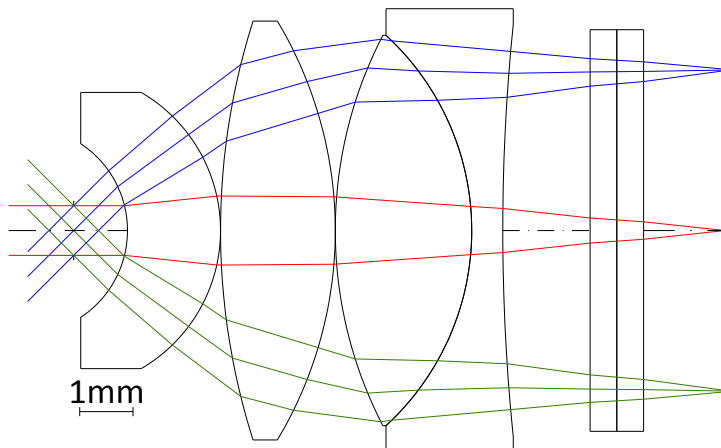


Figure 2.5.: Wide-angle security lens design a with FOV of 90° with and a FPI in telecentric configuration. The effective focal length is 4.33 mm and the numerical aperture on the image side is $NA_i = 0.108$. In comparison to the initial design in Fig. 2.1, the system was reoptimised for telecentricity on the image side and a minimal RMS spot size.

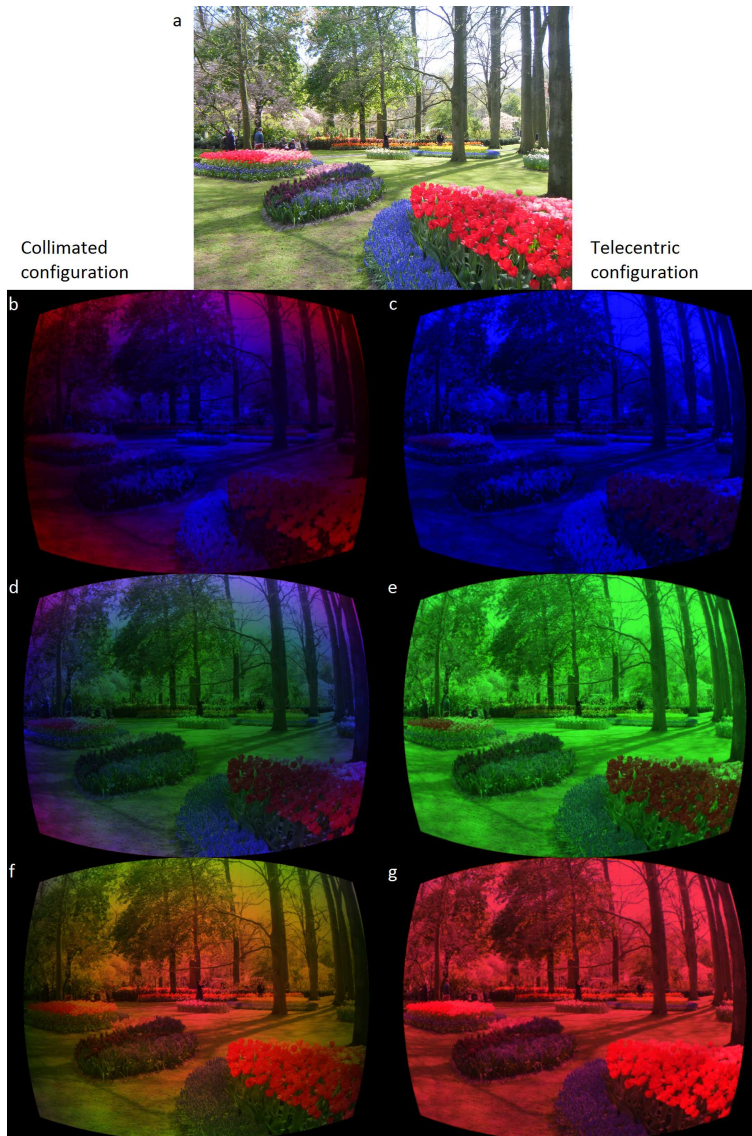


Figure 2.6.: CODE V image simulation that shows the spectral behaviour of the collimated (left) and the telecentric configuration (right). CODE V cannot simulate more than three colour channels with its image simulation, so the object has to be a RGB file and we can only extract information for 3 wavelengths. The images b & c show the transmittance image for a FPI air gap of $d = 190$ nm, d & e for $d = 274$ nm and f & g for $d = 360$ nm. The image of the flower fields at Keukenhof was taken by Luca Cisotto.

so we can extract only three colour channels from the image. The three colour channels of the RGB image can be either assigned to three discrete wavelengths or a weighted set of wavelengths in CODE V¹⁹. Despite of the spectral limitation of using only three input channels the simulation provides useful information on the spectral behaviour of the two camera models. The distortion of the images is typical for wide-angle camera systems and can be corrected by software during post-processing [125]. The different spectral behaviour of the two designs can be best explained by analysing the field angle dependency of the spectral transmittance.

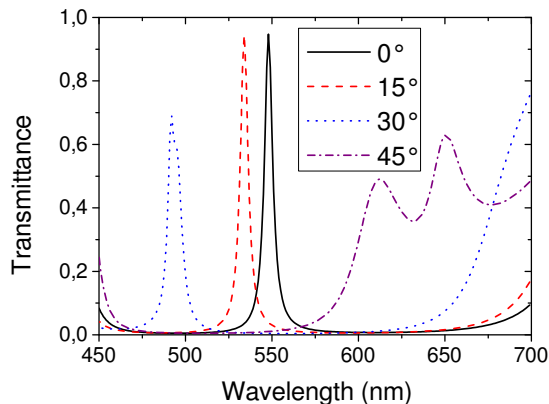


Figure 2.7.: Transmittance spectra of the collimated configuration (Fig. 2.4) for different half field angles using unpolarised light. The angle of incidence at the FPI is identical to the half field angle.

For the collimated design, note that the dominant colours in the centre and at maximal field are different, in accordance with the transmittance²⁰ given in Fig. 2.7. The Airy function (2.1) describes the small angle behaviour, visible as a wavelength shift of the peak for 15° with respect to 0°, without changing the shape of the peak. For large angles, the reflectance of the mirror coatings becomes polarisation dependent and must be described by matrix-based calculations of the thin-film transmittance [102]. For the mirror coating that we use, the transmittance decreases significantly for field angles larger than 20°. The transmittance peak becomes a superposition of the transmittance peaks of s- and p-polarised light, which makes the retrieval of the spectral information more complex. The measured intensity in off-axis image points cannot be assigned to a single wavelength but has to be deconvolved with the exact (double-)peak profile of the FPI.

The field-dependent transmittance of the telecentric design (Fig. 2.5) is shown in

¹⁹In Fig. 2.6, the red channel has been assigned to 450–460 nm and 570–700 nm, the green channel to 460–630 nm and the blue channel to 450–520 nm, mimicking the spectral sensitivity of the human eye and the camera with individual weights per wavelength interval of 10 nm.

²⁰The technique to produce such a plot using CODE V as well as a more detailed plot featuring more field angles can be found in Appendix A.

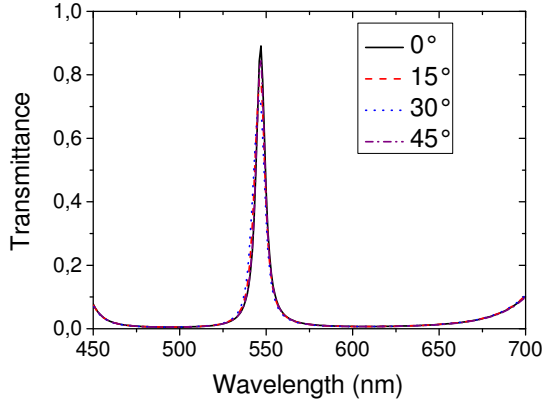


Figure 2.8.: Transmittance spectra of the telecentric configuration (Fig. 2.5) for different half field angles. The angle of incidence at the FPI varies over the full numerical aperture on the image side $NA_i = 0.108$ and is independent of the half field angle.

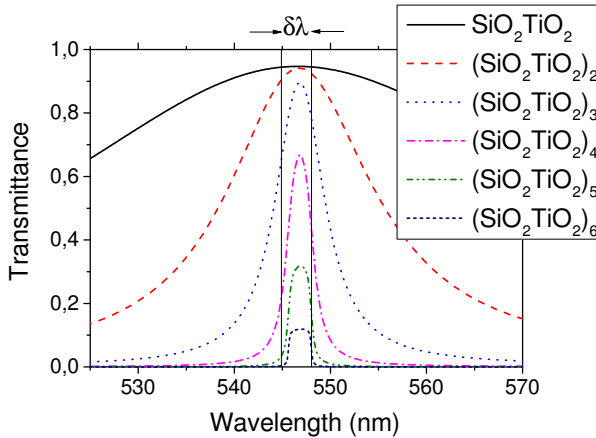


Figure 2.9.: Transmittance as function of wavelength of the telecentric configuration at 0° half field angle for different numbers of pairs of (SiO_2TiO_2) as coatings. The wavelength interval $\delta\lambda$ is indicated in the graph, with the first vertical line being the wavelength λ_1 of maximum transmission for the marginal rays and the second vertical line being the wavelength λ_0 at which the chief ray has maximum transmission. It is required for a properly designed system, that the spectral linewidth of the FPI is larger than the wavelength interval $\delta\lambda$ (see Eq. (2.9)).

Figure 2.8. The transmittance²¹ and the simulated spectral resolution (FWHM_s) remain essentially the same over the entire FOV. Therefore in Figure 2.6c,e,g we see only a single colour (i.e. wavelength peak) for a given value of the FPI air gap. For both collimated and telecentric incidence, changing the coating is mainly influencing the FWHM_s of the transmittance peaks. By increasing the number of coating layers (Fig. 2.9), the mirror reflectance increases and the resulting FWHM_s decreases. However in the telecentric configuration, when the peaks become too narrow to transmit all angles according to Equation (2.7), the transmittance starts to decrease significantly. The transmittance lines for chief and marginal rays become so narrow that they stop overlapping and start interfering destructively. For $\text{NA}_i = 0.108$ as used in the telecentric system (Fig. 2.5) and $\lambda = 548 \text{ nm}$, $\delta\lambda$ is 3.2 nm . If the FWHM of the transmittance peaks is reduced to $\leq \delta\lambda$ the peak intensity decreases. This is in good agreement with the CODE V transmission analysis for different coatings that is displayed in Figure 2.9.

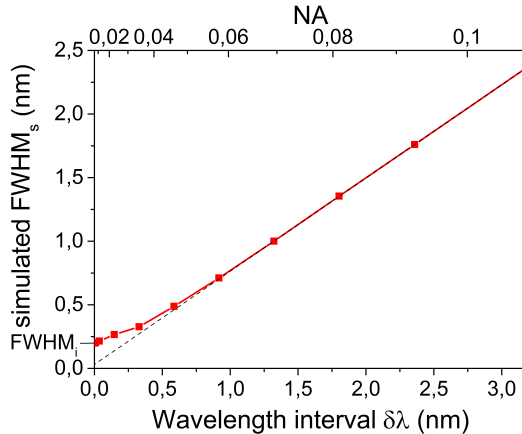


Figure 2.10.: Simulated FWHM_s of transmittance peaks in the telecentric configuration using a FPI with a pair of $(\text{SiO}_2/\text{TiO}_2)_6$ coatings for different numerical apertures. The first point for $\text{NA}_i = 0$ is the intrinsic FWHM_i . For larger numerical apertures the simulated FWHM_s of the peaks is proportional to the wavelength interval $\delta\lambda$ as indicated by the dotted asymptote.

By changing the numerical aperture the dependency of the FWHM_s on the numerical aperture can be observed directly. The results are shown in Figure 2.10. For low numerical apertures, i.e. small wavelength intervals $\delta\lambda$ the simulated FWHM_s barely differs from the intrinsic FWHM_i and is almost completely determined by the coating, while for larger numerical apertures the FWHM_s of the peak becomes proportional to the calculated wavelength interval $\delta\lambda$ as described in . This proportionality comes from the fact that when NA_i increases, the FWHM_s that is required to transmit larger angles also increases. Due to this proportion-

²¹A plot featuring more field angles can be found in Appendix A.

ality Equation 2.9 can be used as a criterion to choose a coating or design for a certain spectral resolution as well as to predict the FWHM_s of a system with a given FPI when the numerical aperture is changed. We can distinguish two cases. For small values of the NA_i , a higher FPI finesse yields a higher spectral resolution without influencing the peak transmittance. For large NA_i , a higher FPI finesse does not influence the FWHM_s but the transmittance decreases. This also implies a reduction of the spectral resolution.

The comparison of the two designs shows their advantages and disadvantages. For the collimated design, the spectral resolution is not limited by the NA_i of the camera design, but digital imaging processing is required. If a hyperspectral image is desired (i.e. many wavelengths are required), the small-angle dependency of the peak transmittance can be corrected by computationally associating all field angles to their corresponding wavelengths. Multispectral imaging, i.e. the case when only a few wavelengths must be determined, also requires a full wavelength scan to obtain the necessary information over the full field of view and is therefore as time-consuming as hyperspectral imaging. For large field angles the transmittance peaks are formed by superposition of s- and p-polarised light. Due to the polarisation dependency of the mirror reflectance the peaks are broadened, deformed and even split up into two peaks. The polarisation-deformed transmittance for large field angles can only be used if the measured data is deconvolved afterwards on the computer.

In the telecentric configuration, the spectrum transmitted by the FPI is almost the same for all field angles and independent of polarisation over the full field of view. For multispectral imaging no continuous wavelength scan is required, because full FOV information for individual wavelengths can be collected separately. As follows from Equation 2.9, the width in terms of wavelength of the transmittance peaks in the telecentric configuration is limited by the numerical aperture on the image side of the imaging optics. A certain required spectral resolution limits the NA_i and therefore the amount of light that can be collected in a given time. Unless high spectral resolution is required, the telecentric design is preferable because of its simplicity. For many applications e.g. for security purposes the spectral resolution that can be obtained with the telecentric design should be sufficient.

Tighter manufacturing tolerances of the mirrors in collimated configurations also motivated e.g. Kentischer et al. [29] to use a FPI in a telecentric configuration. They describe how misalignment and large-scale variations²² of the FPI mirror shape cause only a small wavelength shift in telecentric designs, while the resolution drops significantly in the collimated configuration. The less restrictive tolerances on the manufacturing of the mirrors and the alignment of the system makes the telecentric configuration the preferred system for cost-effective and compact multispectral imaging.

²²Large-scale variations are deviations from a perfectly flat mirror that occur on a macroscopic scale across the surface (e.g. bending). The roughness of a mirror is an example for a small-scale variation.

2.5. Concluding remarks

A large field of view for a multispectral imaging system can be achieved with a simple and compact design. While the common approach of inserting the FPI in front of the lens system is not able to produce a large field of view, the telecentric design shown in Figure 2.5 can achieve this. As shown in Equation 2.9 and numerically confirmed with CODE V, the spectral resolution can be increased by decreasing the aperture size at the expense of the amount of collected light at the detector. This property can be used as a design criterion for telecentric multispectral imaging systems. Depending on the size of the numerical aperture NA_i , we find two cases. In the first case for a small NA_i , increasing the FPI finesse has the desirable effect of increasing the spectral resolution. In the second case for a large NA_i , increasing the FPI finesse has the negative effect of decreasing the transmittance. Because of the simplicity and the reasonable image quality that can be obtained, except if a very high spectral resolution is required, the telecentric system is preferred in many applications, in particular for surveillance systems.

Next to the findings for large FOV multispectral imaging systems, the development of the Spectr@phone camera has been finished successfully. With the help of the new spectral camera system, medical research can progress, help children in need and give further insights into the ageing of bruises.

Part II.

Electrowetting liquid lenses

3. Focusing light using liquid optics

During the development of the spectral camera, it became clear that it would be difficult to publish more scientific articles based on its manufacturing and design. Both the well-known working principle of a Fabry-Pérot interferometer (FPI) and the business interests of the involved companies hindered publishing more design details and findings. Starting from Florian Bociort's initial idea to use a zoom lens to scan through different angles of incidence on a standard FPI with fixed distances between mirrors, the use of a liquid lens was discussed. Angular scanning of a FPI however has two drawbacks. First only marginal rays change their angle of incidence when changing the focal length of an objective. The on-axis chief ray does not change direction during a zoom-based angular scan therefore, huge parts of the aperture would have to be blocked to achieve a reasonable scanning effect. Second the scanned wavelength range would be small similar to approaches where a dichroic filter is turned [87, 88]. Large angle of incidence polarisation effects of the FPI/filter can limit the performance as well.

With these properties in mind, during the first year of the project I came up with a different method to use a liquid lens for spectral imaging. The idea was to create a grating on a liquid (lens) to scan different wavelengths for spectral imaging. If it is possible to create a standing sine wave on a liquid pool, changing the actuation frequency will tune the grating constant of the liquid surface grating²³. This optical grating could be used to diffract different wavelengths of the incident light into different directions. The standing wave on the surface depends sinusoidal on time and hence, there are two times during one period of the oscillation, when the surface is flat and there is no grating present on the surface of the liquid. Although the deflection of the surface wave changes with time, the grating constant does not change during the oscillation. In consequence, we would expect the intensity to shift from the 0th order to higher diffraction orders during times when the aspect ratio of the grating increases. The diffraction angle would be time-independent for any wavelength, so a detector placed at the correct position can easily be used to determine the wavelength composition of the spectral image. The only requirement would be a sufficiently long integration time of the detector to ensure that the surface is not flat during the measurement.

Unfortunately, manufacturing a new liquid optics device from scratch has been beyond our capabilities. We therefore decided to buy an existing liquid optics system and study the principle of stimulating liquid surface waves to create useful optical surfaces. The system of choice turned out to be a liquid lens (LL). A liquid lens however is round and is therefore not suited for creating a linear grating, because it favours circular or radial symmetry. These symmetries are however

²³The terms surface and interface will be used interchangeably, because any surface that is not in contact with vacuum is in fact an interface between two media.

useful and interesting for other applications namely beam shaping and aberration correction of imaging systems in which the aberrations are rotationally symmetric.

3.1. Liquid lens techniques

There are four major tunable liquid lens techniques on the market making use of four different fundamental physical principles: pressure, surface tension, crystal structures, and acoustic waves.

3.1.1. Tunable acoustic gradient index of refraction lenses

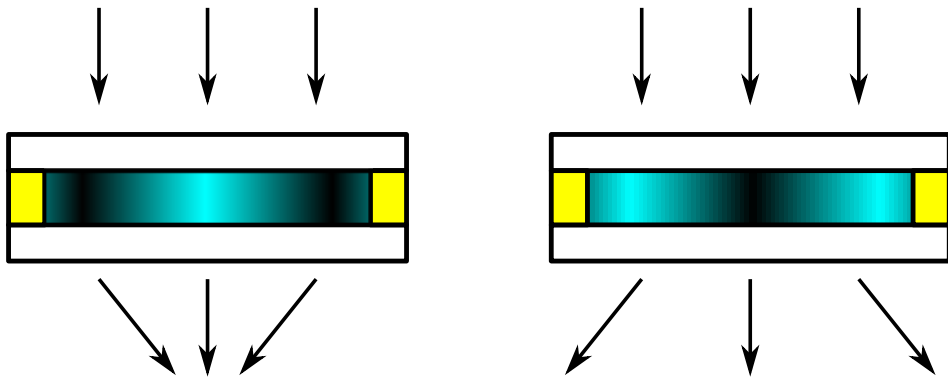


Figure 3.1.: Tunable acoustic gradient index of refraction (TAG) lens. Piezos (yellow) create an acoustic wave that changes the refractive index of the liquid.

The most uncommon and most recent technique is the tunable acoustic gradient index of refraction (TAG) lens also known as an ultrasound lens [126]. TAG lenses use a piezoelectric transducer driven at 70 kHz – 1 MHz to create sound waves in a liquid as shown in Figure 3.1 [127]. Sound waves create a pressure grating that results in a periodic change of the refractive index inside the liquid. Light passing through the liquid lens is delayed depending on the momentary local refractive index of the lens, creating different phase profiles for different driving frequencies. The resulting phase front created by a TAG lens actuated with a single sine frequency has the shape of a Bessel function²⁴ $J_\nu(r)$. The Bessel phase front can for small r be approximated by a parabolic surface $J_0(r) = 1 - r^2/4 + \mathcal{O}(r^4)$. An aperture is used to cut out all light passing through the non-parabolic region to locally create a close to spherical surface²⁵. Just like a liquid surface, the standing wave is not at rest but continuously oscillating. The focal length of the lens is continuously changing therefore, to take a snapshot the camera or

²⁴ J is the Bessel function of first kind, ν is the order of the Bessel function, and r the radial coordinate.

²⁵A spherical surface can also be approximated by a parabola as shown in Section 3.1.3.

light source needs to be triggered and the image needs to be taken very quickly. The extreme speed is the main strength of the technique allowing 3D volumetric scanning of e.g. biological processes faster than any other technique available but the lateral and axial resolution is rather low due to the reduced numerical aperture (NA). TAG lenses as resonant axial scanners have been successfully tested in e.g. confocal microscopy or 2-photon excitation (2PE) microscopy where femtosecond laser pulses provide the necessary power to allow imaging during the extremely short integration time [128–131]. TAG lenses can also be used to create phase profiles in the shape of Bessel functions for e.g. beam shaping [132].

TAG lenses can be purchased from TAG Optics Inc.²⁶ and are a promising technique for high speed applications [133]. The aperture diameter of a TAG lens is in the range of 11 mm while the whole lens has a length and diameter of around 35 mm and requires driving voltages of up to 50 V. The lenses can be used for wavelengths from 355 nm to 1064 nm, with a NA of up to 0.02 depending on the focal length. The predominant aberration is astigmatism followed by spherical aberration and coma.

3.1.2. Liquid crystal lenses

Liquid crystal (LC) lenses were first described by Susumu Sato in 1979 [134]. They consist of a rigid transparent container containing liquid crystals. LCs flow like liquids but their molecules can be arranged in a crystal-like structure. They are typically polar organic rod-shaped molecules that show different refractive indices along and perpendicular to their axis. One way to control the orientation of LCs is placing them in an electric field. In liquid-crystal displays (LCD) this effect is used to reorient the molecules in a chiral phase to turn the polarisation of the light between two cross-polarisers. In LC lenses typically ring-patterned indium tin oxide (ITO) electrodes are used to turn the molecules as a function of the radius. The radially changing refractive index forms the lens [135–138].

The technique has been applied in many fields of imaging, e.g. for zoom objectives [139], for autofocus lenses [140], augmented reality [141] or holographic displays [142]. Like LCD screens LC lenses can be used for the whole visible wavelength range and the switching speed ranges between 1 and 20 kHz [143]. The NA ranges up to 0.01 while the optical power typically stays below 2 m^{-1} .

3.1.3. Membrane liquid lenses

The simplest and oldest technique to create a liquid lens is filling a flexible transparent container with a liquid and pressing on it at some part to increase the pressure and deform the surface at a different part. The first mentioning of a liquid lens known to the author is a patent filed in 1893 by Arnold A. Ingram [144]. There are many more LL patents from the following decades especially in Germany [145, 146] until Robert Graham published the first scientific article in 1940. Two extremely thin hemispherical glass plates are connected with a rubber ring and filled with a transparent liquid. Squeezing the lens changes its focal length [147].

²⁶Part of Mitutoyo

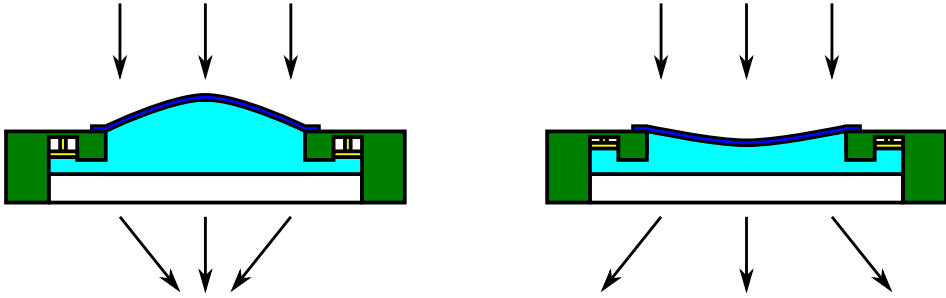


Figure 3.2.: Membrane liquid lens

The original technique of bending glass plates has been reinvented very recently by Dynamic Optics SrI a spin-off from the group of Stefano Bonora [148, 149]. However, nowadays mainly transparent polymer membranes are used to contain the liquid [150]. This is usually done by using a glass container with a membrane on top. Pressure is applied to the liquid at the outer part of the lens by e.g. piezoelectric actuators to change the shape of the membrane in the middle of the lens as shown in Figure 3.2. The surface shape of a membrane liquid lens is by default a paraboloid in the middle of the lens and flat at the outer rim. In the centre, the surface can be approximated by a hemisphere²⁷ $\sqrt{R^2 - r^2} = R - r^2/(2R) + \mathcal{O}(r^4)$. The resulting aberrations can be controlled by using a membrane with a variable thickness [151–154].

The main manufacturer of membrane liquid lenses is Optotune [155], selling lenses with comparatively large apertures of up to 20 mm. Membrane liquid lenses are a popular tool for many applications ranging from augmented reality [156] to machine vision. They have the advantage of large diameters but suffer from aberrations due to gravity if oriented vertically. Membrane lenses can be used from 420–1600 nm and reach a NA of up to 0.02.

3.1.4. Electrowetting liquid lenses

Electrowetting (EW) liquid lenses are based on the manipulation of surface tensions. The earliest occurrence of an EW lens known to the author is a publication by Werner B. Schneider in the German language from 1988 [157, 158]. He refers to it as if it has been already known for a longer time as a "little known method to create a lens". The development of reliable electrowetting liquid lenses started with the work of Bruno Berge and Jerome Peseux in 1997 (patent in French) [159, 160] and Stein Kuiper and Benno H. W. Hendriks in 2004 [161].

A liquid droplet is deformed when placed in an electric field. Depending on the voltage the droplet focusses light at different distances. In a commercially available EW liquid lens the liquid forms an interface with a second liquid enclosed in a transparent container. The exact working principle of a liquid lens is described below in Section 3.2. Liquid lenses create spherical surfaces, which places them

²⁷ R is the radius of curvature of the lens.

ahead of the other techniques in terms of optical quality for imaging systems. There have been approaches to correct for the resulting spherical aberrations by combining their working principle with the principles of the other techniques to create aberration-free imaging systems [162,163]. Unlike mechanical (e.g. MEMS) zoom systems electrowetting lenses are not affected by external vibrations and can be used in various work environments where other small autofocussing systems fail. They are invariant to effects of gravity and provide a large focal range.

Electrowetting liquid lenses are produced by Corning²⁸ and have been sold more than a million times as of 2018 [164]. They have been applied in barcode readers [165], ophthalmology equipment, machine vision and autofocus systems in vibrating environments. They are produced with aperture sizes <4 mm and use a voltage input of up to ± 70 V. The lenses can be used efficiently in the wavelength range from 410-850 nm with a transmission of typically 97% but also in the near IR where the transmission drops to only 70% at 1100 nm.

The choice for a suited liquid lens was made based on two requirements: First surface waves can only be studied if there is a flexible liquid surface in the LL; second the lens had to be cheap since there was limited funding to support this research. A single EW lens costs only 100 € and is therefore chosen to be subject of this research. To understand the surface behaviour of a liquid lens it is necessary to understand the underlying physical mechanism.

3.2. Electrowetting

Electrowetting describes the modification of the wetting properties of a surface in an electric field. Electrocapillarity has been first described in 1875 by Gabriel Lippmann in his PhD thesis (in French) [166,167]. He observed electrowetting at a mercury-electrolyte (H_2SO_4) interface. Over the decades, physicists, electrical engineers and chemists have investigated the topic from various perspectives. An extended overview including a translation of Lippmann's thesis can be found in [167]. We will neglect all gravity influences due to the high surface to volume ratio of small droplets and consider two approaches to derive the central principle of electrowetting.

3.2.1. Wetting

Wetting describes the contact of a liquid with a solid surface. Usually wetting deals with three phases: a solid surface, a liquid drop, and the surrounding air. The wettability is a result of intermolecular forces between all of the involved materials. The molecules in a perfectly non-wetting situation (e.g. water on Teflon) show weak solid-liquid interactions but strong liquid-liquid interactions. A spherical drop is formed. For weak intra-liquid interactions and strong solid-liquid interactions instead perfect wetting is achieved and the drop smears out to a thin sometimes even single molecular layer.

²⁸Formerly: Varioptic, which is kept as a brand name.

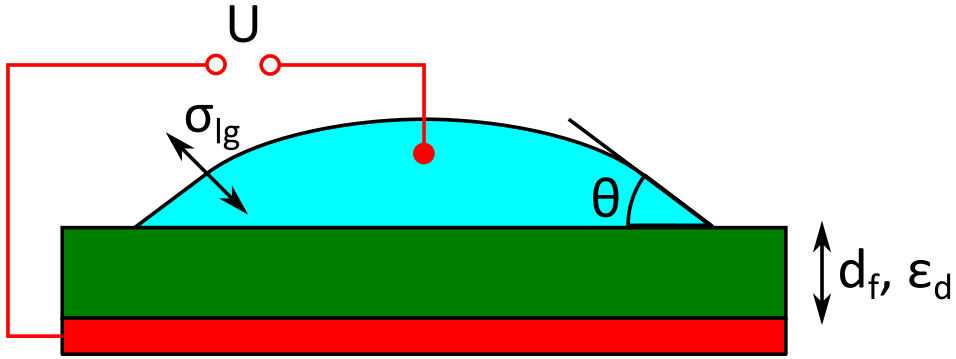


Figure 3.3.: Electrowetting can be best observed in a capacitor setup consisting of three main parts: A conducting planar plate (red) covered with an insulator (green) and the conducting droplet on top (blue). An electrode is used to apply a voltage between the droplet and the conducting plate.

Electrowetting typically deals with partially wetting liquids, which are often chosen to be salt-water droplets of millimetre dimension or smaller. The droplet is lying on a planar insulating surface on top of a metal plate (Fig. 3.3). With an electrode contacting the water a voltage can be applied between the metal plate and the liquid droplet. The surrounding medium is often air or an immiscible oil. On this scale gravity can be neglected compared to surface tension. In the absence of an electric field, the shape of the droplet is determined by the interfacial free energy or surface tension σ . The interfacial free energy F_i of the droplet is given by the sum of contact areas between the three phases²⁹ and volume V conservation

$$F_i = A_{sl}\sigma_{sl} + A_{sg}\sigma_{sg} + A_{lg}\sigma_{lg} - \lambda V, \quad (3.1)$$

where A_{sl} , A_{sg} , and A_{lg} are the areas of the solid-liquid, the solid-gas, and the liquid-gas interface, respectively and σ_{sl} , σ_{sg} , and σ_{lg} are the surface tensions of the solid-liquid, the solid-gas, and the liquid-gas interface, respectively, and λ is a Lagrangian variable present to enforce a constant volume V . λ is equal to the pressure difference Δp over the liquid-gas interface [167]. Minimising the free energy yields two equations:

- Young-Laplace equation:

$$\Delta p = \sigma_{lg} \left(\frac{1}{R_1} + \frac{1}{R_2} \right), \quad (3.2)$$

with R_1 and R_2 being the principal radii of curvature³⁰.

²⁹We denote the solid substrate with s, the liquid phase with l, and the surrounding gas or oil with g.

³⁰The principal radii of curvature are the radii of curvature along two perpendicular meridians originating from the point of interest and in general position-dependent.

- Young's equation:

$$\cos \vartheta_Y = \frac{\sigma_{\text{sg}} - \sigma_{\text{sl}}}{\sigma_{\text{lg}}}, \quad (3.3)$$

with Young's equilibrium³¹ contact angle ϑ_Y being the solid-liquid contact angle on a mesoscopic scale.

If no external forces act on the surface and the surrounding media, the pressure difference between two media is constant along the surface. Then the Young-Laplace equation implies that the sum of curvatures of the droplet is constant everywhere on the liquid surface. For homogeneous surfaces the principal radii of curvature are identical and the droplet is therefore spherical. Young's equation determines the contact angle of a liquid with a surface in the absence of external forces, e.g. an applied electric field.

3.2.2. Electrowetting

The electrowetting on dielectric (EWOD) equation as the central result describing electrowetting can be derived in a few different ways. We present the derivation based on investigating the charge accumulation at the liquid-surface interface layer and on minimising the free energy [167].

Thermodynamic approach

Lippmann's derivation is based on Gibbsian interfacial thermodynamics [166]. Lippmann described electrowetting on metal, we in contrast will derive the electrowetting equation on a dielectric to be able to predict the behaviour of a droplet in a capacitor structure as shown in Figure 3.3. When applying a voltage dU the intermolecular forces change at the liquid-solid interface. Ions in the liquid are pulled to the interface by the electric field causing a change of the effective surface tension

$$d\sigma_{\text{sl}}^{\text{eff}} = -\rho_{\text{sl}}dU, \quad (3.4)$$

where $\rho_{\text{sl}} = c_{\perp}U$ is the surface charge density of the relocated ions with $c_{\perp} = \epsilon_0\epsilon_d/d$ the capacitance per unit area where ϵ_0 is the permittivity of vacuum and ϵ_d is the relative permittivity of the dielectric and d is the thickness of the dielectric. The voltage-dependency of the effective surface tension follows by integration:

$$\sigma_{\text{sl}}^{\text{eff}} = \sigma_{\text{sl}} - \int_0^U \rho_{\text{sl}}dU = \sigma_{\text{sl}} - \frac{\epsilon_0\epsilon_d}{2d}U^2. \quad (3.5)$$

Substituting the result into Young's Equation (3.3) yields the electrowetting on dielectric (EWOD) equation that defines the mesoscopic solid-liquid contact angle ϑ :

$$\cos \vartheta = \cos \vartheta_Y + \frac{\epsilon_0\epsilon_d}{2d\sigma_{\text{lg}}}U^2. \quad (3.6)$$

³¹Young's equilibrium contact angle is the contact angle in absence of external potentials, e.g. an applied electrical field.

The second term is known as the electrowetting number. It measures the strength of the electrostatic energy compared to the surface tension.

Energy minimisation approach

The free energy of a droplet $F = F_i - F_{el}$ consists of two parts: The interfacial energy F_i as given by Equation (3.1) and the energy of the electric field [168]:

$$F_{el} = \frac{1}{2} \int \mathbf{E}(\mathbf{r}) \cdot \mathbf{D}(\mathbf{r}) dV, \quad (3.7)$$

with the electric field $\mathbf{E}(\mathbf{r})$ and the dielectric displacement $\mathbf{D}(\mathbf{r}) = \epsilon_0 \epsilon(\mathbf{r}) \mathbf{E}(\mathbf{r})$ at point \mathbf{r} . The electric field energy can be calculated by simplifying the problem to a plate capacitor between the droplet and the metal plate. The stray fields at the contact line of the droplet can be neglected for larger droplets. Thus, the electric field energy is equal to the energy of a capacitor $F_{el} \approx CU^2/2 = \epsilon_0 \epsilon_d A_{sl} U^2 / (2d)$. The free energy for EWOD then becomes:

$$F = A_{sl} \left(\sigma_{sl} - \frac{\epsilon_0 \epsilon_d U^2}{2d} \right) + A_{sg} \sigma_{sg} + A_{lg} \sigma_{lg} - \lambda V. \quad (3.8)$$

The free energy of a droplet in presence of an electric field has the same structure as the free energy in absence of an electric field (see Eq. (3.1)). By comparing the coefficients we discover that Young's Equation (3.3) obtained by minimising the free energy turns into the EWOD Equation (3.6).

On a microscopic scale the contact angle deviates from the prediction of the EWOD equation [169]. There is also an electromechanical approach to derive the electrowetting equation [170, 171].

3.3. Electrowetting liquid lens

The electrowetting effect can be used to make a liquid lens. The capacitor structure in its presented form (Fig. 3.3) cannot be used for imaging because it is typically not transparent. Since the contact angle is only determined at the contact line, it is not necessary to use a large metal electrode that covers the whole aperture area. The electrode can be reduced to a ring electrode and completely be integrated into the outer walls of the liquid lens.

To ensure that the lens is working in all environments it is enclosed in a cylindrical container with two glass windows. The conductive droplet is typically immersed in a non-conductive oil that does not mix with it and works as an additional thin insulating layer that prevents breakthroughs and the thereby resulting electrolysis of the droplet. The composition of the oil is typically chosen such that its density is equal to the density of the conducting droplet. Density matching allows using the lens in all orientations without a gravity-related change of the optical surface and prevents effects on the liquid surface caused by shocks or vibrations of the imaging system. A typical choice of the oil is a mixture of 2-chloronaphthalene and dodecane with a weight ratio of 8:2. A typical choice for the conducting

droplet is an 47 wt% aqueous solution of glycerol and 1 wt% of sodium lauryl sulphate [172]. A selection of material properties can be found in Table 3.1. The mixtures both have a density of 1.107 g/cm^3 but different refractive indices of $n_l = 1.38$ and $n_o = 1.49$. The indices l and o stand for liquid and oil, respectively.

Material	Density (g/cm^3)	Viscosity (mPa s)	Refractive index at 589nm	Surface tension (mN/m)
Water	1	0.89	1.333	72.8
Dodecane	0.7495	1.383	1.421	25
2-chloronaphthalene	1.2656		1.60787	
Glycerol	1.25	934	1.474	64.8
Glycerol (47 wt%)	1.107	5		65
Sodium lauryl sulphate	1.1			

Table 3.1.: Material properties of typical substances in a liquid lens [172–175].

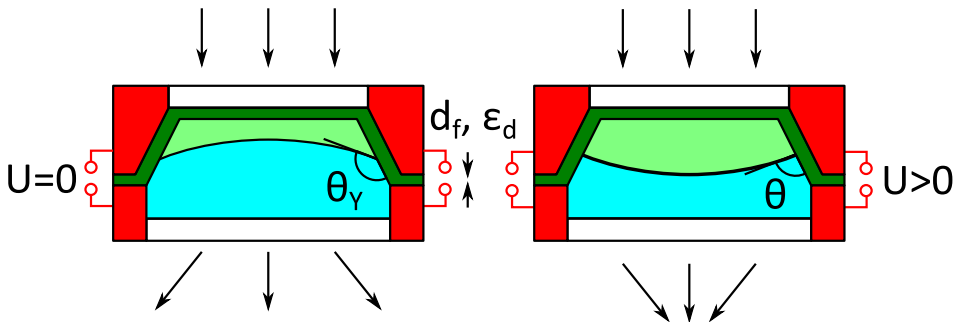


Figure 3.4.: Working principle of a liquid lens. Applying a voltage changes the contact angle of the aqueous droplet (cyan), the remaining space is filled with an immiscible oil (light green). A transparent insulating layer (dark green) separates both parts of the metallic and conducting package that serve as electrodes (red). The glass windows are shown in white.

Figure 3.4 shows the profile of a liquid lens. The bottom electrode is in contact with the conducting droplet, while the top electrode is typically coated with a hydrophobic and insulating layer of parylene-C and/or Teflon AF 1600 and serves as the second capacitor plate. The walls of the liquid lens are tilted in a 45° angle to ensure that the drop stays centred in the LL.

The optical power P can be expressed in the applied voltage U using the EWOD

equation [161]:

$$R_{\text{curv}} = \frac{R}{\cos \vartheta} = \frac{R}{\cos \vartheta_Y + \frac{\epsilon_0 \epsilon_d U^2}{2d\sigma_{\text{lg}}}} \quad (3.9)$$

$$P = \frac{n_o - n_l}{R_{\text{curv}}} = P_0 + \frac{\epsilon_0 \epsilon_d (n_o - n_l)}{2\sigma_{\text{lo}} d R} U^2, \quad (3.10)$$

with R_{curv} being the radius of curvature of the liquid-oil interface, R the radius of the liquid lens cylinder, and $P_0 = (n_o - n_l) \cos \vartheta_Y / R$ the optical power³² for $U = 0$. Note that the EWOD Equation (3.6) and Equation (3.10) contain a simplification that often results in a threshold voltage. For some materials the equilibrium contact angle predicted by Young's Equation (3.3) is larger than 180° , i.e. $|\sigma_{\text{so}} - \sigma_{\text{sl}}| / \sigma_{\text{lo}} > 1 \neq \cos \vartheta_Y$. Thus, low voltages compensate for the large predicted contact angle and the surface only starts to change if the predicted contact angle drops below 180° [176]. Figure 3.5 shows the focussing behaviour of the purchased liquid lens as function of the applied voltage.

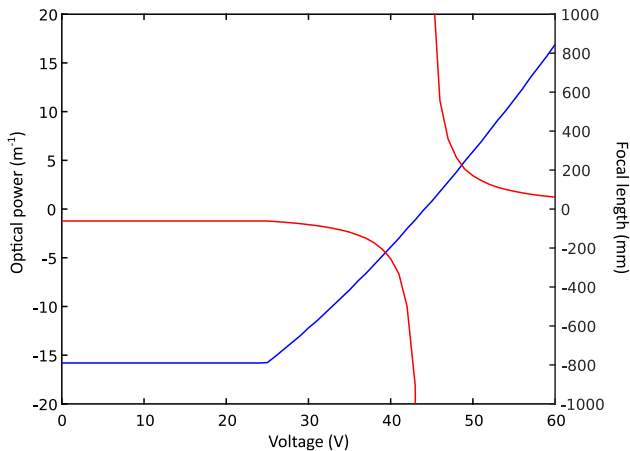


Figure 3.5.: Voltage dependency of the optical power (blue) and the effective focal length (red) for a Varioptic Arctic 39N0 liquid lens [177].

There are three ways to operate a liquid lens. AC operation, DC operation, and quasi-DC operation³³. All modes have their individual advantages and disadvantages. We focus on AC operation, i.e. all voltages are modulated with a 1136 Hz square wave. AC operation prevents charging and polarisation of the non-conducting oil and produces highly reproducible surface shapes with a negligible hysteresis. The main disadvantages are a higher electric fatigue of the insulating layer and higher power consumptions.

³²We denote the oil with o which replaces the index g for gas in a liquid lens.

³³DC with an occasional switch in polarity every 1 – 10 s.

3.3.1. Arctic 39N0



Figure 3.6.: Two Varioptic Arctic39N0 liquid lenses. The two parts on the left are the bottom and the top part of a lens showing the inside. The top half of the lens (middle) is coated entirely with a thin hydrophobic and insulating coating. The bottom half of the lens (left) contains a plastic ring that both seals the lens when pressed together with the bottom part and separates the top from the bottom electrodes similar to a button cell. A complete liquid lens is shown on the right.

The purchased lens that is used throughout all experiments in this thesis is a Varioptic Arctic 39N0³⁴ with a useful optical diameter of 3.5 mm. Figure 3.6 shows the two lenses of the first generation³⁵. Over the course of the measurements presented in Chapters 4 and 5, two different generations of liquid lenses have been used. Table 3.2 summarises the properties of the second generation as given by the LL manual [177]. The slightly different specifications of the first generation as used for the experiments presented in Chapter 4 can be found in the old manual [178].

Since our focus is on studying the LL surface, Equation (3.10) has to be analysed in detail to predict the exact behaviour for the real LL. The actual geometry of the liquid lens as shown in Figure 4.1 is not cylindrical. In fact the shape is conical in the vicinity of the liquid surface and this causes the radius of the liquid surface R to be voltage dependent.

³⁴The exact product name and its specifications have been changed during recent years. The current name is A-39N0. The additional symbol 0 indicates that the lens is covered with an anti-reflective coating optimised for the visible range.

³⁵Both LLs cannot be used anymore. The first one exploded due to a too high voltage and the resulting electrochemical processes and the second one was violated by the fingerprints of a Chinese astronomer, who was unfortunately granted a lab tour.

Parameter	Typical value
Useful aperture	3.5 mm
Front aperture	4.09 mm
Back aperture	6.5 mm
Optical power P	$-5 < P < 15 \text{ m}^{-1}$
AC Input voltage	24 – 70 V
Voltage @ 0 optical power	45 V
Wavefront error	50 nm
Optical axis stability	0.8 mrad
Transmittance @ 587 nm	97 %
Response time	35 – 70 ms
Capacitance @ 1 kHz	500 pF
Operating temperature T_{OP}	$-20 < T_{OP} < +60 \text{ }^{\circ}\text{C}$
Refractive index oil @ 589.3 nm	1.495
Abbe number oil	34.63
Refractive index water @ 589.3 nm	1.386
Abbe number water	58.13

Table 3.2.: Specifications of the second generation of Arctic 39N0 lenses [177]

4. Study of surface modes on a vibrating electrowetting liquid lens

Creating a tunable linear grating on a circular liquid lens (LL) is difficult especially because the purchased liquid lens only allows circular symmetric actuation with its two electrodes. The surface modes are not simple sine waves, so their behaviour has to be studied carefully to be able to make use of them. The main results of this study as presented in this chapter have been published in *Applied Physics Letters* [179]³⁶. The necessary optical components to perform the experiments were provided by Sylvania F. Pereira. Roland Horsten built and designed the electrical signal amplifier and programmed an initial LabView program to drive the LL. Bianca Harrewijn built the basic optical setup during her internship and helped integrating live camera analysis tools into the software.

The increased usage of LLs motivates us to investigate surface waves on a liquid lens surface. During fast focal switching the surface waves decrease the imaging quality. In this chapter, we propose a model that describes the surface modes appearing on a liquid lens and predicts the resonance frequencies. The effects of those surface modes on a laser beam are simulated using Fresnel propagation³⁷ and the model is verified experimentally.

4.1. Known performance impacts of surface vibrations

Liquid lenses are tools to create small tunable optics without any moving parts. As described in Section 3.1 the first mass-producible commercial electrowetting lenses were developed by Bruno Berge and Jérôme Peseux in 1997 [159–161, 180]. Since then many other techniques have been tested to create a focus-tunable lens i.e. using membranes and acoustic waves [132, 147, 157, 181, 182]. While some techniques never left the lab environment, electrowetting, tunable acoustic gradient index of refraction (TAG) and membrane lenses are available commercially [133, 155, 164]. The most popular type of liquid lenses uses the electrowetting effect to manipulate a liquid-liquid interface with an external voltage. These lenses use two liquids with similar density to avoid any gravity influences. A major drawback next to the energy consumption is that the speed of operation of the lens is limited by the liquid inertia of the liquid. When switching between two focal positions too fast, surface waves are created and in consequence the image suffers from aberrations.

³⁶Parts of this chapter are reprinted from M. Strauch, Y. Shao, F. Bociort, and H. P. Urbach, “Study of surface modes on a vibrating electrowetting liquid lens,” *Appl. Phys. Lett.*, vol. 111, p. 171106, Oct. 2017, with the permission of AIP Publishing.

³⁷The simulation code was provided by Yifeng Shao.

While LLs can avoid astigmatism by using several electrodes, in particular spherical aberration is challenging for example in dual beam auto focussing systems [183], even without switching the focal length. In membrane-based LLs the thickness of the membrane can be varied to minimise aberrations [149, 151, 152, 184, 185]. There are promising developments for electrowetting liquid lenses with multiple liquid interfaces [186] and it has been shown that spherical aberration can be corrected in micro-lenses by controlling the hydrostatic pressure [162, 163], but there has been no technique for a single electrowetting-only macroscopic LL to tackle the spherical aberration, yet. The hope to make use of surface waves caused by fast switching to control, introduce, and correct for aberrations motivates us to study their nature in detail.

4.2. Liquid surface model

Oscillations on liquid droplets have been studied intensively [187], including a complete solution for the eigenfrequencies of a viscous droplet in another viscous fluid [188, 189], nonlinear oscillations [190], and constrained liquid droplets [191]. For simplicity, the liquid is assumed to be incompressible and inviscid [192]. Due to the small size of the droplet we limit our investigation of surface vibrations to capillary waves following the approach of Landau and Lifshitz [193].

Suppose that a curved surface in a thermodynamic equilibrium is caused by a small pressure difference Δp between the two adjacent media. This equilibrium is described by the Young-Laplace Equation (3.2) as given in Section 3.2.1. For small surface deviations the Young-Laplace equation can be written as:

$$\Delta p = -\sigma_{\text{lo}} \left(\frac{\partial^2 u}{\partial x^2} + \frac{\partial^2 u}{\partial y^2} \right), \quad (4.1)$$

where σ_{lo} is the surface tension of the liquid-oil interface and $u(x, y)$ is the shape of the surface. In the case of a non-stationary situation the linear Bernoulli equation is

$$p = -\rho \frac{\partial \phi}{\partial t} - \Phi, \quad (4.2)$$

with $\Delta \rho$ the difference in mass density between the adjacent media, t the time, ϕ the velocity potential defined by $\partial u / \partial t = \nabla \phi$, and $\Phi = \rho_A \partial^2 u / \partial t^2$ the potential of the inertial force, with ρ_A the displaced areal mass density. Applying the Bernoulli equation on the Young-Laplace equation yields

$$\Delta \rho \frac{\partial \phi}{\partial t} + \Phi = \sigma_{\text{lo}} \left(\frac{\partial^2 u}{\partial x^2} + \frac{\partial^2 u}{\partial y^2} \right). \quad (4.3)$$

In a liquid lens the densities of the adjacent fluids are identical, i.e. $\Delta \rho = 0$, hence Equation (4.3) simplifies to a linear wave equation of $u(x, y, t)$

$$\frac{\partial^2 u}{\partial t^2} = \frac{\sigma_{\text{lo}}}{\rho_A} \left(\frac{\partial^2 u}{\partial x^2} + \frac{\partial^2 u}{\partial y^2} \right). \quad (4.4)$$

The obtained differential equation is a standard wave equation with the speed of the waves given by $c = \sqrt{\sigma_{10}/\rho_A}$. Thus, the waves on the LL surface are modelled as transverse vibrations of a circular membrane, of which the surface tension dominates the stiffness. With respect to the polar coordinates r and ϕ Equation (4.4) becomes [194]:

$$\frac{\partial^2 u}{\partial t^2} = c^2 \left(\frac{\partial^2 u}{\partial r^2} + \frac{1}{r} \frac{\partial u}{\partial r} + \frac{1}{r^2} \frac{\partial^2 u}{\partial \phi^2} \right). \quad (4.5)$$

with the boundary condition following from the EWOD equation (3.6)

$$\left. \frac{\partial u(r, t)}{\partial r} \right|_{r=R, t=0} = -\tan \theta, \quad (4.6)$$

where θ is the surface deflection angle compared to the surface at rest for the membrane with radius R .

The speed of the waves c is unknown if the properties of the liquid are not known, as it is the case for the Arctic 39N0 series. It is equal to the speed of waves within the approximation of a classical membrane, but the actual speed of the waves differs from $\sqrt{\sigma_{10}/\rho_A}$ in a more thorough model of a liquid, in which the Bernoulli equation has not been linearised by neglecting the displacement-dependent second-order term $-\partial/\partial t(u^2/2)$. The value of c will have to be determined later on to make the linear model sufficiently accurate.

The LL has only two electrodes, which are placed moreover all around the LL, therefore the electrodes can only provide a circularly symmetric actuation voltage. Hence the third term at the right-hand side of Equation (4.5) vanishes. Radially symmetric solutions of Equation (4.5) can be obtained by the method of separation of variables: $u(r, t) = \mathcal{R}(r)\mathcal{T}(t)$, for some functions \mathcal{R} and \mathcal{T} . Substitution into Equation (4.5) yields:

$$\frac{1}{c^2 \mathcal{T}} \frac{\partial^2 \mathcal{T}}{\partial t^2} = \frac{1}{\mathcal{R}} \left(\frac{\partial^2 \mathcal{R}}{\partial r^2} + \frac{1}{r} \frac{\partial \mathcal{R}}{\partial r} \right) \equiv K, \quad (4.7)$$

where K is a constant independent of r and t . The two resulting differential equations can be easily solved. The time-dependent equation is the standard harmonic oscillator equation with solution

$$\mathcal{T} = \mathcal{T}_1 e^{\sqrt{K}ct} + \mathcal{T}_2 e^{-\sqrt{K}ct}. \quad (4.8)$$

The solution is growing exponentially for $K > 0$ and is constant for $K = 0$. It is periodic for $K < 0$, with frequency $f = -i\sqrt{K}c/(2\pi)$.

$$\mathcal{T} = \mathcal{T}_1 e^{i2\pi ft} + \mathcal{T}_2 e^{-i2\pi ft} = C_1 \cos(2\pi ft) + C_2 \sin(2\pi ft), \quad (4.9)$$

with the proportionality constants \mathcal{T}_1 , \mathcal{T}_2 , C_1 , and C_2 . The radius-dependent equation

$$\frac{\partial^2 \mathcal{R}}{\partial r^2} + \frac{1}{r} \frac{\partial \mathcal{R}}{\partial r} - K\mathcal{R} = 0, \quad (4.10)$$

is a special case of Bessel's differential Equation (5.2) with solutions: the Bessel functions of first J_0 and second kind Y_0 and 0th order.

$$\mathcal{R} = C_3 J_0\left(\frac{2\pi f}{c}r\right) + C_4 Y_0\left(\frac{2\pi f}{c}r\right), \quad (4.11)$$

with the proportionality constants C_3 and C_4 . The second term leads to unphysical results $Y_0(r \rightarrow 0) = -\infty$, therefore $C_4 = 0$. If we assume that at $t = 0$ the displacement is maximum, the general time-harmonic solution is:

$$u = A \cos(2\pi ft) J_0\left(\frac{2\pi f}{c}r\right), \quad (4.12)$$

where A is the amplitude.

The step from an undamped vibrating membrane to an undamped liquid surface is a change in boundary conditions. While in the case of a drum the membrane is fixed at the outer boundary $r = R$, in the electrowetting case the boundary condition 4.6 prescribes the slope at the boundary [167]

$$\left. \frac{\partial u(r, t)}{\partial r} \right|_{r=R, t=0} = -\tan \theta, \quad (4.13)$$

where θ is the surface deflection angle compared to the surface at rest for the membrane with radius R . By applying the boundary condition we get for the amplitude³⁸

$$A = \frac{c \tan \theta}{2\pi f J_1\left(\frac{2\pi f}{c}R\right)}. \quad (4.14)$$

By setting the denominator in this expression to zero³⁹ we obtain the resonance frequencies of the undamped oscillator:

$$f_n = \frac{c}{2\pi R} j_{1,n}, \quad (4.15)$$

where $j_{1,n}$ is the n th root of the Bessel function of first kind and 1st order.

The orthogonality properties of the Bessel function are explained in detail in Section 5.2.1. The Bessel functions $J_0(j_{1,n}r/R)$ form an orthogonal basis function, when the argument is scaled, so any radially symmetric surface shape can be described by linear combination. Controlling these surface vibrations may give us the possibility to temporarily design different surface shapes by superposition, like it is done for example in laser pulse shaping [195]. By measuring the mode frequencies and the corresponding surface shapes experimentally, the nature of the surface vibrations and the shape of the surface can be determined [196]. In this way the accuracy of the presented linear theory can be verified.

³⁸ $dJ_0(r)/dr = -J_1(r)$

³⁹In practice however, the amplitude does not diverge because of damping.

4.3. Approximations and limitations

Since the theory of an undamped vibrating surface can only be an approximation of the experimental situation, we have to point out a few differences between theory and experiment and to check afterwards, whether the simple undamped model is sufficiently accurate to describe the behaviour of the real liquid surface. The used liquid lens is a first-generation Arctic 39N0 LL from Varioptic⁴⁰ as displayed in Figure 3.6 [178]. As indicated in Section 3.3.1, the shape of the liquid container is not cylindrical as assumed by the model, but conical in the vicinity of the liquid interface (Fig. 4.1). Hence, the size of the membrane slightly changes during vibration. In the static case, the radius of the interface depends on the LL interface curvature and therefore on the applied voltage U . It can be fitted to the data given by the manual [178]:

$$R(U) = R_0 + R_1 U, \quad (4.16)$$

with the fit parameters $R_0 = (3.193 \pm 0.006)$ mm and $R_1 = -(12.5 \pm 0.1)$ $\mu\text{m}/\text{V}$. Because the mode frequencies depend on the radius (see Eq. (4.15)), they also depend on the applied voltage amplitudes when the lens is continuously driven. For small oscillations as investigated in this Chapter the introduced frequency shift compared to the resonance frequencies of an undisturbed surface is $\approx 1.5\%$, but it can go up to more than 20% for larger fluctuations. In consequence, the conical shape of the LL limits the applicability of the model to the first 64 modes for the applied small oscillations, where the resonance frequencies of disturbed and undisturbed surfaces start overlapping. In the case of a flat undisturbed surface the surface radius is $R = (2.65 \pm 0.01)$ mm.

The vibration of a real liquid is damped by the viscosity and the friction at the walls. Therefore the oscillator has to be driven with an external driving voltage to keep the lens oscillating. The dependence of the deflection angle θ (in radians) on the voltage can be fitted to the data given by the manual [178]. The optical power depends quadratically on the applied voltage (see Eq. (3.10) & Fig. 3.5). For small contact angles, the contact angle is proportional to the optical power, which can be linearised in the vicinity of a flat surface. Please note that the angle of deflection θ is not the contact angle ϑ as used in the EWOD Equation (3.6). They are linked via the geometry by $\theta = 3\pi/4 - \vartheta$, i.e. the side wall angle is 45° (Fig. 4.1):

$$\theta = \theta_0 + \theta_1 U, \quad (4.17)$$

with the fit parameters $\theta_0 = -0.949 \pm 0.007$ and $\theta_1 = (2.27 \pm 0.01) \times 10^{-2} \text{V}^{-1}$.

When the control voltage amplitude is small and oscillates at or close to a resonance, the liquid surface is a standing wave at the resonance frequency. Since the system is damped, a continuous driving force is required to create a steady oscillation. As follows from Equation (4.14) and Equation (4.17), the amplitude A of the standing wave depends non-linearly on the voltage U . To be able to use the linear model, it is necessary to stay within the regime of small deflection angles. A simulated comparison of the non-linear model and the linearised model is shown in

⁴⁰Today: Corning [164]

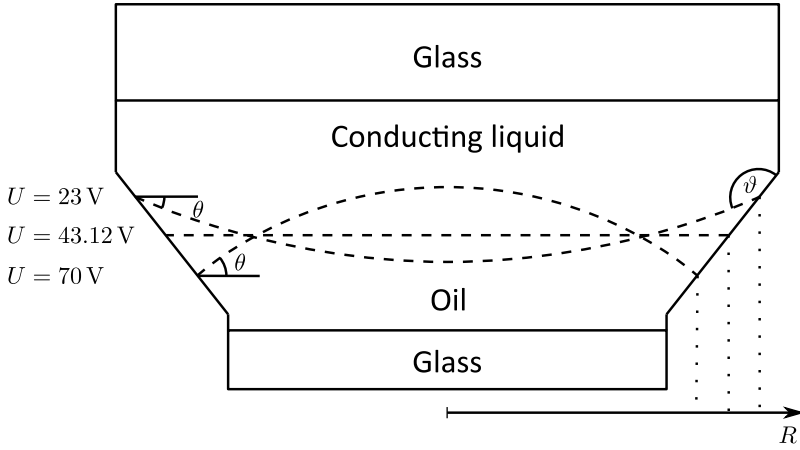


Figure 4.1.: Schematic static profiles of the Arctic 39N0 liquid lens. The dashed lines show possible static interface curvatures to scale for different voltages U as given by the Arctic39N0 manual [178] and the provided Zemax model of the lens. θ indicates the deflection angle. ϑ is the contact angle.

Figure 4.2 for a small voltage oscillation, as used in this chapter and an extremely large one. While the amplitude deviation due to linearisation is below 1% for the applied small oscillations, it can become more than 25% for larger oscillations. The deviation from the cosine behaviour introduces additional frequency components which stimulate multiple modes at the same time during the experiments.

4.4. Measurement setup

For experimental verification we use the first-generation Arctic 39N0 LL model by Varioptic [178]. A summary of its properties can be found in Table 3.2. Some details however differ from the second generation of liquid lenses and are therefore listed here. The optical power is -5 m^{-1} to 15 m^{-1} for applied voltages ranging from 36 V to 58 V. The focal switching speed is limited to 25 Hz (i.e. 20 ms between the two extreme foci⁴¹). The refractive indices of the two used liquids are $n_1 = 1.3846$ and $n_2 = 1.4921$ at $\lambda = 632.8 \text{ nm}$. A flat interface is obtained for a voltage of $U = 43.12 \text{ V}$. The environment temperature is 21°C . The optical power of the lens depends on the temperature and has had the largest impact on the reproducibility of the measurements. The actuation voltage to obtain a flat surface shifts $\approx 0.7 \text{ V}/^\circ\text{C}$ at 21°C . The diameter of the lens aperture is $d = 3.95 \text{ mm}$.

A collimated HeNe laser beam with a Gaussian beam profile and a FWHM of 8 mm illuminates the LL surface. The intensity distribution of the modified beam is measured with a camera at a distance of 50 cm behind the LL, i.e. in the Fresnel

⁴¹Depending on the required switching and imaging quality the manufacturer advises to use a three times slower switching speed of 60 ms [178].

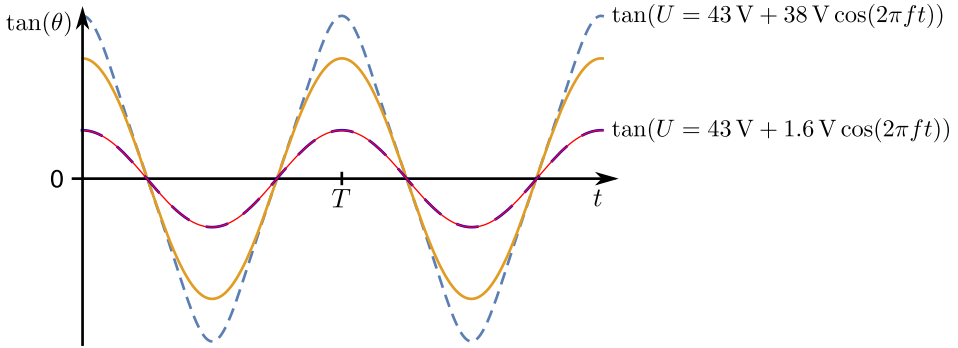


Figure 4.2.: Comparison of the linear approximation of $\tan(\theta(t))$ and the exact solution for a small and a large amplitude. The dashed lines show the tangent exactly. The solid lines show $\tan \theta = \cos(2\pi t/T)$ with the period of the surface wave $T = 1/f$. To increase readability $\tan(U = 1.6V)$ is multiplied by 10.

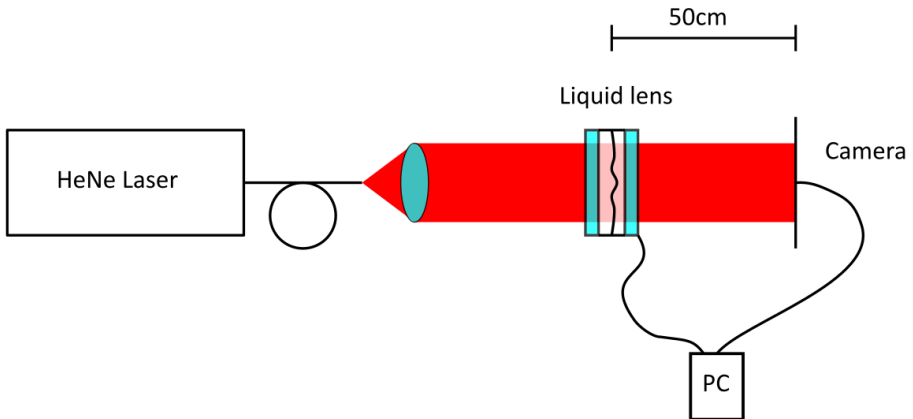


Figure 4.3.: The HeNe laser light is coupled out of a fibre, the beam is collimated, passes the liquid lens and is detected by a camera connected to a computer. Both the camera and the liquid lens are controlled by the computer.

region (Fig. 4.3). The experiment was carried out both with an SVS-VISTEK eco424MVGE industrial camera and a Photron SA3 high-speed camera. The first one was provided by Silvania F. Pereira from Katsiaryna Ushakova’s lab and the second one by Nandini Bhattacharya⁴². The high-speed camera was used to sample the motion of the lens surface within a single oscillation, while the industrial camera is able to sample it over several oscillation cycles. The specifications of all used cameras are summarised in Table 4.1. The image acquisition is synchronized to the voltage supply of the liquid lens. Appendix B gives a detailed overview, how triggering the camera and the voltage supply are realised experimentally using LabVIEW.

	Photron SA3	eco424MVGE	eco655MVGE
Resolution	1024 × 1024 px	656 × 492 px	2448 × 2050 px
Max. frame rate	120000 fps	124 fps	10 fps
Min. exposure time	2 μs	3 μs	7 μs
Bit depth	12 bit	8 bit	8 bit

Table 4.1.: Specifications of the used cameras

The simplicity of the setup facilitates the simulation and prediction of the intensity measurements for several parameter values using the linear model. By fitting the simulated to the measured intensity patterns, the speed of the waves c can be determined.

4.5. Simulation of a liquid lens using Fresnel propagation

The simulation was carried out both using a geometrical optics and a physical optics model. In LightTools the setup was simulated by means of geometrical optics, but the simulation has not been able to predict the diffraction effects introduced by the lens aperture⁴³. The deviation of the simulation from the experimentally observed light pattern increases with the actuation frequency f , because LightTools does not include any diffraction effects. Figure 4.4 shows the prediction for the ground mode f_1 at $t = T/2$ with the period of the surface wave $T = 1/f$. The LightTools algorithm is also much slower than the physical optics simulation.

A wave optics model instead delivered accurate results. The delay of the incident plane wave is proportional to the optical path length inside the two liquids. The wavefront is propagated to the detector using Fresnel propagation and converted

⁴²The Photron SA3 high-speed camera was only available for two weeks, therefore the cheap low quality alternatives were necessary.

⁴³LightTools can be best controlled externally via the Microsoft Excel-based macro Visual Basic programming environment. Since the attempts to carry out these simulations have not reached the required accuracy, an exact description of how to do this will be omitted.

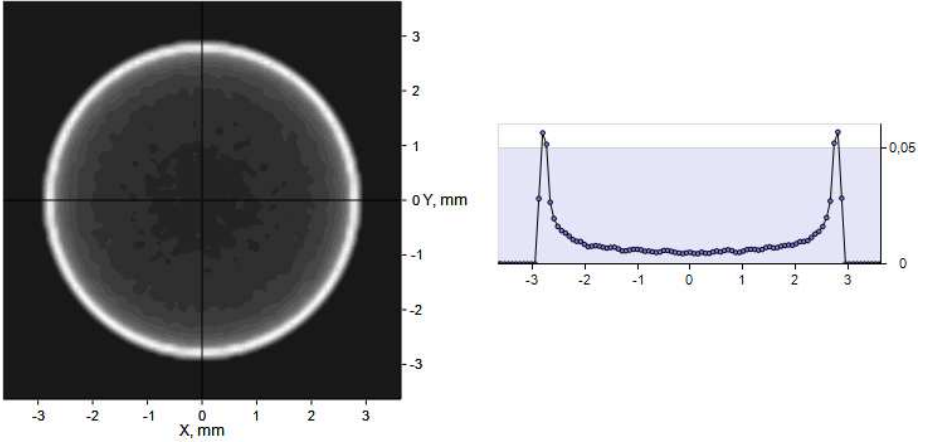


Figure 4.4.: Simulation of the light pattern for the ground mode f_1 with LightTools. The intensity distribution at the detector plane at $z = 50$ cm is shown on the left and an intensity profile along the x -axis is shown on the right. The LightTools simulations do not include any diffraction effects and are therefore only able to describe the ground mode behaviour f_1 with the required accuracy.

into a intensity pattern EE^* . The initial field immediately behind the lens

$$E(x', y', z = 0, t) = \exp \left[i \frac{2\pi(n_2 - n_1)}{\lambda} u \left(\sqrt{x'^2 + y'^2}, t \right) \right], \quad (4.18)$$

is propagated to the detector plane $z = 50$ cm using [197, 198]

$$E(x, y, z, t) = \frac{\exp(i \frac{2\pi}{\lambda} z)}{i\lambda z} \times \int \int_{-\infty}^{\infty} E(x', y', 0, t) \exp(i \frac{\pi}{\lambda z} [(x - x')^2 + (y - y')^2]) dx' dy'. \quad (4.19)$$

The Fresnel approximation is valid for the given aperture diameter and wavelength for distances longer than $\sqrt[3]{r^4/(4\lambda)} = 1.8$ cm behind the liquid lens, which includes our measurement distance clearly. For smaller apertures or distances larger than $2d^2/\lambda = 50$ m the simpler Fraunhofer model is sufficiently accurate. The MATLAB code calculating the Fourier transform using a chirp Z-transform has been provided by Yifeng Shao. The first row of Figure 4.6(a) shows the results of the simulated fundamental mode for both extreme surface deflections at $t = 0$ and $t = T/2$. While the resonance frequencies are predicted by the model, the amplitude can be chosen freely. In the displayed cases it was chosen to be small, i.e. in the range of $3 \mu\text{m}$ to $14 \mu\text{m}$. The maximum of the introduced optical path length difference is then approximately 0.5–2 wavelengths. The other rows show the higher resonance modes. It can be observed, that the number of dominant

rings with maxima equals the resonance mode number.

4.6. Confirmation of the membrane model

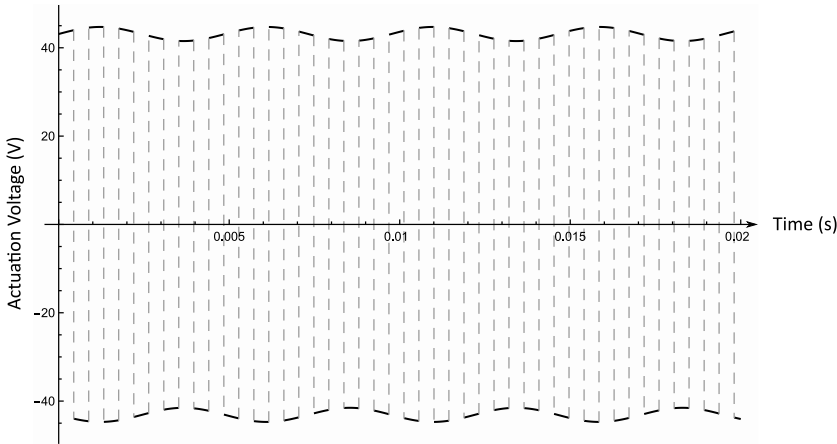


Figure 4.5.: Typical voltage input $U = 43.12 \text{ V} + 1.6 \text{ V} \sin(2\pi t \times 205 \text{ Hz})$. All voltage inputs are modulated with a 1136 Hz square wave.

The liquid lens is tuned to a flat surface by applying 43.12 V. A small alternating current (AC) cosine signal with amplitude 1.6 V is added on top to excite surface modes (Fig. 4.5). The voltage variation is chosen to be small to assure that the lens surface can be described linearly. The frequency is varied between 10 Hz and 250 Hz. The liquid lens is always operated in AC mode as explained in Section 3.3, therefore all actuation voltages are modulated with a 1136 Hz square wave⁴⁴. The exposure time of the high-speed camera is 50 μs . Since the speed of the surface waves c is yet unknown, the resonance frequencies have to be determined experimentally. The fundamental mode can be identified by comparing the simulated intensity patterns and the experimental data. It occurs at $f_1 = 59 \text{ Hz}$. The next three higher modes can be found in the same way: $f_2 = 108 \text{ Hz}$; $f_3 = 157 \text{ Hz}$; $f_4 = 205 \text{ Hz}$. Figure 4.6 shows simulated and measured intensity snapshots of the deflections of the first four modes at two instances of time $t = 0$ and $t = T/2$ at which the deflection is maximum. A video of the first LL modes is available [online](#) [179]. The comparison of the measurements and the simulated intensities shows only minor deviations in the general shape of the light patterns. The measurement of the ground mode at 59 Hz is slightly overexposed and therefore appears to be sharper than the simulation. Also note that the result of the Light-Tools simulation in Figure 4.4 fails to predict any of the minor fringes. The small vertical fringe patterns observed in all measurements appear due to Fabry-Pérot interference in the camera.

⁴⁴More details on the signal generation using LabVIEW are given in Appendix B.

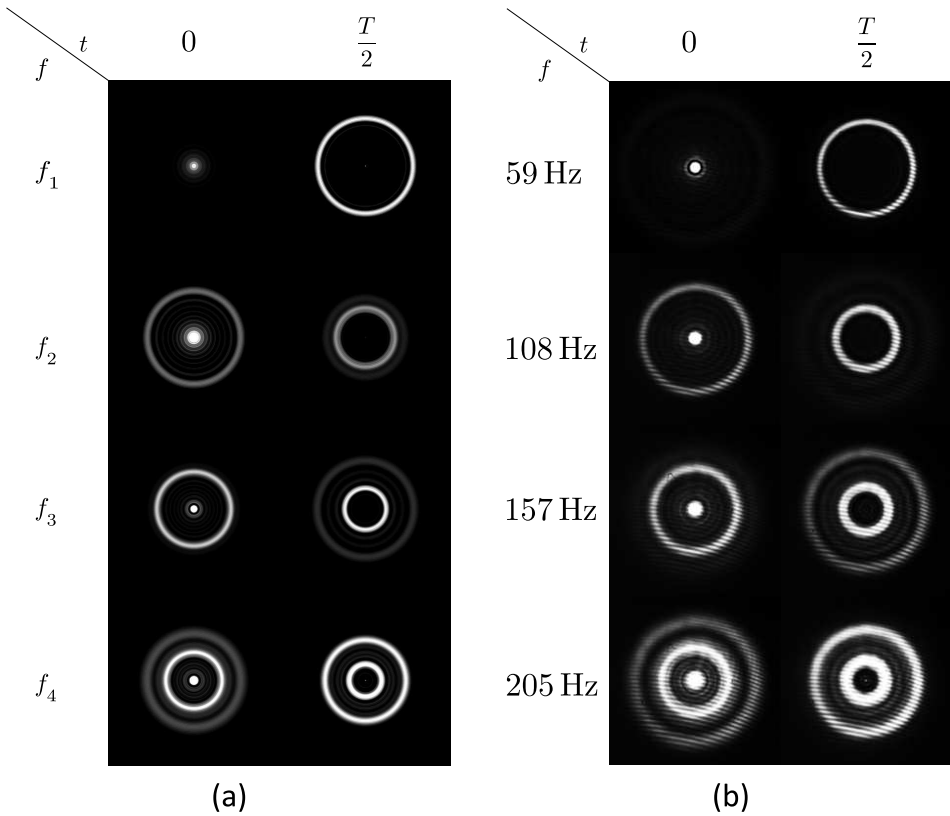


Figure 4.6.: Intensity patterns of the first four modes at $z = 50$ cm behind the lens as obtained from Fresnel simulations (a) and from measurements with the high speed camera (b). The times $t = 0$ and $t = T/2$ correspond to instances that the deflection of the surface wave is maximum. The exposure time is $50 \mu\text{s}$.

Using the experimentally determined frequency of the first resonance mode and Equation (4.15), the speed of the waves on the LL surface can be calculated: $c = 2\pi R f_1 / j_{1,1} = (26 \pm 6) \text{ cm/s}$. The value is in the expected range for aqueous solutions. This quantity can now be used in simulations of the behaviour of the liquid lens for different voltages and frequencies to create different surface shapes.

The experimentally determined mode frequencies $f_{1,2,3,4}$ are in agreement with Equation (4.15). This additionally validates the proposed undamped model. The mode frequencies are much smaller compared to those of the tunable acoustic gradient index of refraction (TAG) lenses discussed in Section 3.1.1 [132] ($> 100 \text{ kHz}$) and do not require costly high speed cameras or high precision flash light sources. For higher modes though, the measured resonance frequencies are higher than as predicted by our linear Bessel-based surface resonance model. This deviation is probably caused by the larger influence of friction at the walls for higher frequencies, which changes the Neumann boundary condition to a Robin⁴⁵ boundary condition [199].

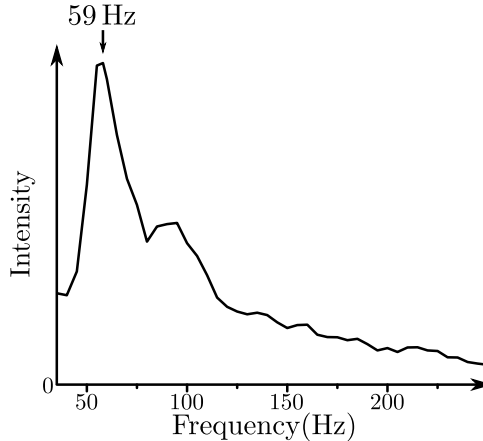


Figure 4.7.: Measured intensity on the optical axis versus the modulation frequency at $t = 0$. The intensity shows a maximum at the fundamental mode $f_1 = 59 \text{ Hz}$. Higher modes are not visible in the graph since the intensity is split up between the central peak and the surrounding rings.

The influence of damping can be made visible by analysing the frequency response of the system. A way to show the sharpness of the fundamental mode is measuring the intensity on the optical axis at $t = 0$ (Fig. 4.7). Independent of the mode number, the intensity is expected to be maximum on the optical axis. However, the higher modes are not visible in the graph, because the intensity is distributed between the on-axis peak and the surrounding rings. The influence of damping is not unexpected since the LL manufacturer artificially increases the

⁴⁵Robin boundary conditions are a linear combination of Dirichlet (no-slip) and Neumann (slip) wall boundary conditions.

damping to optimize the response time and to suppress oscillations [160].

For high resonance amplitudes, the frequencies also shift and multiple modes are stimulated at the same time. This happens due to the non-linearity of the model in both the radius dependency of the resonance frequencies (4.15) and the tangent-dependency the boundary condition at the edge of the amplitude (4.14). Ultimately the amplitude of the surface waves is limited by the distance between the glass windows of the LL (Fig. 4.1).

4.7. Applicability

Surface modes on a liquid lens can be described with a membrane model that is based on the assumption of an inviscid incompressible liquid droplet. The simulated intensity patterns based on a vibrating surface match the experimentally observed behaviour. The experimentally dominating low frequency modes can be fully described and predicted with the developed model. High amplitudes and frequencies though, do not fulfil the assumptions of the membrane model because the behaviour becomes non-linear and the resonances are strongly damped. They therefore only play a minor role during fast focal switching and do not cause relevant aberrations. Whether the obtained knowledge about the surface waves can be used to improve the switching speed of a LL, or shape the LL surface, such that the phase front can be designed to create a Bessel beam [200,201], avoid aberrations (also in 2D imaging), or to create a phase object for digital holography is the subject of Chapter 5.

5. Creation of a tunable asphere with an electrowetting liquid lens

This chapter demonstrates a technique to create aspheric surface shapes on commercially available electrowetting on dielectric (EWOD) liquid lenses. By proving the validity of the simple linear description of surface waves on a liquid lens (LL) in Chapter 4, we have found an answer on the question: How does the surface of a LL behave when the focal length is changed faster than the reaction time of the lens? The linear model of surface oscillations on the LL as such however, has not been proven to be useful for the standard liquid lens user, yet. During common operation of a liquid lens fast focal switching causes aberrations, due to surface waves, so a new question arises: Is it possible to make use of the surface waves to design useful surface shapes, now that we can model them? If a technique exist, that enables us to design new surface shapes with surface on the LL, the technique will have one general advantage: surface modes can be produced by any user of an EWOD LL without making changes to the LL hardware. Next to electrowetting (EW), the model of surface waves can be applied to membrane LLs, too, especially because here it is an actual membrane that has to be modelled. Only the boundary conditions would have to be adjusted, since the membrane is fixed at its outer rim. The Bessel shape of the surface waves creates Bessel phase profiles, but also more general phase profiles can be obtained by making more diverse surface shapes by superposition.

There are two starting points to derive a method to design useful surface shapes on a liquid lens: either creating a desired surface periodically by linear combination of resonant modes or pulsed by linear combination of all actuation frequencies except for the resonant modes. The second approach has been published in AIP Advances [202] and will be the main focus of this chapter. Observing and measuring the exact created surface functions was only possible with the additional support of Peter A. A. M. Somers, who helped choosing, designing and evaluating an interferometric setup.

Based on the model of surface oscillations in Chapter 4, we will propose a technique using a Hankel transform and test it experimentally. An alternating current (AC) actuation voltage is applied to the liquid lens to stimulate surface oscillations, that add up to the desired surface shape at discrete moments in time. The voltage signal can be repeated at video rate. The measurements are taken with a Mach-Zehnder interferometer and confirm the observations of Chapter 4. The capabilities and limitations of the proposed method are demonstrated using the examples of a Bessel surface, spherical aberration, an axicon, and a top hat structure.

5.1. Aberration correction with liquid lenses

The switching performance of electrowetting liquid lenses is limited by surface oscillations. Already when the first liquid lenses were developed, it became clear, when the focal distance is switched too fast, the inertia of the liquid prevents the liquid surface from following the change instantaneously [160,161]. Then surface waves are created. These uncontrolled deviations from a spherical interface were identified as the cause of dynamic aberrations and have limited the operational speed of liquid lenses. All liquid lenses therefore have a response time⁴⁶, which depends on the chosen materials and the lens size, that limits their high-speed application.

Recent works minimised the response time of a LL by optimizing the choice of liquids and surface roughness as well as surface coatings of the LL package [172,176]. But also static aberrations, especially spherical aberration, limit the performance in some applications [183] and in consequence, many new lenses have been developed to create aspheric liquid lenses, e.g., an ultrasonic liquid crystal lens [203] and a LL making use of thermal Marangoni forces [204] to shape the surface. Also, the combination of hydrostatic pressure and electrowetting or the use of multiple liquid interfaces promises to extend the functionality of a liquid lens [162,163,186,205]. However, only the simple electrowetting LL has been commercialised.

Our alternative approach is to study the nature of the excited surface waves on a commercially available liquid lens and its resonance modes in order to avoid, or even to make use of them (Chap. 4). By exciting the liquid interface faster than the response time of the LL, waves can be created on purpose to create new optical surface shapes. The resonant modes have the shape of Bessel functions and can be excited individually. A similar approach, published just a month after our original paper, focusing on the application of surface waves on a liquid lens for optical encryption came to the same conclusion [206,207]. Surface oscillations of liquid droplets have been studied thoroughly elsewhere [187,191], providing a good overview of liquid immersion and viscosity effects [188,189], that need to be considered to understand the non-linearity of the liquid oscillations [190]. However, a linear dispersion relation based on an inviscid and incompressible model of the liquid (Sec. 4.2) [192,193] was confirmed experimentally for small surface excitations up to a few optical path lengths (OPL).

5.2. Construction of a desired surface shape using Bessel functions

Surface vibrations on a liquid droplet and more specifically a LL can be described by Bessel functions of first type and 0th order J_0 for sinusoidal actuation (Sec. 4.2)

⁴⁶The response time as such is a term that is not commonly defined for liquid lenses. It often refers to the time between the actuation voltage change and the point in time, when the optical power reaches 90% of its final value. See also Table 3.2.

[193,208]. The properties of the Bessel-function are advantageous for creating new surface shapes by superposition and are summarised in this section.

5.2.1. Orthogonality of the Bessel function

As previously indicated the scaled Bessel functions are orthogonal. However, it has not been explained, yet, why this is the case. Two functions f_i, f_j are orthogonal if their inner product is $\langle f_i, f_j \rangle_w = 0$ for every $i \neq j$, where the inner product is defined over an interval $[a, b]$ as

$$\langle f_i, f_j \rangle_w = \int_a^b f_i(x)f_j(x)w(x) dx, \quad (5.1)$$

for a non-negative weight function $w(x)$ [209].

The Bessel function $J_\nu(kr)$ is the solution to Bessel's differential equation⁴⁷

$$r^2 \frac{d^2 J_\nu(kr)}{dr^2} + r \frac{dJ_\nu(kr)}{dr} + (k^2 r^2 - \nu^2) J_\nu(kr) = 0, \quad (5.2)$$

with the order of the Bessel function $\nu \geq -1$, and a scaling factor k along the radial coordinate axis r . By rearranging, the Bessel equation transforms into an eigenvalue equation:

$$-\left(\frac{d^2}{dr^2} + \frac{1}{r} \frac{d}{dr} - \frac{\nu^2}{r^2} \right) J_\nu(kr) = k^2 J_\nu(kr). \quad (5.3)$$

Eigenfunctions of self-adjoint operators are orthogonal $(\lambda_j - \lambda_i) \langle f_i, f_j \rangle = 0$. The weight function is given by Sturm-Liouville theory $w(r) = r$ [209, 210]. With the definition of the inner product (5.1) over the interval $[0, R]$ we get the orthogonality for the Bessel function

$$\int_0^R J_\nu(kr) J_\nu(k'r) r dr \stackrel{!}{=} 0 \quad (5.4)$$

$$\frac{R \left[k' J_\nu(kR) \frac{\partial}{\partial r} J_\nu(k'R) - k \frac{\partial}{\partial r} J_\nu(kR) J_\nu(k'R) \right]}{k^2 - k'^2} = 0. \quad (5.5)$$

The Bessel function is orthogonal, if kR and $k'R$ are roots of the Bessel function J_ν or zeros of its first derivative $\frac{\partial}{\partial r} J_\nu$. Here we limit our focus to $\nu = 0$ such that $\frac{\partial}{\partial r} J_0(r) = -J_1(r)$.

We conclude that the set of functions $J_0(kr)$ with k given by either the zeros of $k \rightarrow J_0(kR)$ or the zeros of $k \rightarrow J_1(kR)$ is an orthogonal set of functions. It can be shown, that the set of Bessel functions $\sqrt{r} J_0(j_{1,n} r/R)$ is complete in the

⁴⁷By comparing the Bessel equation to the radial differential equation solved in Section 4.2, we see that the radial differential Equation (4.10) is indeed the Bessel equation by choosing $\nu = 0$ and substituting $k = \sqrt{K}$.

space of all radial functions $u(r)$ with $\int_0^R u(r)^2 r dr < \infty$ in the interval $[0, R]$. The Fourier-Bessel series

$$f(r) = \sum_{n=1}^{\infty} c_n J_0\left(\frac{j_{1,n}}{R} r\right), \quad (5.6)$$

converges uniformly for all piecewise-smooth functions $f(x)$, with $\partial f(R)/\partial r = 0$, except near discontinuities where it converges to the average of the left- and right-hand limits [211, 212].

For sufficiently large times after switching on the actuator basically any type of surface shape can be created by simple superposition of sinusoidal voltage inputs. The surface u created by a voltage actuation $U(t) = U_0 \cos(2\pi f_0 t)$ with oscillation frequency f_0 and amplitude U_0 is at time t given by Equation (4.12):

$$u = A(f_0) \cos(2\pi f_0 t) J_0\left(\frac{2\pi f_0}{c} r\right), \quad (5.7)$$

where c is the capillary speed of the waves⁴⁸ and A is the amplitude. A desired surface function for $t = 0$ can be expressed as a superposition of such surface functions for different amplitudes $A(f)$ and frequencies f .

$$u(r \leq R, t=0) = \int_0^{\infty} A(f) J_0\left(\frac{2\pi f}{c} r\right) df. \quad (5.8)$$

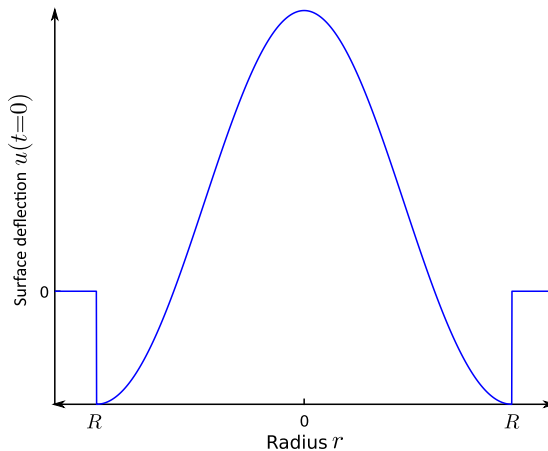


Figure 5.1.: Example for the choice of a desired surface. Here: Bessel ground mode $u(r \leq R) = J_0(j_{1,1}r/R)$. The zero level is chosen such that the integral over the full surface is zero.

The surface shape (Fig. 5.1) is chosen to be zero for all values outside the lens radius R : $u(r > R, t=0) = 0$. To get a specific surface shape $u(r, t=0)$ for

⁴⁸More accurately: the speed of waves in the proposed linear membrane model.

$0 \leq r \leq R$ the exact time dependent actuation signal can be calculated using two basis transforms. First a Hankel transform is applied to $r \rightarrow u(r, t = 0)$ to calculate the amplitude spectrum of the surface function and second an inverse Fourier transform to obtain the time dependent actuation signal for the LL.

5.2.2. Hankel transform

The Hankel transform is an integral transform with the integration kernel $J_\nu(kr)r$ [209] and its properties follow from those of the Fourier transform. We recall the definition of the 2D-Fourier transform

$$\mathcal{F}(\mathbf{k}) = \frac{1}{2\pi} \iint \mathbf{f}(\mathbf{r}) e^{-i\mathbf{k}\cdot\mathbf{r}} d\mathbf{r}, \quad (5.9)$$

where $\mathbf{k} = k_x \hat{\mathbf{x}} + k_y \hat{\mathbf{y}}$. We change the variable \mathbf{k} and the integration variables to polar coordinates and evaluate the Fourier transform on the x -axis: $\mathbf{k} = k_x \hat{\mathbf{x}} = k \hat{\mathbf{x}}$. Then [213]

$$\mathcal{F}(k) = \frac{1}{2\pi} \int_0^\infty dr \int_0^{2\pi} d\varphi r f(r, \varphi) e^{-ikr \cos \varphi}. \quad (5.10)$$

For circular symmetric functions $f(r)$ and using the integral representation of the Bessel function $J_0(x) = 1/(2\pi) \int_0^{2\pi} \exp(ix \cos \varphi) d\varphi$ [209] the Fourier transform simplifies to the Hankel transform \mathcal{H}_0 of order 0 [214]:

$$\mathcal{F}(k) = \int_0^\infty f(r) J_0(kr) r dr \equiv \mathcal{H}_0[f(r)](k). \quad (5.11)$$

The domain of definition is also inherited from the Fourier transform ($\iint |\mathbf{f}(x, y)|^2 dx dy < \infty$):

$$\int_0^\infty |f(r)|^2 r dr < \infty. \quad (5.12)$$

All surface functions without singularities and with $u(r > R) = 0$ fulfil this condition.

Let $u_0(r)$ be the desired rotational symmetric shape of the LL surface that we want to realise at time $t = 0$ by applying some small actuation voltage $U(t)$. The problem then is to find a small voltage actuation $U(t)$ such that $u(r, t)$ satisfies

$$\frac{\partial^2 u(r, t)}{\partial t^2} = c^2 \left(\frac{\partial^2 u(r, t)}{\partial r^2} + \frac{1}{r} \frac{\partial u(r, t)}{\partial r} \right), \quad (5.13)$$

$$\frac{\partial u(R, t)}{\partial r} = -U(t), \quad (5.14)$$

then at time $t = 0$:

$$u(r, t=0) = \begin{cases} u_0(r) & \forall 0 \leq r \leq R \\ 0 & \forall r > R \end{cases}. \quad (5.15)$$

The surface modes of the liquid lens are Bessel functions (see Eq. (5.7)). If we want to construct a desired surface (5.8) by superposition, we need to express it in Bessel functions and find their coefficients. This can be solved by applying the Hankel transform (5.11) on Equation (5.8):

$$\mathcal{H}_0[u(r, t=0)](k) = \int_0^\infty \int_0^\infty A(f) J_0\left(\frac{2\pi f}{c} r\right) J_0(kr) r \, df \, dr. \quad (5.16)$$

The Bessel function closure relation [209, 215] $\int_0^\infty J_n(k'r) J_n(kr) r \, dr = \delta(k' - k)/k$, where $\delta(x)$ is the Dirac delta function, can be applied to replace the radial integral

$$\mathcal{H}_0[u(r, t=0)](k) = \int_0^\infty A(f) \frac{c}{2\pi f} \delta\left(\frac{2\pi f}{c} - k\right) \, df, \quad (5.17)$$

where $k = 2\pi f/c$ is the linear dispersion relation of the membrane model. Because the linear model is only sufficiently accurate for small amplitude waves and relatively low frequencies, the linear dispersion relation is only correct for these amplitudes and frequencies and it must be replaced by a more complicated one in more exact fluid models [208]. Integrating the delta function gives

$$\mathcal{H}_0[u(r, t=0)](k) = \frac{1}{k} A\left(\frac{kc}{2\pi}\right). \quad (5.18)$$

We are now able to determine the amplitude coefficient function $A(f)$ such that $u(r, t)$ satisfies Equations (5.13) and (5.15)

$$u(r, t) = \int_0^\infty \frac{2\pi f}{c} \mathcal{H}_0[u(r, t=0)] \left(\frac{2\pi f}{c}\right) \cos(2\pi ft) J_0\left(\frac{2\pi f}{c} r\right) \, df. \quad (5.19)$$

The electrowetting [167] boundary condition (4.6) determines the contact angle deviation θ of the liquid surface at the lens radius R

$$\left. \frac{\partial u(r, t)}{\partial r} \right|_{r=R} = -\tan \theta(t). \quad (5.20)$$

The voltage actuation signal $U(t)$ is proportional to $U(t) \sim \tan \theta(t)$ for small surface waves. Applying the boundary condition to Equation (5.19) and evaluating it for the derived amplitude spectrum $A(f)$ (see Eq. (5.18)) for a desired surface

$u(t = 0)$ yields the voltage spectrum

$$-U(t) \sim - \int_0^{\infty} \frac{2\pi f}{c} A(f) e^{-2i\pi f t} J_1\left(\frac{2\pi f}{c} R\right) df. \quad (5.21)$$

Hence, with $U(t) = \int_0^{\infty} \hat{U}(f) \exp(-2i\pi f t) df$ we identify

$$\hat{U}(f) \sim \frac{2\pi f}{c} A(f) J_1\left(\frac{2\pi f}{c} R\right) \quad (5.22)$$

$$\sim \left(\frac{2\pi f}{c}\right)^2 J_1\left(\frac{2\pi f}{c} R\right) \mathcal{H}_0[u(r, t=0)]\left(\frac{2\pi f}{c}\right). \quad (5.23)$$

The time-dependent actuation signal is given by the inverse Fourier transform:

$$U(t) = \int_{-\infty}^{\infty} \hat{U}(f) e^{2i\pi f t} df. \quad (5.24)$$

The hereby obtained actuation signal $U(t)$ can now be used to stimulate oscillations on the liquid lens that add up to the desired surface function u at $t = 0$. The obtained signal is in general infinitely long but in fact for finite lens sizes only a short pulse holding non-zero information. Because the surface of the liquid lens is $u(r > R, t = 0) = 0$ outside of the LL, the inverse Fourier transform of the Hankel transformed surface shape is also $U(|t| > 2R/c) = 0$ outside of a time interval centred around $t = 0$. The pulse can be repeated continuously to recreate the desired surface function at video rate.

5.3. Implementation

The presented transforms were implemented in Matlab using its discrete fast Fourier transform (FFT) and the quasi-discrete Hankel transform [216–218]. The Hankel transform is applied on an array containing the desired surface coordinates u at $t = 0$ to obtain the spatial spectrum $\mathcal{H}[u(r, t = 0)](k)$. The spatial spectrum is transformed into the temporal voltage spectrum $\hat{U}(f)$ using Equation (5.23). The resulting voltage signal $U(t)$ is obtained by the inverse FFT. The calculation time to obtain the voltage signal is 24–30 ms on a standard desktop machine (Intel Core i5-3470) independent of the complexity of the desired surface input. An exact explanation including a minimal code example to perform the Hankel transform and the proposed algorithm is presented in Appendix D.

The example of the first resonant Bessel mode $u(r \leq R, t = 0) = J_0(j_{1,1}r/R)$ is used to illustrate the intermediate steps of the algorithm (Fig. 5.1–5.3). The Hankel transform converts a Bessel function into a sharp peak at the resonance frequency. The peak is however broadened and is accompanied by strong side modes due to the introduced cut-off of the surface function at the radius R and the discrete transform. It enforces resulting signals to be of limited duration and

resolution. In other words, the finite radius R of the lens determines the length of the computed actuation signal. The computed signal is therefore always a pulse, even if a continuous signal could be used to achieve the same result. The positive side effect is that a predefined pulse length is predictable and avoids situations, where the periodicity of the continuous signal approaches infinity and makes the technique unusable.

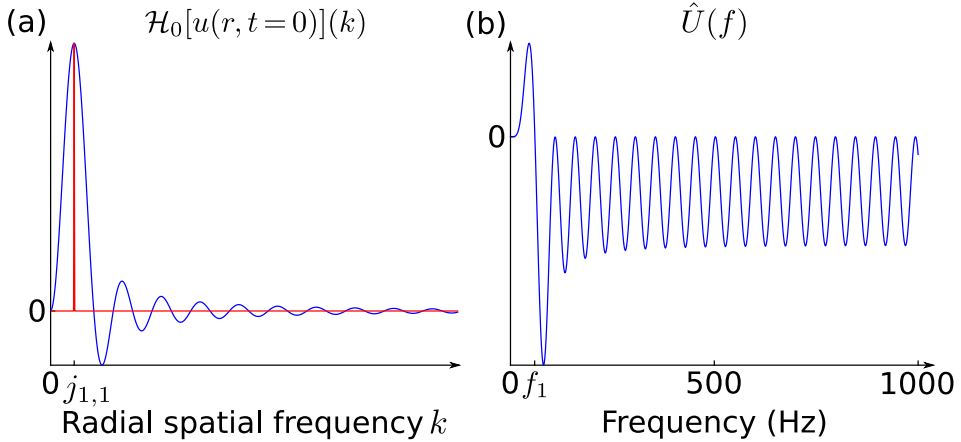


Figure 5.2.: (a) The Hankel transform of the Bessel ground mode with cut-off at $r = R$ as presented in Fig. 5.1 in blue and the Hankel transform of the infinitely extended Bessel ground mode in red. (b) The frequency spectrum of the actuation voltage (see Eq. (5.23)).

To check the validity of the Hankel-transform method, its result is compared to the analytic actuation signal for the second resonant Bessel mode $u(r \leq R, t=0) = J_0(j_{1,2}r/R)$ in Figure 5.4. Within the first half of the pulse, both methods yield identical actuation signals. The second half of the pulse is symmetric and destroys the surface shape to restore a flat surface. At $t = \pm 2R/c = \pm 20.4$ ms the pulse ends. The pulse length resembles the travelling time of a wave on the lens from one side to the opposite side and is given by the ratio of the radius R of the lens and the speed of waves on the LL surface c .

The applicability of the method will be demonstrated experimentally with four different examples: The trivial case of creating a Bessel shape on the LL surface, a Zernike polynomial to address spherical aberrations, a conical surface to create an axicon and a top hat structure to show the limitations of the model.

5.4. Interferometric surface measurements

A picture of the whole setup is displayed in Figure 5.5. The used LL is again a Varioptic Arctic 39N0 [164, 177], but this time taken from the second generation of liquid lenses as described in detail in Table 3.2. In contrast to the previously used liquid lens, the optical power ranges from -5 m^{-1} to 15 m^{-1} for voltages from

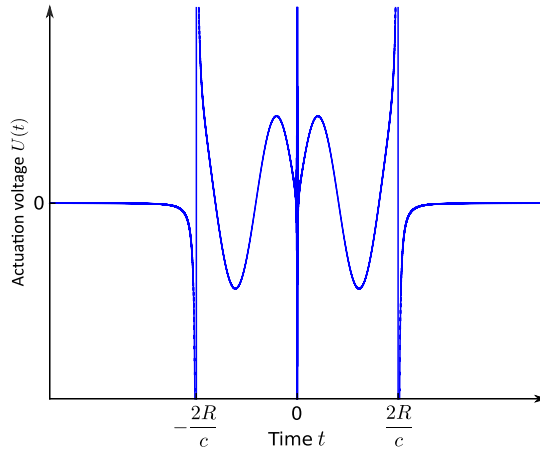


Figure 5.3.: The voltage actuation signal $U(t)$ required to create a Bessel shaped liquid lens surface $J_0(j_{1,1}r/R)$ as displayed in Fig. 5.1.

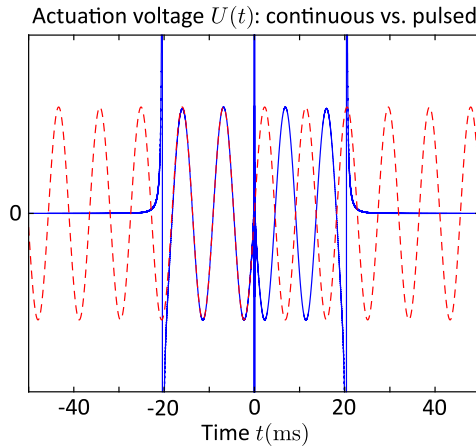


Figure 5.4.: Comparison of the actuation signal for the second resonant Bessel mode on the LL for an infinitely extended lens using the analytic model (red) and for a finite lens radius using the proposed Hankel transform method (blue).

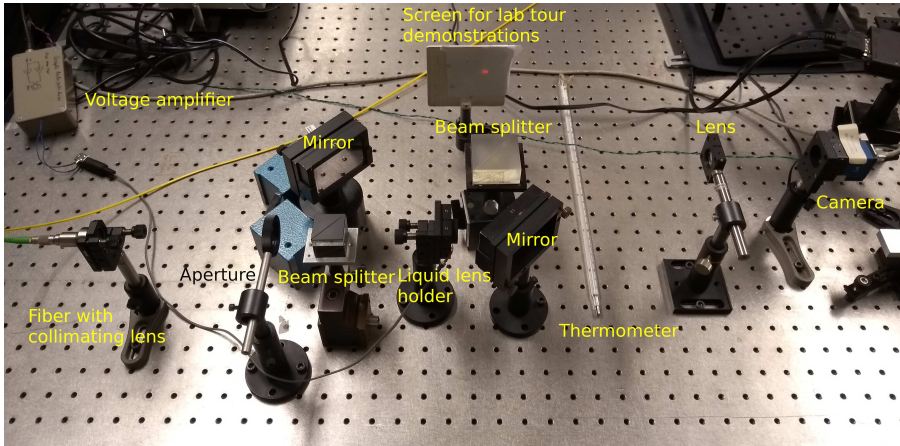


Figure 5.5.: Photo of the liquid lens in a Mach-Zehnder interferometer

39 V to 58 V during standard operation. A flat surface is obtained by applying ± 45 V. The lens makes use of AC electrowetting, therefore all input voltages are modulated with a square wave at 1136 Hz as displayed in Figure 4.5. At the wavelength 632.8 nm, the refractive indices of the two used liquids are $n_1 = 1.3846$ and $n_2 = 1.4921$. The root-mean-squared (RMS) wavefront error⁴⁹ is $WFE_{\text{RMS}} = 50$ nm (i.e. $WFE_{\text{RMS}}/(n_2 - n_1) = 0.5 \mu\text{m}$ RMS surface error). In Section 4.6 we determined the speed of capillary waves on the LL: $c = 26$ cm/s. Even though the focal length as function of the applied voltage of the newer LL differs from the previous one, the resonance properties were by testing found to be identical. The measurement temperature for the shown experiments is $T = 25^\circ\text{C}$. The radius of a flat LL interface is $R = 2.65$ mm.

A HeNe laser beam is collimated and sent through a Mach-Zehnder interferometer (Fig. 5.6). The light passing through the liquid lens interferes with the reference and is measured with a camera. A lens is used behind the Mach-Zehnder interferometer to image the optical phase shift introduced by the LL surface onto the camera. The Mach-Zehnder interferometer was built and analysed with the help of Peter A. A. M. Somers.

The camera is a SVS-VISTEK eco424MVGE with an adjustable frame rate (1-124 Hz) and integration time ($3 \mu\text{s}$ -1 s) as listed in Table 4.1. All images and videos⁵⁰ are made using an external trigger to synchronise the camera to the LL surface movement. The videos are in consequence not showing a high-speed image of a single lens surface oscillation but are recorded over many oscillation periods. The calculated voltage signal is sent via a NI-9263 D/A converter from the computer to a voltage amplifier ($8\times$) and then applied to the LL electrodes. More information about the amplifier and the generation of the voltage actuation

⁴⁹The root-mean-squared error is the common term for describing the quality of optical surfaces and used interchangeably with the standard deviation throughout this thesis.

⁵⁰The videos are part of the publication in AIP Advances and available online [202].

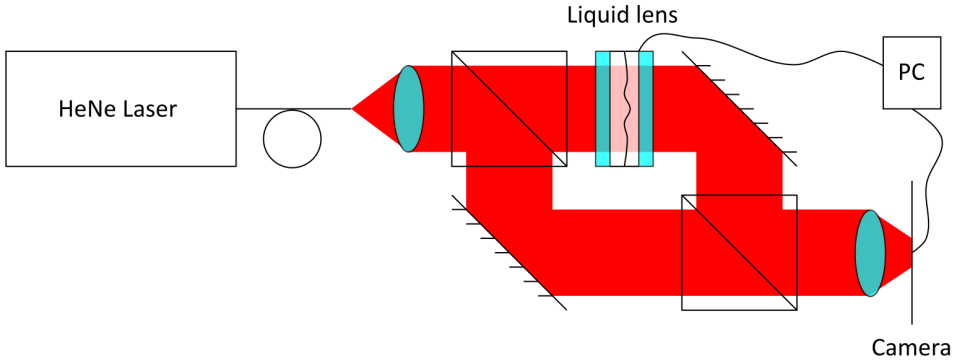


Figure 5.6.: The liquid lens surface is measured in a Mach-Zehnder interferometer. The phase change due to the liquid lens is imaged onto the camera with an additional lens.

and trigger signals can be found in Appendix B.

For the analysis of the interferogram, it is not relevant to know the exact initial phase or amplitude profile of the incident laser. When the test and the reference waves interfere, the phase difference $\Delta\phi$ can be obtained from the intensity pattern

$$I_{\text{tot}}(\mathbf{x}) = I_1(\mathbf{x}) + I_2(\mathbf{x}) + 2\sqrt{I_1(\mathbf{x})I_2(\mathbf{x})} \cos \Delta\phi(\mathbf{x}). \quad (5.25)$$

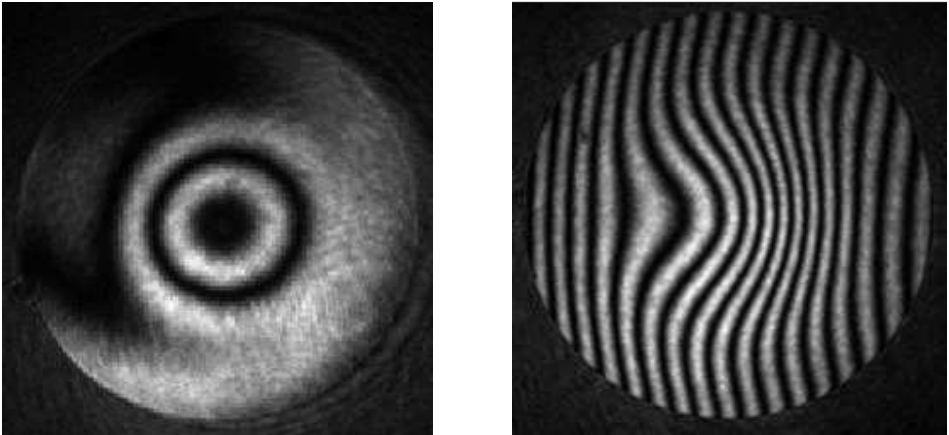


Figure 5.7.: Interference pattern of a Bessel phase shift in the test wavefront with an almost parallel (left) and a tilted (right) reference wavefront.

For two identical waves interfering the resulting intensity is constant over the full interferogram. If one of the waves is deformed, the intensity will vary locally and allows determining the phase. However the inverse of the cosine is limited to phases between 0 and π and therefore not represent significant phase changes.

The resulting phase is also continuous, so it cannot be unwrapped using the fact that the surface is a continuous function of position. Additionally the analysis is disturbed by stray light caught by the detector and the detector noise. These problems can be circumvented by intentionally tilting the reference with respect to the wavefront that is tested [219]. Figure 5.7 displays two interferograms for a parallel and a tilted reference wavefront interfering with the same phase shift in the test beam.

The interference of two tilted identical wavefronts creates a linear fringe pattern, that can be expressed by introducing a carrier frequency vector \mathbf{f}_c pointing in the direction of the tilt to Equation (5.25)

$$I_{\text{tot}}(\mathbf{x}) = I_1(\mathbf{x}) + I_2(\mathbf{x}) + 2\sqrt{I_1(\mathbf{x})I_2(\mathbf{x})} \cos(2\pi\mathbf{f}_c\mathbf{x} + \Delta\phi(\mathbf{x})) \quad (5.26)$$

$$= I_1(\mathbf{x}) + I_2(\mathbf{x}) + I_{\text{mix}}(\mathbf{x})e^{i2\pi\mathbf{f}_c\cdot\mathbf{x}} + I_{\text{mix}}^*(\mathbf{x})e^{-i2\pi\mathbf{f}_c\cdot\mathbf{x}}. \quad (5.27)$$

with $I_{\text{mix}}(\mathbf{x}) = \sqrt{I_1(\mathbf{x})I_2(\mathbf{x})} \exp(i\Delta\phi(\mathbf{x}))$. If the spatial phase variation $\Delta\phi$ is slow compared to the introduced phase tilt, the Fourier transform of both components separate in Fourier space by the carrier frequency

$$\hat{I}_{\text{tot}}(\mathbf{f}) = \hat{I}_1(\mathbf{f}) + \hat{I}_2(\mathbf{f}) + \hat{I}_{\text{mix}}(\mathbf{f} + \mathbf{f}_c) + \hat{I}_{\text{mix}}^*(\mathbf{f} - \mathbf{f}_c). \quad (5.28)$$

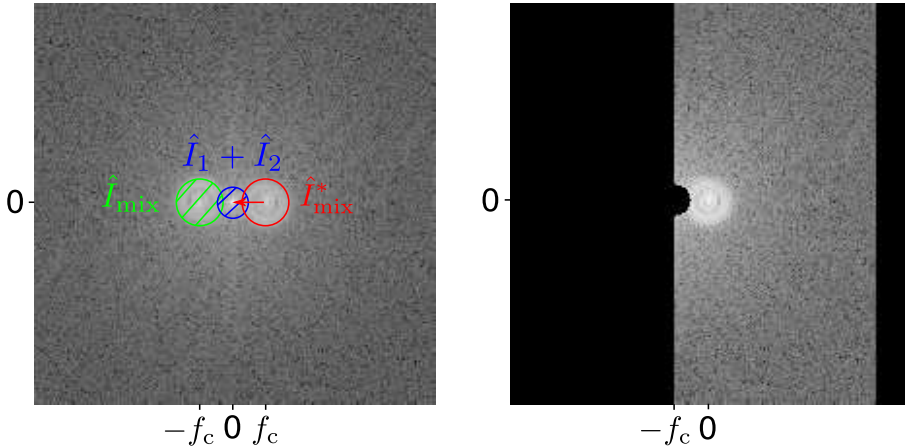


Figure 5.8.: Plot of the logarithm of the modulus of the Fourier transform: $\ln(|\hat{I}_{\text{tot}}|)$ of the right interferogram in Fig. 5.7. The first plot shows the separated components of \hat{I}_{tot} and the second plot the shifted result \hat{I}'_{mix} after removing the background.

The separation in frequency space offers the possibility to filter out the unwanted background noise $\hat{I}_1 + \hat{I}_2$ around the origin and to retrieve the phase information around \mathbf{f}_c . Either of the two phase profiles \hat{I}_{mix} is translated to the origin, while the other one is set to 0 to obtain the phase information $\hat{I}'_{\text{mix}}(\mathbf{f})$. Figure 5.8 shows the separation in Fourier space, how to remove the background, and how to

shift the relevant information to the origin. An inverse Fourier transform yields $I'_{\text{mix}}(\mathbf{x})$ and taking the logarithm isolates the phase information completely from the amplitude in the imaginary part:

$$\ln(I'_{\text{mix}}(\mathbf{x})) = \ln\left(\sqrt{I_1(\mathbf{x})I_2(\mathbf{x})}\right) + i\Delta\phi(\mathbf{x}). \quad (5.29)$$

The resulting phase information is wrapped onto the interval $]-\pi, \pi]$. Although this information is sufficient for most calculations, the wrapped phase does not represent the real phase object or in our case the continuous LL surface. There are several techniques to unwrap the phase available that are all based on the assumption that the phase varies slowly between neighbouring pixels [220]. The difference of nearest neighbour pixels is then compared to a threshold value, i.e. 1.8π . If the phase difference is larger than the threshold, a phase jump is detected and a phase offset of $\phi_o = \pm 2\pi$ is added to the phase difference to obtain a continuous phase profile

$$\phi_c(\mathbf{x}) = \Delta\phi(\mathbf{x}) + \phi_o(\mathbf{x}). \quad (5.30)$$

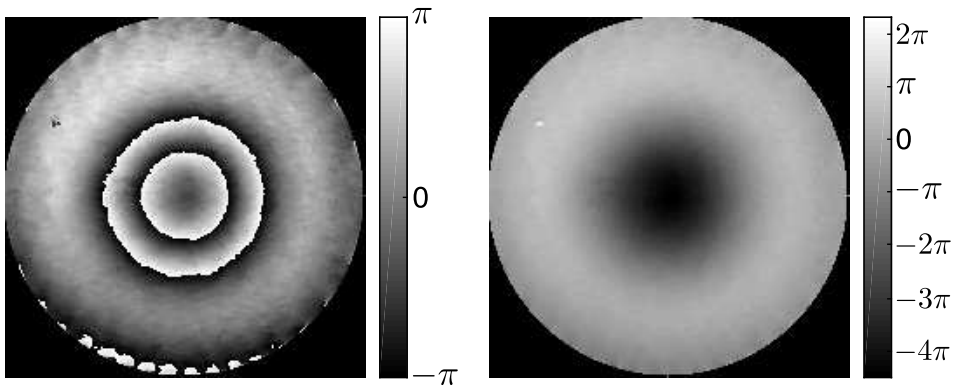


Figure 5.9.: Phase shift of the right interferogram in Fig. 5.7 before (left) and after phase unwrapping (right).

A comparison between a wrapped and an unwrapped phase profile is shown in Figure 5.9. The interferograms are analysed in Matlab. The exact procedure is explained in Appendix C.

5.5. Construction of arbitrary aspheres

The presence of Bessel-shaped modes as predicted by the analytical model in Section 4.2 can be additionally confirmed with the interferometric surface measurement. As in the experiment in Section 4.6, a cosine voltage with an amplitude of 1.6 V and a frequency of $f_1 = 59$ Hz is applied to the liquid lens to reproduce the first resonant Bessel mode $u = \cos(2\pi f_1 t)J_0(j_{1,1}r/R)$. Figure 5.10 (a) shows the measured surface profile along the y -axis of the camera sensor in an instant of time

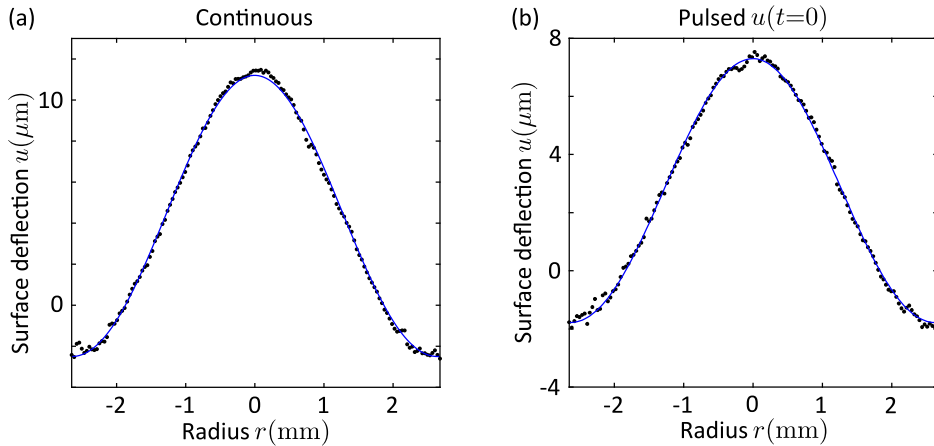


Figure 5.10.: The Bessel function created in two different ways: (a) by a continuous 59 Hz cosine actuation signal and (b) by a pulsed signal as shown in Fig. 5.3 (black dots). The theoretical prediction is plotted in blue.

where the deflection is maximum. The measured surface shape agrees with the model (see Eq. (5.7)) and thereby confirms the results of the previous chapter with another type of measurement. The RMS wavefront error $WFE_{RMS} = 0.02 \mu\text{m}$ is smaller than the one given by the LL manufacturer. The RMS wavefront error of $0.01 - 0.02 \mu\text{m}$ can be observed in all measurements, even without the LL, and is therefore associated with the Mach-Zehnder interferometer.

The movement of the liquid lens surface is not entirely symmetric, when applying a cosine voltage as can be observed in Figure 5.11. The behaviour of the surface changes slightly with the polarity. This asymmetry has been described recently [221] and can be explained by the theory of charge restraint. Negative ions are restrained, i.e. held back, more easily by the dielectric during the oscillation and therefore prevent the formation of a flat surface when the voltage is decreasing. This behaviour can best be observed in a video that has been published [online](#) [202]. The video of the surface oscillation is taken with time steps of $292 \mu\text{s}/\text{frame}$ and the exposure time is $80 \mu\text{s}$.

The same surface shape can be created using the proposed algorithm (Sec. 5.3) as shown in Figure 5.10 (b). A pulse is calculated for the first Bessel mode on the liquid lens as shown in Figure 5.3. The pulse is repeated with a frequency of 10 Hz. The Bessel function is created with the same quality ($WFE_{RMS} = 14 \text{ nm}$) as with the continuous sinusoidal actuation voltage. However, the surface profile looks very different at all other times than $t = 0$. There is a video available [online](#), too [202]. It shows the pulse in time steps of $62.5 \mu\text{s}/\text{frame}$ and the exposure time is $20 \mu\text{s}$.

Creating a Zernike function as surface deformation that can be added to the spherical surface of the LL is a possible application of the technique. Zernike polynomials are an orthogonal basis on the unit circle and describe optical aber-

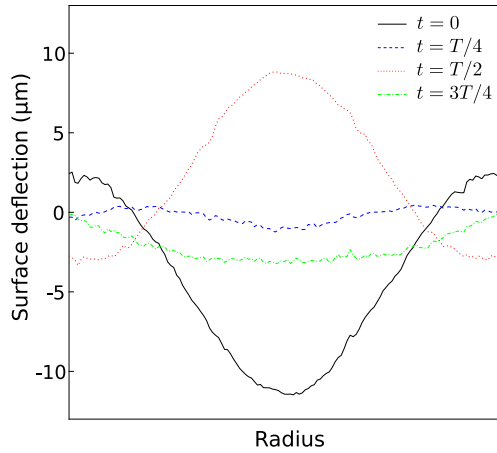


Figure 5.11.: A continuously driven liquid lens surface by which a Bessel function shape as in Fig. 5.10 (a) is created at four instances of time during one period T . The movement of the lens surface is not entirely symmetric due to charge trapping in the electrical insulator as can be seen by comparing the shape at $t = T/4$ and $t = 3T/4$. While the surface becomes almost flat moving upwards, it stays curved during the downwards movement.

ration. Introducing phase delays with the shape of Zernike polynomials and their superposition is therefore commonly used in adaptive optics and optical design to achieve a better imaging performance. Figure 5.12 displays an overview of Zernike functions. Hankel transforms of Zernike functions are (related to) Bessel functions:

$$\mathcal{H}_m[R_n^m(r)](k) = (-1)^{\frac{n-m}{2}} J_{n+1}(k), \quad (5.31)$$

with $R_m^n(r)$ being the radial Zernike polynomials and $\mathcal{H}_m(k)$ the Hankel transform of order m and for even $n - m \geq 0$ [222].

Electrowetting liquid lenses are built to create defocus Z_2^0 by shaping the surface in the form of the Zernike polynomial. Some of the more recent lenses use multiple electrodes oriented radially around the lens to create tilt Z_1^1, Z_1^{-1} , astigmatism Z_2^2, Z_2^{-2} or trefoil Z_3^3, Z_3^{-3} . All modes on the left and right edges of the displayed triangle can be created with multiple electrodes and DC voltages. The used Arctic 39N0 LL however can only create defocus statically. With the proposed algorithm it should be possible to create all circularly symmetric Zernike modes like spherical aberration Z_4^0 temporarily (vertical symmetry axis of the triangle in Figure 5.12). All other aberrations that are not on the edge or the symmetry axis can be realised by combining both techniques. An actuation voltage pulse has to be calculated for each electrode in a multi-electrode LL.

The actuation signal to create the primary spherical aberration Z_4^0 at a given instant of time on the LL can be calculated in the same way as in the case of the Bessel surface shape. Figure 5.13 shows the result of the algorithm and shows a

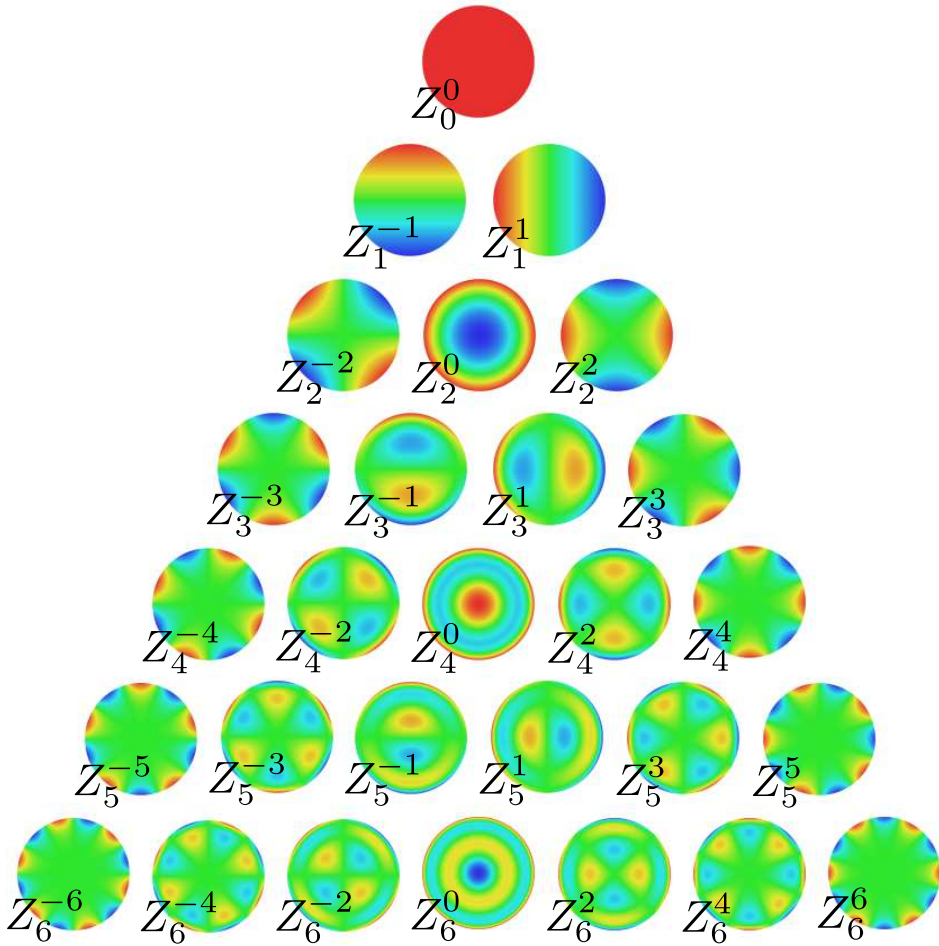


Figure 5.12.: Zernike functions on the unit circle. The surfaces on the left and right edge of the triangle can be created by liquid lenses with multiple electrodes. The ones on the vertical symmetry axis can be realised with the proposed technique. All others can be created by combing the proposed technique with multiple electrodes.

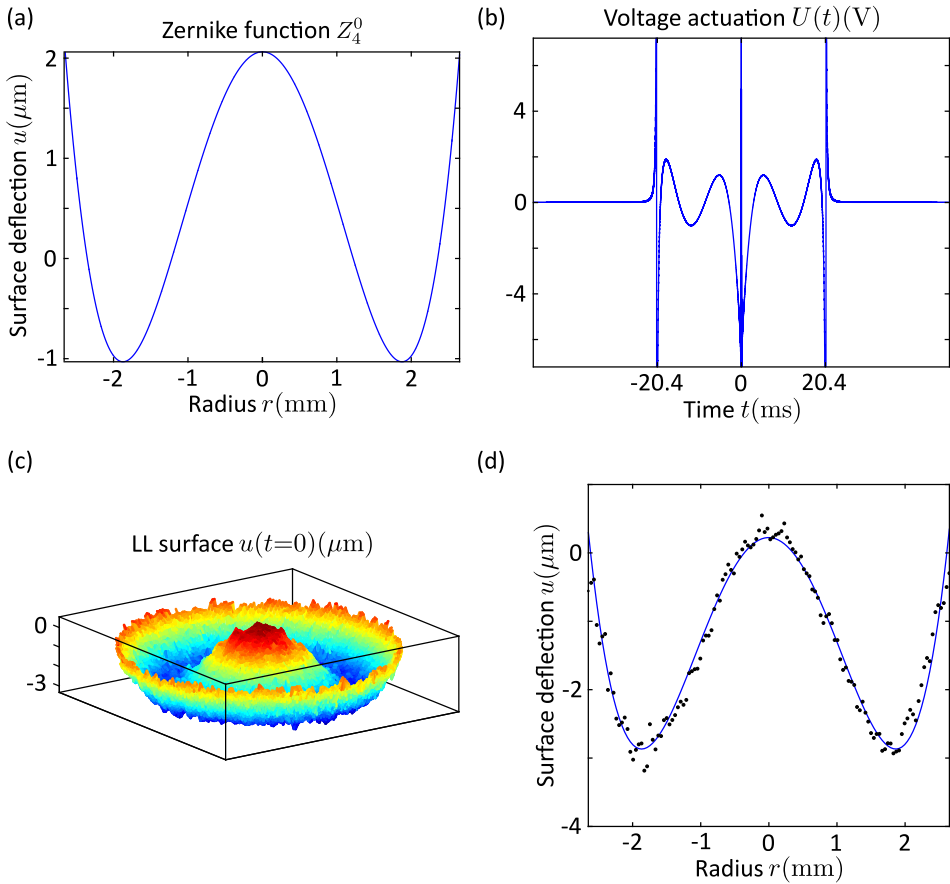


Figure 5.13.: (a) The primary spherical aberration is transformed into a voltage actuation signal (b). The surface measurement is displayed in (c) and the measured and computed surface profiles at the time $t = 0$ are shown in (d).

comparison of the measured and the computed surface at time $t = 0$. The peak to valley deflection of the surface is $3 \mu\text{m}$, which resembles an optical phase difference of π . The change in phase can be chosen to be smaller than 2π as well as larger than the wavelength by changing the amplitude of the actuation voltage. The smallest phase change tested successfully is 0.16π . The absolute deviation from the desired surface is similar to the previous examples $\text{WFE}_{\text{RMS}} = 0.02 \mu\text{m}$.

The applicability of the technique however is limited to simple shapes. Surface shapes with higher spatial frequency content are more difficult to create. Creating an axicon is for example still possible with good accuracy using the linear dispersion model, but a top hat structure cannot be created. Figure 5.14 (a) shows the measured surface shape of an axicon. While the slopes of the axicon are nicely mimicked ($\text{WFE}_{\text{RMS}} = 0.02 \mu\text{m}$), the tip of the axicon appears slightly rounded and loses its sharpness for higher amplitude signals. The quality of the conical shape is surprisingly good since the formation of a sharp tip requires high spatial frequency information as can be seen by the actuation pulse and its Fourier transform in Figure 5.15.

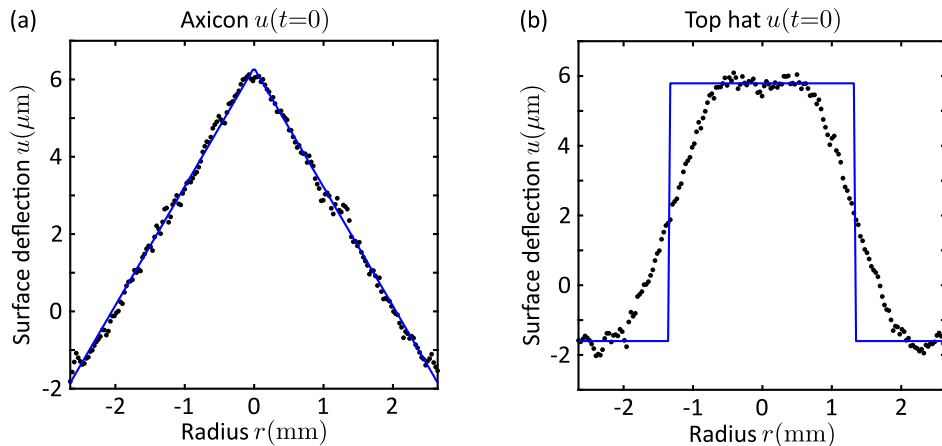


Figure 5.14.: Measured (black dots) and computed surface shape at time $t = 0$ for an axicon (a) and a top hat (b). The surfaces were realized with a computed actuation voltage pulse.

The top hat structure is displayed in Figure 5.14 (b). Figure 5.15 shows, that the high frequency content of the top hat actuation signal is obviously much higher than for the axicon. The slopes of the top hat are too steep to be fully described by the simple membrane-based model. The measured surface slope is $6 \mu\text{m}/\text{mm}$ which equals an optical path length difference of one optical wavelength per millimetre for a HeNe laser. The slope limitation is not constant over the lens diameter. It is proportional to the envelope of the Bessel functions ($\partial u/\partial r \sim \sqrt{2/(\pi r)}$ for large radii [212]). Large slopes close to the centre of the lens need high actuation frequencies, because the first derivative of the Bessel function $J_1(r=0)$ is 0 at the centre of the lens. The slope increases only slowly with increasing fre-

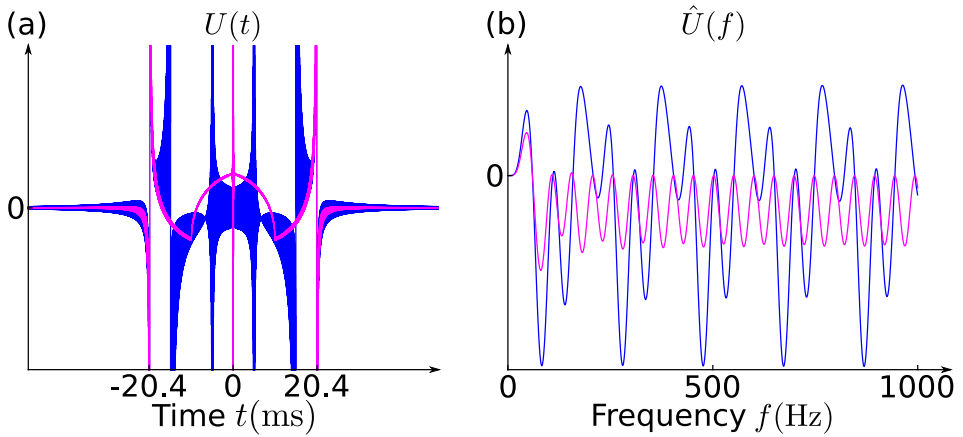


Figure 5.15.: Comparison of the actuation pulses (a) and their Fourier spectra (b) for creating the axicon (magenta) and the top hat (blue) of Fig. 5.14. The thick blue lines origin from very high frequency oscillations in the voltage actuation signal.

quency in the vicinity of the centre. Everywhere else, larger slopes require larger actuation voltages in the input signal because the envelope of the Bessel function $\sqrt{2/(\pi r)}$ decreases with the radius and thus the surface will be affected more by non-linearities. A description of the surface vibration, that takes account of the non-linear dispersion of capillary waves, the exact lens geometry, and the viscosity is expected to improve the creation of high-frequency surface shapes.

The presented results are highly repeatable. A difference in the resulting wavefront exceeding the 50 nm RMS wavefront error has never been found, when measuring the surface shape of the LL for a specific actuation signal over several days in a row, nor when repeating the same experiment after 109 days⁵¹.

The radius of the LL is directly responsible for the calculated pulse lengths $\Delta t = 4R/c$ and therefore imposes a limit on the maximum repetition rate of the desired liquid lens surfaces. To increase the repetition rate, the pulse can be shortened to half its length by setting the actuation voltage to zero for $t > 0$.

5.6. Summary

A new way to create instantaneous aspheric surfaces on a liquid lens has been demonstrated. With the proposed Hankel transform method voltage actuation signals can be computed with which basically any surface shape on the LL can be realised at a given time. However, friction and the viscosity of the liquid limit the applicability of the undamped model to surface deviations in the range of a few optical path lengths. The underlying simplification of a linear surface wave

⁵¹Only very low sub-Hz frequencies that change the polarity of the insulating liquid have to be avoided.

dispersion further limits the shapes to low spatial frequencies. The duration of the actuation voltage pulse depends on the speed of the waves on the surface and scales with the the radius of the lens. The creation of a Bessel function, the primary spherical aberration Zernike polynomial, and an axicon have been demonstrated successfully. Creating a top hat structure however failed due to the simplicity of the underlying liquid model but could be improved by considering a more thorough liquid dispersion model.

6. Conclusion

Designing and building a multispectral camera for the age determination of bruises has been a success. Although the focus of designing a camera system shifted to designing a spectral Fabry-Pérot filter at early stage of the project all main goals have been achieved. The detailed investigation of the Fabry-Pérot interferometer led to new insights into the interaction between plane or spherical waves with a Fabry-Pérot filter. The results can be used to find the best design for placing a Fabry-Pérot interferometer in a lens system, balancing spectral resolution, numerical aperture, and manufacturing tolerances. The spectral resolution of an optical system, that is telecentric on the image side where the Fabry-Pérot interferometer is placed in the image space, is limited by the numerical aperture $\delta\lambda \leq (1 - \sqrt{1 - (\text{NA}_i/n)^2})\lambda_0$. The developed Fabry-Pérot interferometer itself has a unique design that can scan the wavelength by changing the distance between two high-quality large-surface mirrors. The device, available for purchase, contains a Fabry-Pérot filter only a few centimetres in size and is now applied at the Amsterdam Universitair Medische Centra to measure the ageing behaviour of bruises. The camera thereby contributes to the development of a cost-efficient device for residents to detect child abuse at an early stage.

The search for alternative spectral filters to create a new type of spectral camera uncovered a new technique to create tunable optic surfaces with a liquid lens. While studying electrowetting liquid lenses, we found that surface waves on the liquid produced by fast focal switching follow a reproducible pattern. The further study of the surface waves uncovered that for small surface waves the liquid surface can be described as a vibrating membrane with slip wall boundary conditions. The surface waves take the shape of Bessel functions and are resonant at distinct frequencies, that can be calculated if the speed of capillary waves on the surface of the liquid lens is known. The Bessel surface functions form a complete orthogonal basis function for circular symmetric surfaces. In consequence, we investigated how to design new surface shapes on the liquid lens at a given instant of time by linear combination of Bessel surface waves. Using a Hankel transform, it is possible to calculate the actuation signal of a liquid lens to create a variety of new surface shapes. Within the limits of small surface waves, it is possible to create Bessel surfaces, the Zernike polynomial corresponding to spherical aberration, and for the first time a tunable axicon with a liquid lens. The new technique to create aspheres on a liquid lens can be implemented immediately by liquid lens users worldwide, since there is no additional hardware required to apply the technique.

The scientific discoveries of this thesis have been published in three scientific journals and in an interview in the faculty newspaper and have been presented on 14 scientific conferences.

Bibliography

- [1] Clarivate Analytics, “Web of science [v.5.30] - web of science core collection result analysis.”
<http://www.webofscience.com>, 2018.
- [2] M. P. Thomas Jr., “Child abuse and neglect part I – historical overview, legal matrix, and social perspectives,” *N.C. L. Rev.*, vol. 50, pp. 293–349, 1972.
- [3] J. H. Beitchman, K. J. Zucker, J. E. Hood, G. A. daCosta, D. Akman, and E. Cassavia, “A review of the long-term effects of child sexual abuse,” *Child Abuse & Neglect*, vol. 16, no. 1, pp. 101–118, 1992.
- [4] B. Stam, *Three dimensional modeling of bruise evolution for improved age determination*. PhD thesis, Faculty of Medicine, University of Amsterdam, 2012.
- [5] A. Kübelbeck, “Black eye 01.jpg.” CC-BY-SA (<https://creativecommons.org/licenses/by-sa/3.0/>),
https://commons.wikimedia.org/wiki/File:Black_Eye_01.jpg, 2011.
- [6] L. L. Randeberg, B. Skallerud, N. E. I. Langlois, O. A. Haugen, and L. O. Svaasand, “The optics of bruising,” in *Optical-Thermal Response of Laser-Irradiated Tissue* (A. J. Welch and M. J. van Gemert, eds.), ch. The Optics of Bruising, pp. 825–858, Dordrecht: Springer, 2nd ed., 2011.
- [7] T. Stephenson and Y. Bialas, “Estimation of the age of bruising,” *Archives of Disease in Childhood*, vol. 74, no. 1, pp. 53–55, 1996.
- [8] L. L. Randeberg, I. Baarstad, T. Løke, P. Kaspersen, and L. O. Svaasand, “Hyperspectral imaging of bruised skin,” in *Proc. SPIE*, vol. 6078, p. 60780O, 2006.
- [9] B. Stam, M. J. Gemert, T. G. Leeuwen, and M. C. Aalders, “3D finite compartment modeling of formation and healing of bruises may identify methods for age determination of bruises,” *Medical & Biological Engineering & Computing*, vol. 48, no. 9, pp. 911–921, 2010.
- [10] H. Darcy, *Les fontaines publiques de la ville de Dijon*. Paris: Victor Dalmont, 1856.
- [11] A. Fick, “Über Diffusion,” *Ann. Phys.*, vol. 170, no. 1, pp. 59–86, 1855.

- [12] A. Fick, "On liquid diffusion," *J. Membr. Sci.*, vol. 100, no. 1, pp. 33–38, 1995.
- [13] M. C. G. Aalders, N. Van Der Vange, W. M. Star, and H. J. C. M. Sterenborg, "A mathematical evaluation of dose-dependent PpIX fluorescence kinetics in vivo," *Photochem. Photobiol.*, vol. 74, no. 2, pp. 311–317, 2001.
- [14] R. J. M. Hoveling, "The spectr@phone - age determination of bruises," in *Symposium Fotonica*, 2013.
- [15] B. Stam, M. J. C. van Gemert, T. G. van Leeuwen, A. H. Teeuw, A. C. van der Wal, and M. C. G. Aalders, "Can color inhomogeneity of bruises be used to establish their age?," *J. Biophotonics*, vol. 4, no. 10, pp. 759–767, 2011.
- [16] Y. Garini, I. T. Young, and G. McNamara, "Spectral imaging: Principles and applications," *Cytometry Part A*, vol. 69A, no. 8, pp. 735–747, 2006.
- [17] N. Hagen and M. W. Kudenov, "Review of snapshot spectral imaging technologies," *Opt. Eng.*, vol. 52, no. 9, p. 090901, 2013.
- [18] E. Herrala, J. T. Okkonen, T. S. Hyvarinen, M. Aikio, and J. Lammasniemi, "Imaging spectrometer for process industry applications," in *Proc. SPIE*, vol. 2248, pp. 33–40, 1994.
- [19] T. Wu, L. Zhang, Y. Cen, C. Huang, X. Sun, H. Zhao, and Q. Tong, "Polarized spectral measurement and analysis of sedum spectabile boreau using a field imaging spectrometer system," *IEEE Journal of Selected Topics in Applied Earth Observations and Remote Sensing*, vol. 6, no. 2, pp. 724–730, 2013.
- [20] R. O. Green, M. L. Eastwood, C. M. Sarture, T. G. Chrien, M. Aronsson, B. J. Chippendale, J. A. Faust, B. E. Pavri, C. J. Chovit, M. Solis, M. R. Olah, and O. Williams, "Imaging spectroscopy and the airborne visible/infrared imaging spectrometer (AVIRIS)," *Remote Sens. Environ.*, vol. 65, no. 3, pp. 227–248, 1998.
- [21] M. E. Dickinson, G. Bearman, S. Tille, R. Lansford, and S. E. Fraser, "Multi-spectral imaging and linear unmixing add a whole new dimension to laser scanning fluorescence microscopy," *BioTechniques*, vol. 31, no. 6, pp. 1272–1278, 2001.
- [22] B. Khoobehi, J. M. Beach, and H. Kawano, "Hyperspectral imaging for measurement of oxygen saturation in the optic nerve head," *Investigative Ophthalmology & Visual Science*, vol. 45, no. 5, pp. 1464–1472, 2004.
- [23] W. Cai, R. Ning, and J. Liu, "Feasibility study of spectral imaging for differential phase contrast cone beam CT: computer simulations," in *Proc. SPIE*, vol. 8668, p. 86684Z, 2013.

-
- [24] A. Pelagotti, P. Ferrara, L. Pescitelli, C. Delfino, G. Gerlini, A. Piva, and L. Borgognoni, “Multispectral imaging for early diagnosis of melanoma,” in *Proc. SPIE*, vol. 8668, p. 86684A, 2013.
- [25] C. Fabry and A. Pérot, “Sur les franges des lames minces argentées et leur application à la mesure de petites épaisseurs d’air,” *Ann. Chim. Phys.*, vol. 12, no. 459–501, 1897.
- [26] G. Courtès, “Méthodes d’observation et étude de l’hydrogène interstellaire en émission,” *Annales d’Astrophysique*, vol. 23, pp. 115–156, 1960.
- [27] P. D. Atherton, N. K. Reay, J. Ring, and T. R. Hicks, “Tunable Fabry-Perot filters,” *Opt. Eng.*, vol. 20, no. 6, pp. 806–814, 1981.
- [28] J. Bland-Hawthorn and D. H. Jones, “TTF: a flexible approach to narrow-band imaging,” in *Proc. SPIE*, vol. 3355, pp. 855–865, SPIE, 1998.
- [29] T. J. Kentischer, W. Schmidt, M. Sigwarth, and M. von Uexküll, “TESOS, a double Fabry-Perot instrument for solar spectroscopy,” *Astron. Astrophys.*, vol. 340, pp. 569–578, 1998.
- [30] D. H. Jones, P. L. Shopbell, and J. Bland-Hawthorn, “Detection and measurement from narrow-band tunable filter scans,” *Mon. Not. R. Astron. Soc.*, vol. 329, no. 4, pp. 759–774, 2002.
- [31] J. H. Correia, M. Bartek, and R. F. Wolffenbuttel, “Bulk-micromachined tunable Fabry-Perot microinterferometer for the visible spectral range,” *Sens. Actuators, A*, vol. 76, no. 1-3, pp. 191–196, 1999.
- [32] J. H. Jerman and D. J. Clift, “Miniature Fabry-Perot interferometers micromachined in silicon for use in optical fiber WDM systems,” in *TRANSDUCERS ’91: 1991 International Conference on Solid-State Sensors and Actuators. Digest of Technical Papers*, pp. 372–375, 1991.
- [33] J. Antila, R. Mannila, U. Kantojärvi, C. Holmlund, A. Rissanen, I. Näkki, J. Ollila, and H. Saari, “Spectral imaging device based on a tuneable MEMS Fabry-Perot interferometer,” in *Proc. SPIE*, vol. 8374, p. 83740F, 2012.
- [34] J. Antila, J. Mäkynen, A. Rissanen, A. Näsälä, M. Kaarre, and H. Saari, “Fabry-Perot interferometer spectral engines for imaging hyperspectral,” in *Imaging and Applied Optics*, p. AM1B.5, 2013.
- [35] A. K. Jain, W. W. Durand, G. R. Knowles, J. G. Droessler, and M. J. Lavan, “Dual tunable Fabry-Perot: A new concept for spectrally agile filtering,” in *Imaging Spectroscopy I*, vol. 0268, pp. 183–189, 1981.
- [36] S. Poger and E. Angelopoulou, “Multispectral sensors in computer vision,” in *Stevens Institute of Technology, CS Report 2001-3*, 2001.
- [37] W. Gunning, J. Pasko, and J. Tracy, “A liquid crystal tunable spectral filter: Visible and infrared operation,” in *Imaging Spectroscopy I*, vol. 0268, pp. 190–194, 1981.

- [38] P. Jacquinot, “The luminosity of spectrometers with prisms, gratings, or Fabry-Perot etalons,” *J. Opt. Soc. Am.*, vol. 44, no. 10, pp. 761–765, 1954.
- [39] B. Lyot, “Le filtre monochromatique polarisant et ses applications en physique solaire,” *Annales d’Astrophysique*, vol. 7, p. 31, 1944.
- [40] P. Yeh and J. Tracy, “Theory of dispersive birefringent filters,” in *Imaging Spectroscopy I*, vol. 0268, pp. 171–177, 1981.
- [41] A. M. Title and W. J. Rosenberg, “Spectral management,” in *Imaging Spectroscopy I*, vol. 0268, pp. 178–182, 1981.
- [42] P. J. Miller, “Use of tunable liquid crystal filters to link radiometric and photometric standards,” *Metrologia*, vol. 28, no. 3, pp. 145–149, 1991.
- [43] H. R. Morris, C. C. Hoyt, and P. J. Treado, “Imaging spectrometers for fluorescence and raman microscopy: Acousto-optic and liquid crystal tunable filters,” *Appl. Spectrosc.*, vol. 48, no. 7, pp. 857–866, 1994.
- [44] N. Gat, “Imaging spectroscopy using tunable filters: a review,” in *Wavelet Applications VII*, vol. 4056, pp. 50–64, 2000.
- [45] S. E. Harris and R. W. Wallace, “Acousto-optic tunable filter,” *J. Opt. Soc. Am.*, vol. 59, no. 6, pp. 744–747, 1969.
- [46] K. B. Steinbruegge, M. Gottlieb, and J. D. Feichtner, “Automated acousto-optic tunable filter (AOTF) infrared analyzer,” in *Imaging Spectroscopy I*, vol. 0268, pp. 160–166, 1981.
- [47] L. J. Denes, M. S. Gottlieb, and B. Kaminsky, “Acousto-optic tunable filters in imaging applications,” *Opt. Eng.*, vol. 37, no. 4, pp. 1262–1267, 1998.
- [48] N. Gupta, “Hyperspectral imager development at army research laboratory,” in *Infrared Technology and Applications XXXIV*, vol. 6940, pp. 573–582, SPIE, 2008.
- [49] A. Machihin, V. Pozhar, and V. Batshev, “Compact AOTF-based spectral imaging system for medical endoscopic analysis,” *Photon Lasers Med*, vol. 2, no. 2, pp. 153–157, 2013.
- [50] I. S. Bowen, “The image-slicer a device for reducing loss of light at slit of stellar spectrograph,” *Astrophys. J.*, vol. 88, pp. 113–124, 1938.
- [51] J. M. Hill, J. R. P. Angel, J. S. Scott, D. Lindley, and P. Hintzen, “Multiple object spectroscopy - the medusa spectrograph,” *Astrophysical Journal Letters*, vol. 242, pp. L69–L72, 1980.
- [52] A. R. Harvey and D. W. Fletcher-Holmes, “High-throughput snapshot spectral imaging in two dimensions,” in *Proc. SPIE*, vol. 4959, pp. 46–54, 2003.

-
- [53] A. Garcia-Urbe, E. B. Smith, J. Zou, M. Duvic, V. Prieto, and L. V. Wang, “*In-vivo* characterization of optical properties of pigmented skin lesions including melanoma using oblique incidence diffuse reflectance spectrometry,” *J. Biomed. Opt.*, vol. 16, no. 2, p. 020501, 2011.
- [54] J. Stoffels, A. A. J. Bluekens, P. Jacobus, and M. Peters, “Color splitting prism assembly.” US4084180, 1978.
- [55] A. Hirai, T. Inoue, K. Itoh, and Y. Ichioka, “Application of measurement multiple-image Fourier of fast phenomena transform spectral imaging to measurement of fast phenomena,” *Opt. Rev.*, vol. 1, no. 2, pp. 205–207, 1994.
- [56] R. Shogenji, Y. Kitamura, K. Yamada, S. Miyatake, and J. Tanida, “Multispectral imaging using compact compound optics,” *Opt. Express*, vol. 12, no. 8, pp. 1643–1655, 2004.
- [57] Y. Murakami, M. Yamaguchi, and N. Ohyama, “Hybrid-resolution multispectral imaging using color filter array,” *Opt. Express*, vol. 20, no. 7, pp. 7173–7183, 2012.
- [58] L. Miao, H. Qi, and W. E. Snyder, “A generic method for generating multispectral filter arrays,” in *2004 International Conference on Image Processing, 2004. ICIP '04.*, vol. 5, pp. 3343–3346, 2004.
- [59] I. K. Baldry and J. Bland-Hawthorn, “A tunable echelle imager,” *Publ. Astron. Soc. Pac.*, vol. 112, no. 774, pp. 1112–1120, 2000.
- [60] T. Okamoto and I. Yamaguchi, “Simultaneous acquisition of spectral image information,” *Opt. Lett.*, vol. 16, no. 16, pp. 1277–1279, 1991.
- [61] F. V. Bulygin, G. N. Vishnyakov, G. G. Levin, and D. V. Karpukhin, “Spectrotomography—a new method of obtaining spectrograms of 2-D objects,” *Opt. Spectrosc.*, vol. 71, pp. 561–563, 1991.
- [62] M. Descour and E. Dereniak, “Computed-tomography imaging spectrometer: experimental calibration and reconstruction results,” *Appl. Opt.*, vol. 34, no. 22, pp. 4817–4826, 1995.
- [63] M. R. Descour, C. E. Volin, E. L. Dereniak, T. M. Gleeson, M. F. Hopkins, D. W. Wilson, and P. D. Maker, “Demonstration of a computed-tomography imaging spectrometer using a computer-generated hologram disperser,” *Appl. Opt.*, vol. 36, no. 16, pp. 3694–3698, 1997.
- [64] R. G. Baraniuk, “Compressive sensing [lecture notes],” *IEEE Signal Process. Mag.*, vol. 24, no. 4, pp. 118–121, 2007.
- [65] E. J. Candès, “Compressive sampling,” in *Proceedings of the International Congress of Mathematicians*, vol. 3, pp. 1433–1452, European Mathematical Society, 2006.

- [66] E. J. Candès and M. B. Wakin, “An introduction to compressive sampling,” *IEEE Signal Processing Magazine*, vol. 25, no. 2, pp. 21–30, 2008.
- [67] M. E. Gehm, R. John, D. J. Brady, R. M. Willett, and T. J. Schulz, “Single-shot compressive spectral imaging with a dual-disperser architecture,” *Opt. Express*, vol. 15, no. 21, pp. 14013–14027, 2007.
- [68] N. Hagen, R. T. Kester, L. Gao, and T. S. Tkaczyk, “Snapshot advantage: a review of the light collection improvement for parallel high-dimensional measurement systems,” *Opt. Eng.*, vol. 51, no. 11, p. 111702, 2012.
- [69] H. F. Rueda-Chacon, “Higher order discretization model for coded aperture spectral imaging systems,” Master’s thesis, University of Delaware, University of Delaware, Department of Electrical and Computer Engineering, 2015.
- [70] H. Arguello, C. V. Correa, and G. R. Arce, “Fast lapped block reconstructions in compressive spectral imaging,” *Appl. Opt.*, vol. 52, no. 10, pp. D32–D45, 2013.
- [71] H. Rueda, H. Arguello, and G. R. Arce, “Experimental demonstration of a colored coded aperture-based compressive spectral imaging system,” in *Classical Optics 2014*, p. CTu2C.6, OSA, 2014.
- [72] L. Galvis, H. Arguello, and G. R. Arce, “Coded aperture design in mismatched compressive spectral imaging,” *Appl. Opt.*, vol. 54, no. 33, pp. 9875–9882, 2015.
- [73] H. Rueda, H. Arguello, and G. R. Arce, “DMD-based implementation of patterned optical filter arrays for compressive spectral imaging,” *J. Opt. Soc. Am. A*, vol. 32, no. 1, pp. 80–89, 2015.
- [74] H. Rueda, H. Arguello, and G. R. Arce, “Compressive spectral testbed imaging system based on thin-film color-patterned filter arrays,” *Appl. Opt.*, vol. 55, no. 33, pp. 9584–9593, 2016.
- [75] C. F. Cull, K. Choi, D. J. Brady, and T. Oliver, “Identification of fluorescent beads using a coded aperture snapshot spectral imager,” *Appl. Opt.*, vol. 49, no. 10, pp. B59–B70, 2010.
- [76] A. Wagadarikar, R. John, R. Willett, and D. Brady, “Single disperser design for coded aperture snapshot spectral imaging,” *Appl. Opt.*, vol. 47, no. 10, pp. B44–B51, 2008.
- [77] L. Galvis-Carreno, *Coded Aperture Design in Compressive Spectral Imaging*. PhD thesis, University of Delaware, 2018.
- [78] C. Fu, *Compressive polar spectral and polarization imaging*. PhD thesis, 2018.
- [79] M. Karçaaltıncaba and A. R. Aktaş, “Dual-energy ct revisited with multidetector ct: review of principles and clinical applications,” *Diagn. Interv. Radiol.*, vol. 17, pp. 181–94, 2011.

-
- [80] X. Z. Lin, F. Miao, J. Y. Li, H. P. Dong, Y. Shen, and K. M. Chen, “High-definition CT gemstone spectral imaging of the brain,” *J. Comput. Assisted Tomogr.*, vol. 35, no. 2, pp. 294–297, 2011.
- [81] M. Diem, A. Mazur, K. Lenau, J. Schubert, B. Bird, M. Miljković, C. Krafft, and J. Popp, “Molecular pathology via IR and Raman spectral imaging,” *J. Biophotonics*, vol. 6, no. 11–12, pp. 855–886, 2013.
- [82] J.-I. Park, M.-H. Lee, M. D. Grossberg, and S. K. Nayar, “Multispectral imaging using multiplexed illumination,” in *2007 IEEE 11th International Conference on Computer Vision*, pp. 1–8, 2007.
- [83] A. Grewe, M. Hillenbrand, and S. Sinzinger, “Optimized Alvarez phase plates for hyperspectral imaging,” in *DGaO Proceedings*, 2013.
- [84] M. Hillenbrand, A. Grewe, and S. Sinzinger, “Parallelized chromatic confocal systems enable efficient spectral information coding,” *Iraqi Journal of Applied Physics*, vol. 9, pp. 3–4, Jan. 2013.
- [85] M. Hillenbrand, A. Grewe, M. Bichra, B. Mitschunas, R. Kirner, R. Weiß, and S. Sinzinger, “Chromatic information coding in optical systems for hyperspectral imaging and chromatic confocal sensing,” in *Proc. SPIE*, vol. 8550, p. 85500D, 2012.
- [86] E. Laux, C. Genet, T. Skauli, and T. W. Ebbesen, “Plasmonic photon sorters for spectral and polarimetric imaging,” *Nat. Photonics*, vol. 2, pp. 161–164, 2008.
- [87] G. Hennig, G. M. Brittenham, R. Sroka, G. Kniebühler, M. Vogeser, and H. Stepp, “Bandwidth-variable tunable optical filter unit for illumination and spectral imaging systems using thin-film optical band-pass filters,” *Rev. Sci. Instrum.*, vol. 84, no. 4, p. 043113, 2013.
- [88] P. F. Favreau, T. C. Rich, P. Prabhat, and S. J. Leavesley, “Tunable thin-film optical filters for hyperspectral microscopy,” in *Proc. SPIE*, vol. 8589, p. 85890R, 2013.
- [89] Z. Malik, D. Cabib, R. A. Buckwald, A. Talmi, Y. Garini, and S. G. Lipson, “Fourier transform multipixel spectroscopy for quantitative cytology,” *J. Microsc.*, vol. 182, no. 2, pp. 133–140, 1996.
- [90] E. Schröck, S. du Manoir, T. Veldman, B. Schoell, J. Wienberg, M. A. Ferguson-Smith, Y. Ning, D. H. Ledbetter, I. Bar-Am, D. Soenksen, Y. Garini, and T. Ried, “Multicolor spectral karyotyping of human chromosomes,” *Science*, vol. 273, no. 5274, pp. 494–497, 1996.
- [91] T. Zimmermann, J. Rietdorf, and R. Pepperkok, “Spectral imaging and its applications in live cell microscopy,” *FEBS Letters*, vol. 546, no. 1, pp. 87–92, 2003.

- [92] T. Zimmermann, J. Rietdorf, A. Girod, V. Georget, and R. Pepperkok, "Spectral imaging and linear un-mixing enables improved FRET efficiency with a novel GFP2–YFP FRET pair," *FEBS Letters*, vol. 531, no. 2, pp. 245–249, 2002.
- [93] H. Tsurui, H. Nishimura, S. Hattori, S. Hirose, K. Okumura, and T. Shirai, "Seven-color fluorescence imaging of tissue samples based on fourier spectroscopy and singular value decomposition," *Journal of Histochemistry & Cytochemistry*, vol. 48, no. 5, pp. 653–662, 2000.
- [94] M. W. Kudenov, M. E. L. Jungwirth, E. L. Dereniak, and G. R. Gerhart, "White-light sagnac interferometer for snapshot multispectral imaging," *Appl. Opt.*, vol. 49, no. 21, pp. 4067–4076, 2010.
- [95] M. W. Kudenov and E. L. Dereniak, "Compact snapshot birefringent imaging fourier transform spectrometer," in *Proc. SPIE*, vol. 7812, p. 781206, 2010.
- [96] Y. Xie, C. Zhou, W. Jia, J. Wang, and C. Xiang, "Sagnac spectral imaging resolved with two high-density gratings," in *Holography, Diffractive Optics, and Applications VIII*, vol. 10818, pp. 215–221, SPIE, 2018.
- [97] S. Tolansky, *An Introduction to Interferometry*. Longman Group Limited, 2 ed., 1955.
- [98] W. H. Steel, *Interferometry*. Cambridge University Press, 1967.
- [99] J. M. Vaughan, *The Fabry-Perot Interferometer – History, Theory, Practice and Applications*. Bristol: IOP Publishing, 1989.
- [100] G. Hernandez, *Fabry-Perot Interferometers*. Cambridge University Press, 1986.
- [101] M. N. Polyanskiy, "Refractive index database." <https://refractiveindex.info>. Accessed on 2018-11-18.
- [102] H. A. Macleod, *Thin-Film Optical Filters*. CRC Press, 4 ed., 2010.
- [103] O. El Gawhary, M. C. Dheur, S. F. Pereira, and J. J. M. Braat, "Extension of the classical Fabry–Perot formula to 1D multilayered structures," *Appl. Phys. B*, vol. 111, no. 4, pp. 637–645, 2013.
- [104] B. Edlén, "The refractive index of air," *Metrologia*, vol. 2, p. 71, apr 1966.
- [105] "Opto-mechatronics assemblies –." Anteryon B.V., <https://anteryon.com/products/spectrometer-assemblies-2/#1455193790377-6706b4ed-f692>. Accessed on 2018-11-24.
- [106] M. Strauch, I. L. Livshits, Y. Shao, F. Bociort, and H. P. Urbach, "Optical optimisation of Fabry-Pérot based spectral imaging systems," in *EOSAM 2014*, EOS, 2014.

-
- [107] R. C. Lyon, D. S. Lester, E. N. Lewis, E. Lee, L. X. Yu, E. H. Jefferson, and A. S. Hussain, "Near-infrared spectral imaging for quality assurance of pharmaceutical products: Analysis of tablets to assess powder blend homogeneity," *AAPS PharmSciTech*, vol. 3, no. 3, pp. 1–15, 2002.
- [108] Y. Xu, R. Xu, F. Li, and J. Wang, "Verification of programmable, large-FOV spectral imaging technology based on a staring/scanning area-array detector," in *Proc. SPIE*, vol. 9263, p. 92630I, 2014.
- [109] Z. Pan, G. Healey, M. Prasad, and B. Tromberg, "Face recognition in hyperspectral images," *IEEE Transactions on Pattern Analysis and Machine Intelligence*, vol. 25, no. 12, pp. 1552–1560, 2003.
- [110] H. Chang, A. Koschan, M. Abidi, S. G. Kong, and C.-H. Won, "Multispectral visible and infrared imaging for face recognition," in *2008 IEEE Computer Society Conference on Computer Vision and Pattern Recognition Workshops*, pp. 1–6, 2008.
- [111] P. J. Nystrom and L. K. Mestha, "Automatically focusing a spectral imaging system onto an object in a scene." US20140240511 A1, Aug. 2014.
- [112] C. Feng, X. Zhang, L. Shen, and S. Zhuo, "Multi-spectral imaging system for shadow detection and attenuation." US 20140240477, Aug. 2014.
- [113] H. Maeng, S. Liao, D. Kang, S.-W. Lee, and A. Jain, "Nighttime face recognition at long distance: Cross-distance and cross-spectral matching," in *Computer Vision – ACCV 2012*, vol. 7725 of *Lecture Notes in Computer Science*, pp. 708–721, Springer, 2013.
- [114] R. Stabbins, A. Griffiths, M. Gunn, and A. Coates, "Spectral imaging system simulation: Preparations for the ExoMars 2020 rover PanCam wide angle cameras," in *International Workshop on Instrumentation for Planetary Missions (IPM)*, 2018.
- [115] J. Praks, A. Kestilä, M. Hallikainen, H. Saari, J. Antila, P. Janhunen, and R. Vainio, "Aalto-1 - an experimental nanosatellite for hyperspectral remote sensing," in *2011 IEEE International Geoscience and Remote Sensing Symposium (IGARSS)*, pp. 4367–4370, 2011.
- [116] H. Saari, I. Pölönen, H. Salo, E. Honkavaara, T. Hakala, C. Holmlund, J. Mäkynen, R. Mannila, T. Antila, and A. Akujärvi, "Miniaturized hyperspectral imager calibration and UAV flight campaigns," in *Proc. SPIE*, vol. 8889, p. 88891O, 2013.
- [117] E. Honkavaara, J. Kaivosoja, J. Mäkynen, I. Pellikka, L. Pesonen, H. Saari, H. Salo, T. Hakala, L. Markelin, and T. Rosnell, "Hyperspectral reflectance signatures and point clouds for precision agriculture by light weight UAV imaging system," *ISPRS Annals of Photogrammetry, Remote Sensing and Spatial Information Sciences*, vol. I-7, pp. 353–358, 2012.

- [118] E. Hecht, *Optics*. San Francisco: Addison Wesley, 4 ed., 2002.
- [119] I. Livshits, Z. Hou, P. van Grol, Y. Shao, M. van Turnhout, P. Urbach, and F. Bociort, “Using saddle points for challenging optical design tasks,” in *Proc. SPIE*, vol. 9192, p. 919204, 2014.
- [120] Schott, *Schott N-BK 7 Data Sheet*, 2014.
- [121] Synopsys, *CODE V Systems Analysis Reference Manual 10.6*, Sept. 2013.
- [122] “Fabry-Perot spectrometers.” Rikola Ltd., Retrieved on 2014-12-4, http://www.rikola.fi/site/?page_id=46.
- [123] M. Reed, “Miniature spectral imaging camera.” Gooch & Housego, Retrieved on 2014-12-4, <http://goochandhousego.com/news/miniature-spectral-imaging-camera/>, 2014.
- [124] B. Schmitt, J. P. Borgogno, G. Albrand, and E. Pelletier, “*In situ* and air index measurements: influence of the deposition parameters on the shift of TiO₂/SiO₂ Fabry-Perot filters,” *Appl. Opt.*, vol. 25, no. 21, pp. 3909–3915, 1986.
- [125] D. C. Brown, “Decentering distortion of lenses,” *Photogrammetric Engineering*, vol. 32, no. 3, pp. 444–462, 1966.
- [126] T. Tsai, E. McLeod, and C. B. Arnold, “Generating Bessel beams with a tunable acoustic gradient index of refraction lens,” in *Optical Trapping and Optical Micromanipulation III* (K. Dholakia and G. C. Spalding, eds.), vol. 6326, pp. 355–362, SPIE, 2006.
- [127] TAG Optics Inc., *Product Specifications Sheet TAG Lens 2.0 – Model TL2.B*, 2013.
- [128] S. Piazza, P. Bianchini, C. Sheppard, A. Diaspro, and M. Duocastella, “Enhanced volumetric imaging in 2-photon microscopy via acoustic lens beam shaping,” *J. Biophotonics*, vol. 11, no. 2, p. e201700050, 2017.
- [129] M. Duocastella and C. B. Arnold, “Enhanced depth of field laser processing using an ultra-high-speed axial scanner,” *Appl. Phys. Lett.*, vol. 102, no. 6, p. 061113, 2013.
- [130] L. Kong, J. Tang, and M. Cui, “*In vivo* volumetric imaging of biological dynamics in deep tissue via wavefront engineering,” *Opt. Express*, vol. 24, no. 2, pp. 1214–1221, 2016.
- [131] L. Kong, J. Tang, J. P. Little, Y. Yu, T. Lämmermann, C. P. Lin, R. N. Germain, and M. Cui, “Continuous volumetric imaging via an optical phase-locked ultrasound lens,” *Nat. Methods*, vol. 12, no. 8, pp. 759–762, 2015.
- [132] E. McLeod, A. B. Hopkins, and C. B. Arnold, “Multiscale Bessel beams generated by a tunable acoustic gradient index of refraction lens,” *Opt. Lett.*, vol. 31, no. 21, pp. 3155–3157, 2006.

-
- [133] “TAG Optics Home.” TAG Optics Inc., Retrieved on 2018-11-2, <http://tag-optics.com/>.
- [134] S. Sato, “Liquid-crystal lens-cells with variable focal length,” *Japanese Journal of Applied Physics*, vol. 18, no. 9, p. 1679, 1979.
- [135] C.-P. Chiu, T.-J. Chiang, J.-K. Chen, F.-C. Chang, F.-H. Ko, C.-W. Chu, S.-W. Kuo, and S.-K. Fan, “Liquid lenses and driving mechanisms: A review,” *J. Adhes. Sci. Technol.*, vol. 26, no. 12-17, pp. 1773–1788, 2012.
- [136] A. Jamali, D. Bryant, Y. Zhang, A. Grunnet-Jepsen, A. Bhowmik, and P. J. Bos, “Design of a large aperture tunable refractive Fresnel liquid crystal lens,” *Appl. Opt.*, vol. 57, no. 7, pp. B10–B19, 2018.
- [137] A. Jamali, *Large area tunable liquid crystal lens*. PhD thesis, 2018.
- [138] J. Beeckman, T.-H. Yang, I. Nys, J. Puthenparampil George, T.-H. Lin, and K. Neyts, “Multi-electrode tunable liquid crystal lenses with one lithography step,” *Opt. Lett.*, vol. 43, no. 2, pp. 271–274, 2018.
- [139] H. Li, J. Peng, F. Pan, Y. Wu, Y. Zhang, and X. Xie, “Focal stack camera in all-in-focus imaging via an electrically tunable liquid crystal lens doped with multi-walled carbon nanotubes,” *Opt. Express*, vol. 26, no. 10, pp. 12441–12454, 2018.
- [140] T. Galstian, O. Sova, K. Asatryan, V. Presniakov, A. Zohrabyan, and M. Evensen, “Optical camera with liquid crystal autofocus lens,” *Opt. Express*, vol. 25, no. 24, pp. 29945–29964, 2017.
- [141] H.-S. Chen, Y.-J. Wang, P.-J. Chen, and Y.-H. Lin, “Electrically adjustable location of a projected image in augmented reality via a liquid-crystal lens,” *Opt. Express*, vol. 23, no. 22, pp. 28154–28162, 2015.
- [142] R. Wei, D. Wang, and Q.-H. Wang, “P-85: Color holographic display system based on liquid crystal lens,” *SID Symposium Digest of Technical Papers*, vol. 47, no. 1, pp. 1443–1445, 2016.
- [143] L. Li, D. Bryant, T. Van Heugten, and P. J. Bos, “Speed, optical power, and off-axis imaging improvement of refractive liquid crystal lenses,” *Appl. Opt.*, vol. 53, no. 6, pp. 1124–1131, 2014.
- [144] A. A. Ingram, “Fluid lens.” US509379A, 1893.
- [145] D. G. Schaller, “Vorrichtung zur scharfeinstellung elastischer und fester objektive photographischer kameras mittels eines sucher-prismas.” DE000000258963A, 1913.
- [146] K. Ritzmann, “Linse mit veränderlicher optischer wirkung.” DE000000628774A, 1936.
- [147] R. Graham, “A variable focus lens and its uses,” *J. Opt. Soc. Am.*, vol. 30, no. 11, pp. 560–563, 1940.

- [148] “Adaptive Optics Technologies Company | Dynamic Optics.” Dynamic Optics S.r.l., Retrieved on 2019-2-14, <https://dynamic-optics.eu/>.
- [149] S. Bonora, Y. Jian, P. Zhang, A. Zam, E. N. Pugh, R. J. Zawadzki, and M. V. Sarunic, “Wavefront correction and high-resolution in vivo OCT imaging with an objective integrated multi-actuator adaptive lens,” *Opt. Express*, vol. 23, no. 17, pp. 21931–21941, 2015.
- [150] M. Blum, M. Büeler, C. Grätzel, and M. Aschwanden, “Compact optical design solutions using focus tunable lenses,” in *Optical Design and Engineering IV*, vol. 8167, pp. 274–282, SPIE, 2011.
- [151] H. Huang, K. Wei, Q. Wang, and Y. Zhao, “Improved optical resolution for elastomer-liquid lens at high diopter using varied thickness membrane,” in *Proc. SPIE*, vol. 9705, p. 970504, 2016.
- [152] M. C. Flores-Bustamante, M. Rosete-Aguilar, and S. Calixto, “Mechanical and optical behavior of a tunable liquid lens using a variable cross section membrane: modeling results,” in *Proc. SPIE*, vol. 9699, p. 969908, 2016.
- [153] A. Mikš and F. Šmejkal, “Dependence of the imaging properties of the liquid lens with variable focal length on membrane thickness,” *Appl. Opt.*, vol. 57, no. 22, p. 6439, 2018.
- [154] W. Jia, D. Xiang, and S. Li, “A liquid progressive multifocal lens adjusted by the deformation of a non-uniform elastic membrane due to the variation of liquid pressure,” *Journal of the European Optical Society-Rapid Publications*, vol. 14, no. 1, p. 17, 2018.
- [155] “Optotune.” Optotune, Retrieved on 2017-7-26, <http://www.optotune.com/>.
- [156] M. Ozolinsh, J. Berzinsh, A. Pastare, P. Paulins, and Z. Jansone, “Tunable liquid lens equipped virtual reality adapter for scientific, medical, and therapeutic goals,” in *Optoelectronic Imaging and Multimedia Technology V* (Q. Dai and T. Shimura, eds.), vol. 10817, pp. 8–14, SPIE, 2018.
- [157] W. B. Schneider, “Ein einfaches, wenig bekanntes verfahren zum bau einer linse mit einstellbarer brennweite,” *PhuD*, vol. 2, pp. 158–160, 1988.
- [158] W. B. Schneider, “A lenses with an adjustable focal length,” *The Physics Teacher*, vol. 31, no. 2, pp. 118–119, 1993.
- [159] B. Berge and J. Peseux, “Lentille à focale variable.” FR2769375A1, 1997.
- [160] B. Berge and J. Peseux, “Variable focal lens controlled by an external voltage: An application of electrowetting,” *Eur. Phys. J. E*, vol. 3, no. 2, pp. 159–163, 2000.

-
- [161] S. Kuiper and B. H. W. Hendriks, “Variable-focus liquid lens for miniature cameras,” *Appl. Phys. Lett.*, vol. 85, no. 7, pp. 1128–1130, 2004.
- [162] K. Mishra, C. Murade, B. Carreel, I. Roghair, J. M. Oh, G. Manukyan, D. van den Ende, and F. Mugele, “Optofluidic lens with tunable focal length and asphericity,” *Sci. Rep.*, vol. 4, no. 6378, 2014.
- [163] K. Mishra and F. Mugele, “Numerical analysis of electrically tunable aspherical optofluidic lenses,” *Opt. Express*, vol. 24, no. 13, pp. 14672–14681, 2016.
- [164] “Corning® Varioptic® Lenses | Driver for Adjustable Lens | Corning.” Corning Incorporated, Retrieved on 2018-5-20, <http://www.corning.com/worldwide/en/innovation/corning-emerging-innovations/corning-varioptic-lenses.html>.
- [165] “Barcode Readers | Cognex.” Cognex Cooperation, <https://www.cognex.com/products/barcode-readers>. Accessed on 2018-11-29.
- [166] G. Lippmann, *Relations entre les phénomènes électriques et capillaires*. PhD thesis, 1875.
- [167] F. Mugele and J.-C. Baret, “Electrowetting: from basics to applications,” *J. Phys.: Condens. Matter*, vol. 17, no. 28, p. R705, 2005.
- [168] B. Berge, “Electrocapillarité et mouillage de films isolants par l’eau,” *C. R. Acad. Sci. II*, vol. 317, p. 157, 1993.
- [169] P. G. de Gennes, “Wetting: statics and dynamics,” *Rev. Mod. Phys.*, vol. 57, no. 3, pp. 827–863, 1985.
- [170] T. B. Jones, “On the relationship of dielectrophoresis and electrowetting,” *Langmuir*, vol. 18, no. 11, pp. 4437–4443, 2002.
- [171] T. B. Jones, J. D. Fowler, Y. S. Chang, and C.-J. Kim, “Frequency-based relationship of electrowetting and dielectrophoretic liquid microactuation,” *Langmuir*, vol. 19, no. 18, pp. 7646–7651, 2003.
- [172] G. S. Jung, J. S. Lee, and Y. H. Won, “Effects of liquid property and substrate roughness on the response time of an electrowetting liquid spectral,” in *Proc. SPIE*, vol. 10545, p. 1054516, 2018.
- [173] “Wolfram|alpha.” Wolfram Alpha LLC, Retrieved on 2018-12-1, <https://www.wolframalpha.com/input/?i=water+glycerol+dodecane>.
- [174] “Wolfram|alpha.” Wolfram Alpha LLC, Retrieved on 2018-12-1, <https://www.wolframalpha.com/input/?i=chloronaphthalene>.
- [175] “Wolfram|alpha.” Wolfram Alpha LLC, Retrieved on 2018-12-1, <https://www.wolframalpha.com/input/?i=sodium+lauryl+sulfate>.

- [176] M. Maillard, J. Legrand, and B. Berge, “Two liquids wetting and low hysteresis electrowetting on dielectric applications,” *Langmuir*, vol. 25, no. 11, pp. 6162–6167, 2009.
- [177] “TEDS - 140901 - Arctic 39N0 manual.” Parrot SA, 2014.
- [178] “TEDS - 131028 - Arctic 39N0 manual.” Parrot SA, 2013.
- [179] M. Strauch, Y. Shao, F. Bociort, and H. P. Urbach, “Study of surface modes on a vibrating electrowetting liquid lens,” *Appl. Phys. Lett.*, vol. 111, no. 17, p. 171106, 2017.
- [180] T. Krupenkin, S. Yang, and P. Mach, “Tunable liquid microlens,” *Appl. Phys. Lett.*, vol. 82, no. 3, pp. 316–318, 2003.
- [181] C. A. López and A. H. Hirsra, “Fast focusing using a pinned-contact oscillating liquid lens,” *Nat. Photonics*, vol. 2, pp. 610–613, 2008.
- [182] B. H. W. Hendriks, S. Kuiper, M. A. J. van As, C. A. Renders, and T. W. Tukker, “Variable liquid lenses for electronic products,” in *Proc. SPIE*, vol. 6034, p. 603402, 2006.
- [183] F. Zhang, Y. Yao, X. Qu, T. Zhang, and B. Pei, “Dual-beam laser autofocusing system based on liquid lens,” *Opt. Laser Technol.*, vol. 88, pp. 198–204, 2017.
- [184] K. Wei, H. Huang, Q. Wang, and Y. Zhao, “Focus-tunable liquid lens with an aspherical membrane for improved central and peripheral resolutions at high diopters,” *Opt. Express*, vol. 24, no. 4, pp. 3929–3939, 2016.
- [185] G. Diaz-Gonzalez, A. Santiago-Alvarado, J. Munoz-Lopez, R. Juarez-Salazar, A. S. Cruz-Felix, and N. Jiménez-Barriga, “Characterization of a tunable liquid-filled lens with minimum spherical aberration,” in *Proc. SPIE*, vol. 9947, p. 99470H, 2016.
- [186] D. Kopp, T. Brender, and H. Zappe, “All-liquid dual-lens optofluidic zoom system,” *Appl. Opt.*, vol. 56, no. 13, pp. 3758–3763, 2017.
- [187] Lord Rayleigh, “On the capillary phenomena of jets,” *Proc. Roy. Soc. London*, vol. 29, no. 196-199, pp. 71–97, 1879.
- [188] C. A. Miller and L. E. Scriven, “The oscillations of a fluid droplet immersed in another fluid,” *J. Fluid Mech.*, vol. 32, no. 3, pp. 417–435, 1968.
- [189] A. Prosperetti, “Free oscillations of drops and bubbles: the initial-value problem,” *J. Fluid Mech.*, vol. 100, no. 2, pp. 333–347, 1980.
- [190] O. A. Basaran, “Nonlinear oscillations of viscous liquid drops,” *J. Fluid Mech.*, vol. 241, pp. 169–198, 1992.
- [191] J. B. Bostwick and P. H. Steen, “Capillary oscillations of a constrained liquid drop,” *Phys. Fluids*, vol. 21, no. 3, p. 032108, 2009.

-
- [192] A. Frohn and N. Roth, *Dynamics of Droplets*. Berlin: Springer, 2000.
- [193] L. D. Landau and E. M. Lifshitz, *Fluid Mechanics*, vol. 6 of *Course of Theoretical physics*. London: Butterworth-Heinemann, 2 ed., 2003.
- [194] P. Hagedorn and A. DasGupta, *Vibrations and waves in continous mechanical systems*. Chichester: John Wiley & Sons, 2007.
- [195] A. M. Weiner, “Femtosecond pulse shaping using spatial light modulators,” *Rev. Sci. Instrum.*, vol. 71, no. 5, pp. 1929–1960, 2000.
- [196] M. Kac, “Can one hear the shape of a drum?,” *Am. Math. Mon.*, vol. 73, no. 4, pp. 1–23, 1966.
- [197] J. W. Goodman, *Introduction to Fourier Optics*. New York: McGraw-Hill, 2 ed., 1996.
- [198] J. W. Goodman, *Statistical Optics*. New York: Wiley-Interscience, Wiley Classics Library ed., 2000.
- [199] I. Robertson, S. J. Sherwin, and J. M. R. Graham, “Comparison of wall boundary conditions for numerical viscous free surface flow simulation,” *J. Fluids Struct.*, vol. 19, no. 4, pp. 525–542, 2004.
- [200] J. Durnin, J. J. Miceli, and J. H. Eberly, “Diffraction-free beams,” *Phys. Rev. Lett.*, vol. 58, no. 15, pp. 1499–1501, 1987.
- [201] J. Durnin, “Exact solutions for nondiffracting beams. i. the scalar theory,” *J. Opt. Soc. Am. A*, vol. 4, no. 4, pp. 651–654, 1987.
- [202] M. Strauch, P. A. A. M. Somers, F. Bociort, and H. P. Urbach, “Creation of aspheric interfaces on an electrowetting liquid lens using surface oscillations,” *AIP Adv.*, vol. 8, no. 11, p. 115224, 2018.
- [203] Y. Shimizu, D. Koyama, M. Fukui, A. Emoto, K. Nakamura, and M. Matsukawa, “Ultrasound liquid crystal lens,” *Appl. Phys. Lett.*, vol. 112, no. 16, p. 161104, 2018.
- [204] A. Y. Malyuk and N. A. Ivanova, “Varifocal liquid lens actuated by laser-induced thermal Marangoni forces,” *Appl. Phys. Lett.*, vol. 112, no. 10, p. 103701, 2018.
- [205] I. S. Park, Y. Park, S. H. Oh, J. W. Yang, and S. K. Chung, “Multifunctional liquid lens for variable focus and zoom,” *Sens. Actuators, A*, vol. 273, pp. 317–323, 2018.
- [206] D. R. Schipf and W.-C. Wang, “Liquid surface oscillations for a time-dependent random-phase security system,” in *Proc. SPIE*, vol. 10559, p. 1055908, 2018.
- [207] D. R. Schipf and W.-C. Wang, “Optical encryption using a liquid phase mask,” *OSA Continuum*, vol. 1, no. 3, pp. 1026–1040, 2018.

- [208] R. A. Ibrahim, *Liquid Sloshing Dynamics: Theory and Applications*. Cambridge: Cambridge University Press, 2005.
- [209] G. B. Arfken and H. J. Weber, *Mathematical Methods for Physicists*. Amsterdam: Academic Press, 6 ed., 2005.
- [210] I. N. Bronstein, K. A. Semendjajew, G. Musiol, and H. Mühlig, *Taschenbuch der Mathematik*. Frankfurt am Main: Harri Deutsch, 6 ed., 2005.
- [211] G. N. Watson, *A Treatise on the Theory of Bessel Functions*. New York: Cambridge University Press, Cambridge mathematical library 2 ed., 1995.
- [212] W. Kaplan, *Advanced Calculus*. Redwood City: Addison-Wesley, 4 ed., 1991.
- [213] A. D. Poularikas, *The Transforms and applications handbook*. Boca Raton: CRC Press, 2 ed., 2000.
- [214] L. Debnath and D. Bhatta, *Integral Transforms and Their Applications*. Boca Raton: CRC Press, 3 ed., 2015.
- [215] K. B. M. Nambudiripad, *Bessel Functions*. Oxford: Alpha Science International, 2013.
- [216] A. E. Siegman, "Quasi fast hankel transform," *Opt. Lett.*, vol. 1, no. 1, pp. 13–15, 1977.
- [217] M. Guizar-Sicairos and J. C. Gutiérrez-Vega, "Computation of quasi-discrete hankel transforms of integer order for propagating optical wave fields," *J. Opt. Soc. Am. A*, vol. 21, no. 1, pp. 53–58, 2004.
- [218] M. Leutenegger, "Matlab toolbox hankel transform," 2007.
- [219] M. Takeda, H. Ina, and S. Kobayashi, "Fourier-transform method of fringe-pattern analysis for computer-based topography and interferometry," *J. Opt. Soc. Am.*, vol. 72, no. 1, pp. 156–160, 1982.
- [220] D. C. Ghiglia and M. D. Pritt, *Two-Dimensional Phase Unwrapping: Theory, Algorithms, and Software*. New York: John Wiley, 1998.
- [221] X. Na, Z. Ning, and X. Rong-Qing, "Effect of driving voltage polarity on dynamic response characteristics of electrowetting liquid lens," *Jpn. J. Appl. Phys.*, vol. 57, no. 5, p. 052201, 2018.
- [222] R. J. Noll, "Zernike polynomials and atmospheric turbulence," *J. Opt. Soc. Am.*, vol. 66, no. 3, pp. 207–211, 1976.
- [223] Q. Kemao, "Windowed fourier transform for fringe pattern analysis," 2008.

Appendix

A. Optical design specifications

This appendix gives an overview over the used lens designs in chapter 2. Additionally the (not so trivial) way of creating useful spectral transmittance plots with CODE V is explained using macro code samples.

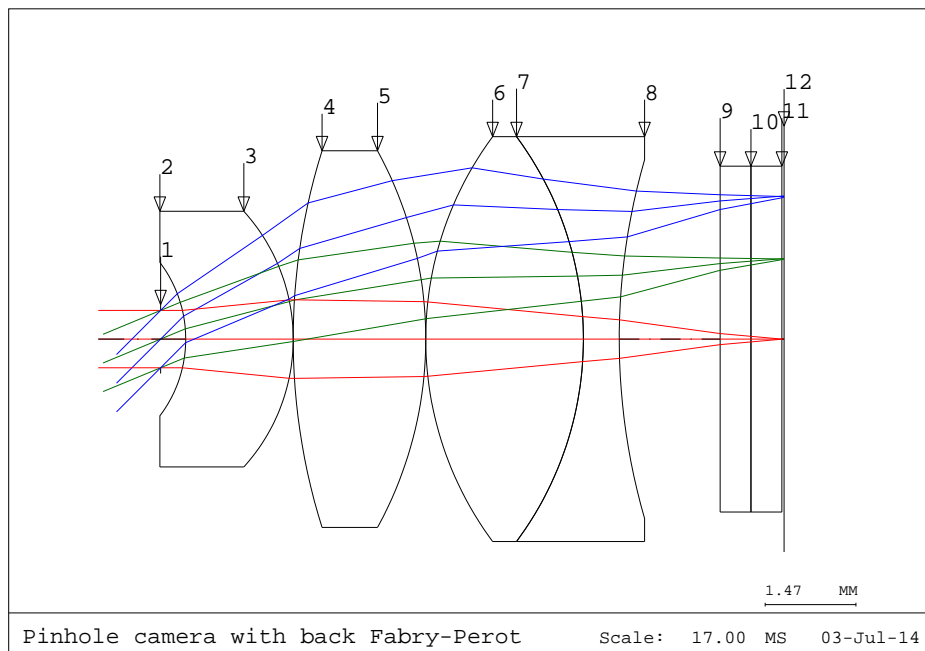
A.1. Lens designs

The initial design is shown in Figure A.1 together with all relevant dimensions. The aperture stop diameter is 1 mm. The full field of view is 90° . The displayed model already shows the FPI as a double glass plate with an intermediate FPI coating representing the spectral physics and zero distance. This was not part of the initial model by Irina Livshits but does not change the spatial optical performance. The coating contains the used Fabry-Pérot mirror coatings and an air layer in between that is varied in size (450 nm–700 nm).

The telecentric design is displayed in Figure A.2 and the collimated design in Fig. A.3. The aberration coefficients of all designs are small except of the distortion, which is very common for wide-angle objectives.

Aberration	Initial	Telecentric	Collimated
Spherical aberration	-0.003	-0.001	-0.006
Tangential coma	-0.020	-0.035	-0.004
Tangential astigmatic blur	0.029	-0.008	0.022
Sagittal astigmatic blur	-0.021	-0.029	-0.025
Petzval blur	-0.047	-0.040	-0.048
Distortion	-1.961	-2.241	-2.400
Axial colour	-0.006	-0.008	-0.003
Lateral colour	-0.031	-0.050	-0.029
Petzval surface curvature	-0.058	-0.040	-0.035

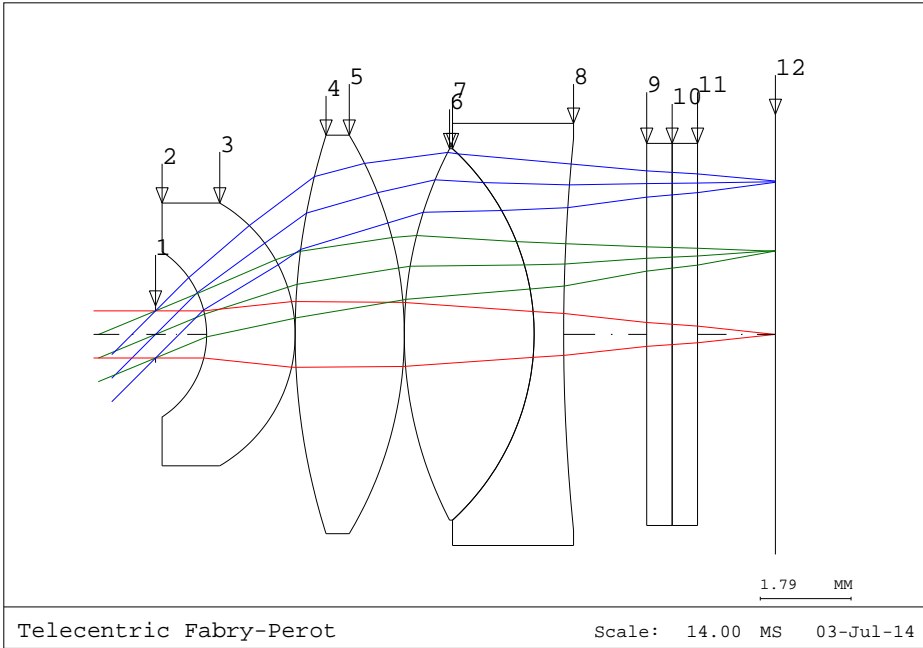
16:15:16



Surface	Radius	Thickness	Glass
Object	∞	∞	
Stop	∞	0.40618	
2	-2.0541	1.74076	N-LAF35
3	-3.0814	0	
4	10.20085	2.14691	P-SK60
5	-6.34797	0	
6	5.50428	2.55311	N-LAF35
7	-5.50428	0.58025	N-SF6
8	10.48634	1.63419	
9	∞	0.5	N-BK7
10	∞	0.5	N-BK7
11	∞	0.03508	
Image	∞	0	

Figure A.1.: Irina Livshits' original lens design

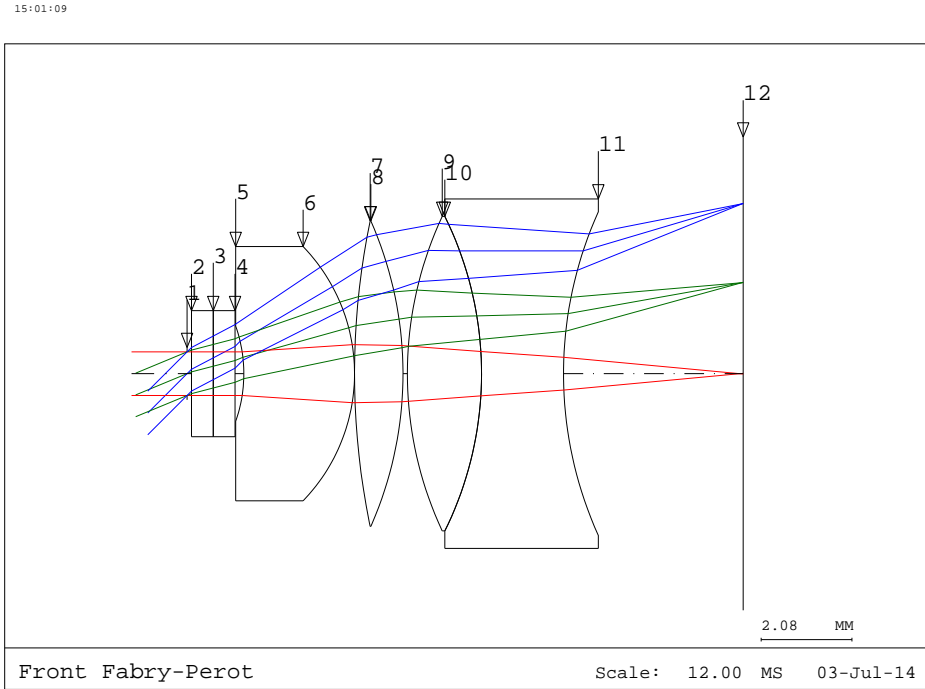
15:32:43



Surface	Radius	Thickness	Glass
Object	∞	∞	
Stop	∞	1.00487	
2	-1.9453	1.74076	N-LAF35
3	-2.9936	0	
4	12.9295	2.14691	P-SK60
5	-7.6334	0	
6	7.9412	2.55311	N-LAF35
7	-4.9615	0.58025	N-SF6
8	38.1777	1.63419	
9	∞	0.5	N-BK7
10	∞	0.5	N-BK7
11	∞	1.53073	
Image	∞	0	

Figure A.2.: Telecentric configuration

A. Optical design specifications



Surface	Radius	Thickness	Glass
Object	∞	∞	
Stop	∞	0.1	
2	∞	0.5	N-BK7
3	∞	0.5	N-BK7
4	∞	0.20143	
5	-3.3008	2.54000	N-LAF35
6	-4.1950	0	
7	17.3129	1.11206	P-SK60
8	-8.6899	0.1	
9	8.5384	1.70222	N-LAF35
10	-8.1595	1.88081	N-SF6
11	9.0360	4.12234	
Image	∞	0	

Figure A.3.: Collimated configuration

A.2. Transmittance spectrum analysis in CODE V

The analysis of the spectral transmittance is done with CODE V *.seq macros. In general a design can be evaluated by calling a functions that calls two functions and a command. The following code gives a brief explanation how such a plot can be created and evaluated using the Fortran style macro language of CODE V. At the basic level the TRA command calls the transmission functionality of CODE V. Usually a plot is created for all wavelengths and fields of the optical design. The amount of wavelengths is however limited to 21 and the amount of fields is limited to 10. To get a plot of sufficient spectral resolution the function TRA has to be called multiple times to create useful data or plots. The following function 10fieldsTRAtoB1.seq copies the calculated datapoints from the buffer B0 to a second buffer B1 for a set of 10 fields and a desired wavelength range $\hat{\text{minlambda}} - \hat{\text{maxlambda}}$.

The function input variables are defined like this:

```
!Input: Minimum wavelength Maximum wavelength Reference wavelength
RFD 450 700 548
NUM ^lambda(21)
^minlambda == #1
^maxlambda == #2
^reflambda == #3
```

Create 20 wavelengths from the min and max values and add the reference wavelength as a 21st value to assure the coating thickness properties are calculated correctly.

```
FOR ^lambi 1 20
  ^lambda(^lambi) == ^maxlambda - (^maxlambda-^minlambda)/20*^lambi
END FOR
WL ^lambda(1) ^lambda(2) ^lambda(3) ^lambda(4) ^lambda(5) ^lambda(6)
  ^lambda(7) ^lambda(8) ^lambda(9) ^lambda(10) ^lambda(11)
  ^lambda(12) ^lambda(13) ^lambda(14) ^lambda(15) ^lambda(16)
  ^lambda(17) ^lambda(18) ^lambda(19) ^lambda(20) ^lambda(21)
FOR ^i 1 21
  IF (WL W^i) = ^reflambda
    REF ^i
  END IF
END FOR
```

Delete the existing buffers B0 and B1, start writing the buffer, call the transmission analysis tool TRA, stop writing the buffer, and find the entry "Ave Transmittance:" to set the cursor to the correct position in buffer B0 with coordinates IC and JC.

```
BUF DEL B0
BUF Y
TRA
GO
BUF N
BUF FND "Ave Transmittance:"
BUF DEL B1
!Buffer format B1:
!Wavelength1 TRAFfield1 TRAFfield2 ... TRAFfield10
!Wavelength2 TRAFfield1 TRAFfield2 ... TRAFfield10
```

```
!...
!Wavelength21 TRAField1 TRAField2 ... TRAField10
```

TRA creates three lines of output values of each 7 values. The values have to be copied value by value to buffer B1 to be saved from being overwritten, when the next CODE V function is called. The wavelength is written to position J1 in buffer B1 and the first transmission value is written to J2.

```
FOR ^w 1 7
  BUF PUT B1 I^w (WL W^w) (BUF.NUM B0 IC J^w+1)
END FOR
FOR ^w 8 14
  BUF PUT B1 I^w (WL W^w) (BUF.NUM B0 IC+1 J^w-7)
END FOR
FOR ^w 15 (NUM W)
  BUF PUT B1 I^w (WL W^w) (BUF.NUM B0 IC+2 J^w-14)
END FOR
```

This has to be repeated for all 10 fields always preceded by a BUF FND command to reset the position of the cursor to the first value of the next field. The last step is deleting the row in buffer B1 that contains the reference wavelength to avoid creating data for the reference wavelength every time the function is called.

```
FOR ^w 1 (BUF.LST B1)
  IF (WL W^w) = #3
    ^deleteThatRow == ^w
  END IF
END FOR
BUF DEL B1 I^deleteThatRow
```

To create plots containing more than 21 wavelengths the TRA function has to be called again. This is done by a second macro: AccurateTRAplot10fields.seq It saves the buffer containing all buffers into a file. The chosen spectral resolution is 1 nm. The output is suppressed to increase speed.

```
!Input: file path
RFD "C:\example.dat"
^path == #1
OUT N
```

The minimum and maximum wavelength values as well as the reference wavelength are taken over from the general lens design. They are stored in an extra variable such that it is possible to restore them in the end. Buffer B2 is used to store the output for all wavelengths collected from all buffers B1. The format is identical to B1. Initially it is emptied.

```
^lambdamax == (WL W1)           !maximum wavelength
^numw == (NUM W)               !number of wavelengths
^lambdamin == (WL W^numw)      !minimum wavelength
^ref == (REF)                  !index of the reference
  wavelength
^lambdaref == (WL W^ref)       !reference wavelength
BUF DEL B2
^B2currentline == 0           !Index used to merge loop
  results
```

The wavelength interval is scanned with 1,nm precision. Since CODE V cannot handle more than 21 wavelengths at a time the task is split into 20nm intervals starting from the maximal wavelength. The 21st wavelength has to be the reference wavelength to keep the correct coating thickness. 10fieldsTRAtoB1.seq writes creates a buffer B1 containing 21 wavelengths. It is copied into buffer B2.

```

^currentmin == ^lambdamax                !minimum wavelength of 20nm
interval
WHI ^lambdamin < ^currentmin - 20
    ^currentmax == ^currentmin            !max lambda is now previous
    min lambda
    ^currentmin == ^currentmin - 20      !min lambda is reduced by
    20nm
RUN "C:\10fieldsTRAtoB1.seq" ^currentmin ^currentmax ^lambdaref
FOR ^i 1 20
    ^B2currentline == ^B2currentline + 1
    BUF PUT B2 i^B2currentline (BUF.NUM B1 I^i J1) (BUF.NUM B1 I^i
    J2) (BUF.NUM B1 I^i J3) (BUF.NUM B1 I^i J4) (BUF.NUM B1 I^i J5)
    (BUF.NUM B1 I^i J6) (BUF.NUM B1 I^i J7) (BUF.NUM B1 I^i J8)
    (BUF.NUM B1 I^i J9) (BUF.NUM B1 I^i J10) (BUF.NUM B1 I^i J11)
END FOR
END WHI

```

Ultimately the original wavelength values can be restored, the buffer is saved to a tab-separated file and the text output can be switched back to normal.

```

WL ^lambdamax ^lambdaref ^lambdamin
REF 2
BUF EXP B2 ^path
OUT Y

```

To simulate the transmittance for different mirror distances of the FPI a third macro needs to be called, that changes the multilayer coating for every mirror position. This is done by AccurateTRAplot10fields9wavelengths.seq. It creates plots for a specified set of mirror distances. 10 input fields need to be defined to run it

```

!Input: None
XAN  0.0 0.0 0.0 0.0 0.0 0.0 0.0 0.0 0.0 0.0
YAN  0.0 5.0 10.0 15.0 20.0 25.0 30.0 35.0 40.0 45.0

```

The multilayer coating is loaded from a .mul file and applied on the FPI surface (here: S10). Then the previous macro is called to calculate the complete transmittance dataset and save it.

```

MLT S10 "C:\6xSiO2TiO2FPI450nm.mul"
RUN "C:\AccurateTRAplot10fields.seq" "C:\example450nm.dat"

```

Plot buffer B2.

```

UGR
TIT "Transmission for 10 fields          Fabry-Perot gap: 450nm"
XLA "Wavelength (nm)"
YLA "Transmittance"
DTB B2 IA JA " 0deg" " 5deg" "10deg" "15deg" "20deg" "25deg"
"30deg" "35deg" "40deg" "45deg"

```

GO

Applying a new multilayer coating, creating the buffer and plotting it has to be repeated for each mirror distance. To calculate the effects on the spectral transmittance for linearly polarised light polarisation ray tracing has to be turned on globally in the CODE V lens model.

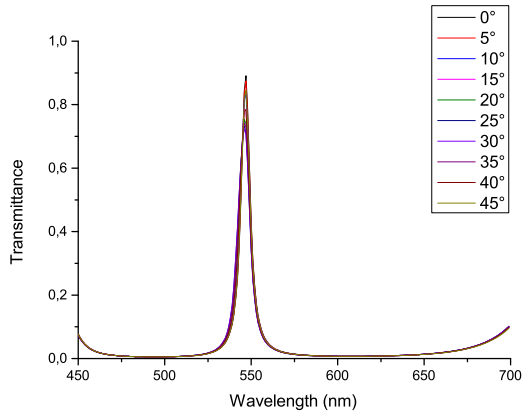


Figure A.4.: Transmittance of the telecentric configuration (see Fig. A.2) for a mirror gap of 548 nm and unpolarised light.

The results of running `AccurateTRAp10fields.seq` for both the collimated and telecentric configuration are displayed in Fig. A.5 and Fig. A.4, respectively.

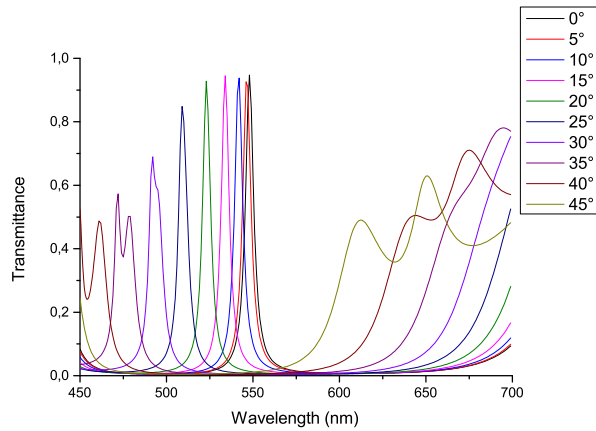


Figure A.5.: Transmittance of the collimated configuration (see Fig. A.3) for a mirror gap of 548 nm and unpolarised light. For higher field angles the peaks shift, broaden, and even split up. These double peaks occur due to different peak wavelengths for s- and p-polarisation.

B. Voltage signal generation

B.1. Amplification

The voltage output of the PC is transferred via USB to a NI-9263 D/A converter. The voltage is amplified 8 times with a self-built amplifier (Fig. B.1 & B.2) and applied to the liquid lens (LL). The capacitance of the LL is 500 pF at 1 Hz sinusoidal driving frequency. The DC voltage supply of the amplifier is generated by two output channels of a Keithley 2230-30-1 Triple Channel DC Power Supply of each 30 V. In consequence, the voltage applied to the LL cannot exceed 60 V.

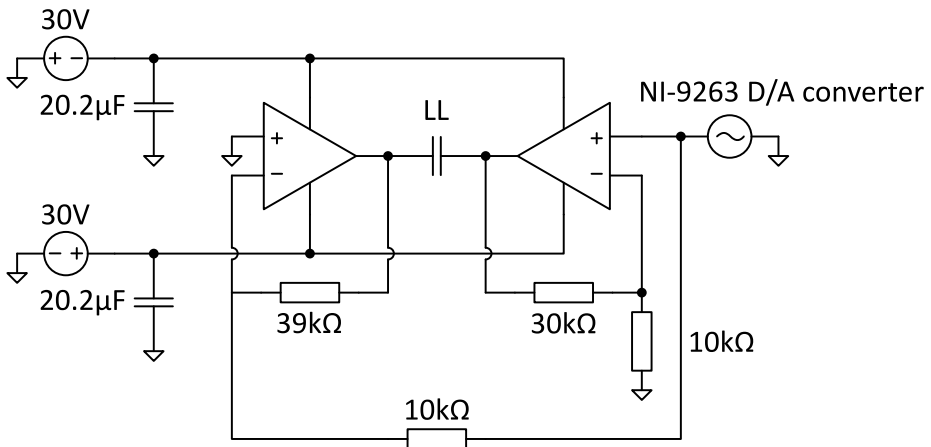


Figure B.1.: Circuit diagram of the 8x voltage amplifier. The signal is applied via the D/A converter, amplified 8 times and applied to the LL.

B.2. LabView software

The LL is fed through a D/A converter controlled by a LABVIEW software that serves as an arbitrary waveform generator. There are two versions of the program serving two different purposes that were necessary to investigate the surface wave phenomena for sine waves with constant frequency and arbitrary waveforms, respectively. The more basic version of the software is called Control program v2_3.vi.

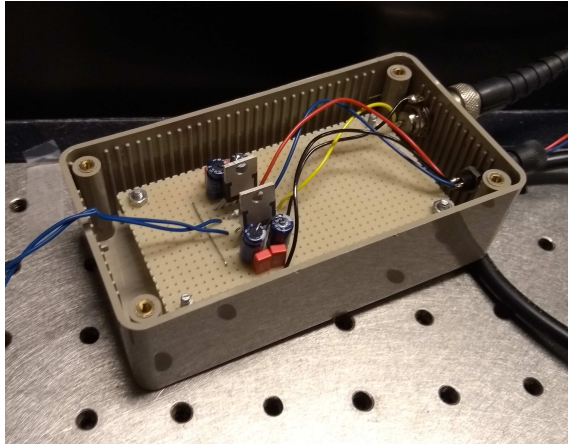


Figure B.2.: Photo of the 8x voltage amplifier as designed and built by Roland Horsten

B.2.1. Creation of cosine waveforms

The program serves two main functions, modulating the liquid lens and reading out the camera. The upper part as shown in figure B.3 controls the actuation voltage and the lower part shows the light pattern measured by the camera.

B.2.2. Liquid lens signal generation

A square wave with constant amplitude (23–70 V) has to be applied to create a static liquid lens surface. The frequency of the square wave can be chosen freely but usually ranges between 0.5–2 kHz. Please be aware that low frequencies <50 Hz can excite assymmetric oscillations of the liquid lens surface and might make the LL unusable due to mixing of the liquids. This process is reversible and usually requires waiting a few minutes. Throughout all experiments presented in this thesis the frequency of the square wave has been chosen to be 1136 Hz. On top of this signal there is an amplitude modulation added, that is actually modulating the LL surface. This cosine voltage can be chosen arbitrarily but is of course limited by the maximum voltage range of the LL ± 70 V. The frequency can be chosen freely. The signal is generated in the following way:

$$[SW_{ampl} + Cos_{ampl} \cos(2\pi \times Cos_{freq} \times t)]_{rect}(2\pi \times SW_{freq} \times t). \quad (B.1)$$

One buffer (1000 samples) of the resulting signal is displayed in the waveform graph next to the controls. The duty cycle of the square wave is usually chosen to be 50%. The exact block diagram realisation including comments on how to use the D/A converter card is shown in figure B.4. As a second feature, a TTL signal is generated to trigger the camera.

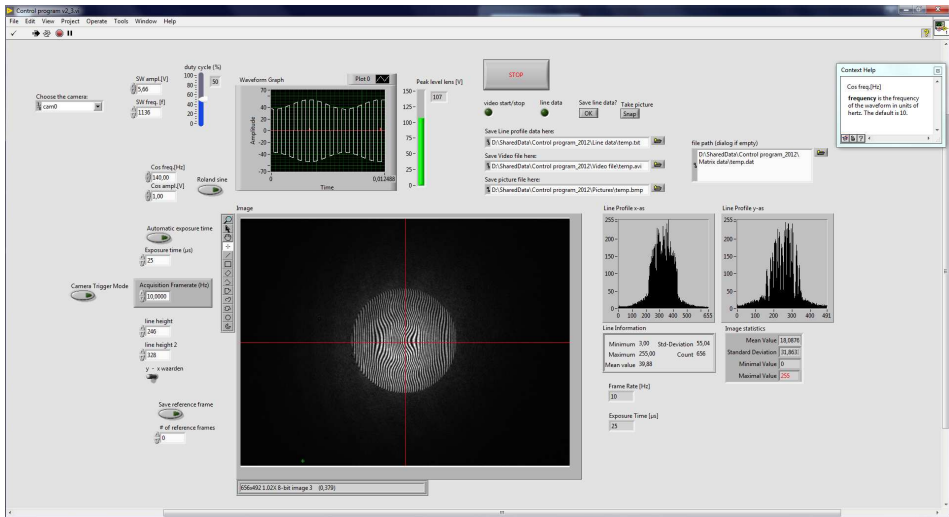


Figure B.3.: Labview interface of the Liquid lens control program. The camera shows the interference pattern as observed in a Mach-Zehnder setup.

B.2.3. Camera driver

The lower part of the Labview interface allows controlling the camera by its frame rate or using the generated trigger. The used camera has to be selected before the code starts running. The measured light pattern is displayed as an Image. The line height control moves a line through the image, along which line profiles are extracted and displayed on the right. Image and line statistics can be used to evaluate the noise in the image and avoid overexposure during measurements. The exposure time can be used to control the integration time of the camera sensor as long as it does not exceed the frame rate. In trigger mode, the camera will integrate over the full exposure time and wait for the next trigger after it finished. The code (Fig. B.5) was written for two different cameras with different resolutions and frame rates. The relevant parameters can be downloaded from the camera as .xml files. All pictures and videos can be saved uncompressed and a reference matrix can be taken (and integrated over several frames) to calibrate the interferometer.

B.2.4. Arbitrary liquid lens surface generation

An arbitrary liquid lens surface shape can only be created by creating a specific time dependent actuation signal. The corresponding program is `Control program v2_3Audio.vi`. Within the limitations of the D/A converter the wavefront can be calculated with the Hankel transform in Matlab as explained in appendix D. For convenience the calculated modulation was saved as a .wav audio file to be easily exported and imported with different kinds of software (Matlab, Labview, Audacity). The first channel contains the LL modulation and

the second channel the trigger signal.

The actuation signal consists of the same square wave as explained above, but replaces the cosine signal with the calculated voltage modulation

$$(SW\text{ampl} + \text{Amplification} \times \text{Audiofile})\text{rect}(2\pi \times SW\text{freq} \times t). \quad (\text{B.2})$$

For edutainment purposes the audio files can be replaced with real audio files to visualise music using the liquid lens. To do this, the sampling rate has to be changed from 80kSamples to 47kSamples to match common audio standards. Figure B.6 depicts how this can be implemented in Labview.

When watching music triggering the camera is unnecessary, since there is no trigger signal on the stereo channels.

C. Interferogram analysis

The surface of the liquid lens (LL) can be computed from the fringe patterns measured with the Mach-Zehnder interferometer. The fundamental concept of the computation is explained in Section 5.4. This appendix will give a short explanation how to compute the surface of the LL in Matlab. Starting point is the measured interference fringe pattern obtained by the LabVIEW program described in Appendix B.

First, LabVIEW has to read in the interferogram of interest. That can be either a single image via `importdata('Fringe.dat','t')` or a video of the fringe pattern with the `VideoReader` function.

```
videoObject = VideoReader('FringeVideo.avi');
numberOfFrames = get(videoObject, 'NumberOfFrames');
fringeVideo = read(videoObject, [1 numberOfFrames]);
```

`fringeVideo` is a 4D matrix containing the frame height, width, colour channel, frame number. The number of colour channels is 1 for gray scale images. Typical maximal dimensions are `fringeVideo(492,656,1,173)` for the SVS Vistek eco424MVGE camera as specified in Table 4.1. The position of the fringe pattern as shown in Figure 5.7 on a single frame `fringeFrame = fringeVideo(1:491, 1:655, 1, frameNumber)` is entered manually using the centre coordinates `xCentre`, `yCentre`, and its radius `r`. The area of interest can be cut out by applying a circular mask, moving the pattern to the middle of the image and setting all values around the fringe pattern to zero. The mask can be reused for all frames.

```
[x, y] = meshgrid(1:655, 1:491);
mask = sqrt((x-xCentre).^2+(y-yCentre).^2) <= r;
fringeFrame(~mask) = 0;
fringeFrame = fringeFrame((yCentre-r):(yCentre+r),
    (xCentre-r):(xCentre+r));
```

Next the fringes are Fourier transformed. All spatial frequencies centred around the origin of the Fourier transform are cut out as shown in Figure 5.8 with a manually configured mask `maskFFT` that can be created similar to `mask`. It is important, that `maskFFT` cuts out the low spatial frequencies such that the absolute maximum of the remaining Fourier transform is in one of the fringe peaks and not at the outer rim of the cut out area.

```
fringeFFT = fftshift(fft2(fringeFrame));
fringeFFT(maskFFT) = 0;
```

The position of the maximum is determined and the half space opposite to the centre is set to zero with another mask. The `maskFFT` and `maskHalfspace` can be reused for all frames and does not need to be redetermined by finding the maxima at `xMax`, `yMax` for all frames.

```
maxValue = max(max(fringeFFT(:)));
[xMax, yMax] = find((fringeFFT) == maxValue);
m = (xMax-r) / (yMax-r);
t = xMax - m*yMax;
maskHalfspace = y(1:2*r+1,1:2*r+1) -
    m*x(1:2*r+1,1:2*r+1) - t <= 0;
fringeFFT(maskHalfspace) = 0;
```

Last the maximum of the remaining fringe peak is shifted to the origin. An inverse Fourier transform gives the `phase` shift introduced between the reference and the test wave of the Mach-Zehnder interferometer.

```
fringeFFT = circshift(fringeFFT, [-xMax+1 -yMax+1]);
phase = ifft2(fringeFFT);
```

The mask is applied once more to the obtained `phase` to avoid problems with phase unwrapping at the outer boundaries. Then the phase is unwrapped. This can be done via 2D phase unwrapping as described in Section 5.4. The `unwrap` function of Matlab should be avoided, since it only unwraps 1D arrays, leading to confusing results if applied on a 2D array. There are algorithms and Matlab codes available online that work accurately as shown in Figure 5.9, e.g. `unwrapping_qg_trim.m` by Qian Kemaoy [220,223].

```
phase(~mask((yCentre-r):(yCentre+r),
    (xCentre-r):(xCentre+r))) = NaN;
[phaseUnwrapped,~] = unwrapping_qg_trim(phase,
    mask((yCentre-r):(yCentre+r),
    (xCentre-r):(xCentre+r)));
```

The phase shift between the reference and the test wave of the Mach-Zehnder interferometer contains the information about the phase delay introduced by all surfaces of the LL, not only those of the moving surface of the liquid. To extract the deformation of the liquid surface a reference interferogram has to be measured for a flat LL surface at rest. By repeating all steps for the reference, i.e. masking, Fourier transforming, and unwrapping, the phase shift introduced by all surfaces except the oscillating LL surface can be calculated and subtracted.

```
phaseSurface = phaseUnwrapped - phaseUnwrappedReference;
```

To create comparable phase information for multiple measurements it can be useful to subtract the mean of `phaseSurface` and to calculate the introduced optical path length `OPL` and the surface deflection `surface` with the `wavelength` of the laser and the refractive indices of the liquid `nLiquid` and the oil `nOil`.

```
phaseSurface = phaseSurface -  
    nanmean(nanmean(phaseSurface));  
OPL = phaseSurface*wavelength/2/pi;  
surface = OPL/(nOil-nLiquid);
```

This can be done for single images as well as for whole videos.

D. Implementation of the Hankel transform

This appendix shows how to calculate the time-dependent actuation voltage $U(t)$ to create a desired surface profile $u(t = 0, r)$ at time $t = 0$ in Matlab. The theoretical background is explained in Section 5.2.2.

D.1. Calculation of the actuation voltage signal

The actuation voltage is calculated from the desired surface profile using the Hankel transform. The necessary parameters for the computation are the radius of the lens for the liquid lens (LL) surface at rest R and the speed of the waves c . The actuation voltage is applied via a NI D/A converter that can write 80 kSamples. The duration of the actuation voltage signal has to be chosen sufficiently larger than the expected pulse length $4R/c$:

```
% LL parameters
R = .00265;           %Radius in m
c = .26;             %speed of waves in m/s
%Acquisition parameters
dt = 1/80000;        %in s (80kSample DA card)
%Free coordinate parameters
tmax = .5;           %Voltage signal length in s
rmax = R;            %Radius of the surface input in m
%Roots of the Bessel function J_1
j11 = 3.831705970;
j12 = 7.015586670;
```

The coordinates time t , radius r , and radial spatial frequencies k space are then:

```
t = -tmax/2 : dt : tmax/2;
k = 0 : pi/(c*tmax) : pi/(c*dt);
r = 0 : c*dt : rmax;
```

The desired surface of the liquid lens u is put in as a function of the radius. The following is a list of the used surface functions u for the measurements shown in Chapter 5.

```
%Zernike spherical aberration
u = (6*(r/R).^4 - 6*(r/R).^2 + 1);
%Axicon
```

```
u = 2/3 - abs(r/R);  
%LL ground mode  
u = besselj(0, j11*r/R);  
%LL 2nd Bessel mode  
u = besselj(0, j12*r/R);  
%Top hat  
u = r*0 - 0.25; u(r<R) = 0.75;
```

All surface functions are set to zero outside of the lens.

```
u(r>R) = 0;
```

The Hankel transform can be computed in different ways: Direct integration using a matrix product, by integrating the Bessel kernel a priori, the quasi-discrete Hankel transform [217], and the quasi fast Hankel transform [216]. There is a Matlab toolbox available by Marcel Leutenegger [218] including functions for all techniques. The easiest way to compute the Hankel transform is by direct integration.

```
function H = hankel0(u,r,k)  
[r,w] = sort(r(:).');  
u = u(w);  
r = [(r(2:end) + r(1:end-1))/2 r(end)];  
I = 2*pi./k(:)*r.*besselj(1,k(:)*r);  
I(k==0,:) = pi*r.*r;  
I = I - [zeros(numel(k),1) I(:,1:end-1)];  
H = reshape(I*u(:),size(k));
```

with the integration kernel I and the spatial spectrum H.

The voltage spectrum `Volt` according to Equation 5.23 can be computed after applying the Hankel transform:

```
H = hankel0(u,r,k);  
Volt = k.^2.*besselj(1,k*R).*H;
```

The time dependent voltage actuation signal is obtained with an inverse Fourier transform. Since we defined our radial spatial frequency `k` over the interval $[0, \pi/(c \cdot dt)]$ we need to mirror the voltage spectrum to be able to apply the inverse Fourier transform.

```
Spectrum = [Volt flip(Volt(2:end))];  
U = 2*pi/c*fftshift(real(ifft(Spectrum)))
```

D.2. Export to LabVIEW

The voltage actuation signal is exported to LabVIEW using a `.wav` audio file with the voltage actuation signal in its first channel and the camera trigger in the second

channel. The DA converter can write 80kSamples. The choice of `tmax` produces voltage signals `U` with a length of 80001 samples and a duration of 1 s. The voltage pulse has a length of $4R/c = 41$ ms, which is a length of 3262 samples.

The actuation voltage typically contains singularities, therefore it is useful to truncate and to rescale the remaining signal.

```
cutoff = 55000;
%cutoff is chosen depending on the size of U between
  the singularities
for i = 1:80001
    if U(i) > cutoff
        U(i) = cutoff;
    elseif U(i) < -cutoff
        U(i) = -cutoff;
    end
end
U = U./max(U);
```

To measure the liquid lens surface at video rate, it is desirable to increase the pulse frequency by truncating the length of the voltage signal. For a frame rate of 10 Hz the actuation voltage is cut to 8000 Samples.

```
U = U(36001:44000);
```

The camera acquisition can be triggered externally when the desired surface is present. The exact length of the trigger pulse is irrelevant.

```
TriggerSignal = zeros(1,8000);
TriggerSignal(4000:4005) = 1;
```

The signals can then be repeated multiple times to create the desired LL surface with a frequency of 10 Hz.

```
for i = 1:12 %2^(i)/10 s
    U = [U U];
    TriggerSignal = [TriggerSignal TriggerSignal];
end
```

Last the actuation and trigger signal are written into the two stereo channels of a .wav file. The audio file can be opened in LabVIEW as described in Appendix B.

```
Stereo(:,1) = U(:);
Stereo(:,2) = TriggerSignal(:);
audiowrite('LabVIEW.wav',Stereo,80000)
```


Curriculum vitæ

Matthias Strauch was born on 3rd of August 1989 in München. He received his Abitur at the Gymnasium Neubiberg in 2007. He obtained his Master's degree in physics at the Ludwig-Maximilians-Universität München in 2012. He started his PhD research in 2013 in the Optica group of the department of Imaging Physics at the faculty of Technische Natuurwetenschappen at the Technische Universiteit Delft.

List of Publications

Peer-reviewed scientific journal publications

- Matthias Strauch, Irina L. Livshits, Florian Bociort, and H. Paul Urbach, *Wide-angle spectral imaging using a Fabry-Pérot interferometer*, Journal of the European Optical Society: Rapid Publications, **10** 15037 (2015)
<https://doi.org/10.2971/jeos.2015.15037>
- Matthias Strauch, Yifeng Shao, Florian Bociort, and H. Paul Urbach, *Study of surface modes on a vibrating electrowetting liquid lens*, Applied Physics Letters, **111** 17 171106 (2017)
<https://doi.org/10.1063/1.4999562>
- Matthias Strauch, Peter A. A. M. Somers, Florian Bociort, and H. Paul Urbach, *Creation of aspheric interfaces on an electrowetting liquid lens using surface oscillations*, AIP Advances, **8** 11 115224 (2018)
<https://doi.org/10.1063/1.5063994>

International conferences

- Matthias Strauch, Irina L. Livshits, Yifeng Shao, Florian Bociort, and H. Paul Urbach, *Optical optimisation of Fabry-Pérot based spectral imaging systems*, EOSAM (2014)
- Matthias Strauch and H. Paul Urbach, *Study of surface harmonics on an electrowetting-based liquid lens*, EOSOME (2015)
- Matthias Strauch and H. Paul Urbach, *Surface harmonics on liquid lenses*, EOSAM (2016)
- Matthias Strauch and H. Paul Urbach, *Surface Harmonics on Liquid Lenses*, 2016 IEEE Photonics Conference (IPC), 248 (2016)
<https://doi.org/10.1109/ipcon.2016.7831063>

- Matthias Strauch, Sander P. Konijnenberg, Yifeng Shao, and H. Paul Urbach,
Wavefront shaping with an electrowetting liquid lens using surface harmonics,
Proc. SPIE Adaptive Optics and Wavefront Control for Biological Systems III, **10073** 1007304 (2017)
<https://doi.org/10.1117/12.2252854>
- Matthias Strauch and H. Paul Urbach,
Non-standard phase manipulation with a liquid lens,
Face2Phase (2017)
- Matthias Strauch, Peter A. A. M. Somers, and H. Paul Urbach,
Creation of aspherical surfaces on a liquid lens,
Electrowetting (2018)
- Matthias Strauch, Peter A. A. M. Somers, and H. Paul Urbach,
Tutorial on how to use an off-the-shelf liquid lens as a tunable asphere using surface oscillations,
EOSAM (2018)

National conferences

- Matthias Strauch, Florian Bociort, and H. Paul Urbach,
The Spectr@phone - Study of a Fabry-Pérot for spectral imaging,
Symposium Fotonica (2013)
- Matthias Strauch, Irina L. Livshits, Florian Bociort, and H. Paul Urbach,
Dependency of optical design and Fabry-Pérot interferometers in spectral cameras,
Symposium Fotonica (2014)
- Matthias Strauch, Wim Weltjens, Florian Bociort, and H. Paul Urbach,
Prototype of a handheld spectral camera using a Fabry-Pérot spectrometer,
Symposium Fotonica (2015)
- Matthias Strauch and Yifeng Shao,
Surface mechanics of a liquid lens,
Dutch Optics Centre Opening (2016)
- Matthias Strauch and H. Paul Urbach,
A new technique to create tunable liquid aspheres,
Photonics event (2017)
- Matthias Strauch,
Creating freeforms with liquid lenses ?!?,
Freeform Optics Symposium (2017)

Interviews

- Floor van Dam,
Detecting child abuse,
De Physicus, **26** 4 32 (2016)

Unrelated publications

- Matthias Strauch, Andreas Graw, and Roland Kersting,
Terahertz study on nanoscale hole transport in pentacene,
INASCON (2008)
- Jan Philip Kolb, Matthias Strauch, Daniel Weng, Hubertus Hakert, Wolfgang Draxinger, Ralf Brinkmann, Reginald Birngruber, Sebastian Karpf, and Robert Huber
Fiber-Based Sub-Nanosecond Two-Photon Microscopy for Virtual H&E Histology,
ECBO (2019)
- Daniel Weng, Hubertus Hakert, Torben Blömker, Jan Philip Kolb, Matthias Strauch, Matthias Eibl, Philipp Lamminger, Sebastian Karpf, and Robert Huber
Sub-Nanosecond Pulsed Fiber Laser for 532nm Two-Photon Excitation Fluorescence (TPEF) Microscopy of UV transitions,
CLEO (2019)
- Matthias Strauch, Valerie Lutz, Jan Philip Kolb, Robert Huber, and Sebastian Karpf
1.6MHz FDML-MOPA Laser with 320MHz pulse repetition rate,
CLEO (2019)
- Matthias Strauch, Jan Philip Kolb, Daniel Weng, Melanie Wacker, Sebastian Karpf, and Robert Huber
Sectioning-Free Virtual H&E Imaging of Tissue Samples with Two-Photon Microscopy,
31st ECP (2019)
- Jan Philip Kolb, Matthias Strauch, Daniel Weng, Melanie Wacker, Wolfgang Draxinger, Nadine Merg, Jennifer Hundt, Sebastian Karpf, and Robert Huber
Two-photon microscopy for sectioning-free virtual H&E imaging,
104th DGP Annual Meeting (2020)
- Matthias Strauch, Jan Philip Kolb, Wolfgang Draxinger, Nadine Merg, Jennifer Hundt, Sebastian Karpf, and Robert Huber
Evaluation of two-photon fluorescence microscopy for sectioning-free virtual H&E imaging of different tissues,
32nd ECP, 33th IAP (2020)